Bulk and Surface Chemistry Modification of Highly Porous Carbon for Supercapacitors

Stephanie L. Candelaria

A dissertation
submitted in partial fulfillment of the
requirements for the degree of

Doctor of Philosophy

University of Washington
2013

Reading Committee:
Professor Guozhong Cao, Chair
Professor Christine K. Luscombe
Professor Brian D. Flinn

Program Authorized to Offer Degree:
Materials Science and Engineering

University of Washington

Abstract

Bulk and Surface Chemistry Modification of Highly Porous Carbon for Supercapacitors

Stephanie L. Candelaria

Chair of the Supervisory Committee:
Professor Guozhong Cao
Materials Science and Engineering

Highly porous carbon prepared through sol-gel processing is an excellent electrode material for supercapacitors, also known as electrochemical capacitors, because of its high surface area and pore volume, good conductivity, and low cost. Research has mostly focused on increasing the surface area of the carbon to improve charge storage, but there are limits to how large this value can be while still maintaining good electrochemical performance of the material. Alternatively, carbon can be modified with foreign elements, either in the bulk or on the pore surfaces, to induce pseudocapacitive reactions that can increase capacitance. Modified samples can also be tested at higher working voltages, which significantly increase the energy and power densities. In this work, highly porous carbon is modified with nitrogen and tested as electrodes in supercapacitors. Modification significantly increases the wettability of the carbon, and the capacitance increases with increasing nitrogen added. However, too much nitrogen can cause pore blockage and decrease accessible surface area, limiting the capacitance. Highly porous carbon, both with and without nitrogen on the pore surfaces, is then tested at higher working voltages. Increasing the voltage from 2V to 3V significantly improves both the energy density and power density. Finally, porous carbon was also synthesized from lignin, a complex polymer derived from natural resources and a waste product in the paper industry. Purification removed over half of the impurities and resulted in porous carbon with four times the internal surface area compared to unpurified lignin. When tested in devices, lignin-derived carbon shows promise as low-cost, renewable material for high performance supercapacitors.

Table of Contents

List of Figures

Figure number

List of Tables

Table number

1. Introduction

As the world shifts its focus away from fossil fuels, there has been an increased interest in making renewable energy generation efficient and accessible. But in order to make new technologies viable, energy storage devices such as batteries and supercapacitors are extremely important. Wind, solar, and other renewable energy resources are largely intermittent, requiring energy to be collected and stored during peak generation times then recovered in order to meet demand during off-peak hours.[2]

Common energy storage devices are shown in the Ragone plot in Figure 1.1. While conventional capacitors have high specific power, delivering energy quickly, they suffer from low specific energy. Fuel cells and batteries, on the other hand, have high specific energy, meaning that they can store a significant amount of energy. However, their low power means they cannot be charged or discharged quickly. An ideal device would combine high specific power with high specific energy.

There are several advantages supercapacitors, also known as electrochemical capacitors or ultracapacitors, have over other energy storage devices. Although their energy density (~5 Wh/kg) is lower than that of batteries, they have high power density (~10 kW/kg, about 10 times larger than in secondary batteries),[3, 4] can charge and discharge quickly, and have cyclic stability that can exceed millions of cycles.[5, 6] They are also environmentally friendly, safe, and can operate in a wide range of temperatures. Supercapacitors are utilized commercially for a variety of applications, including back-up power supplies, industrial equipment, and hybrid/electric vehicles, where supercapacitors can provide high power during acceleration and recover energy during braking. They can be used alone or in combination with batteries or fuel cells.[7-9]

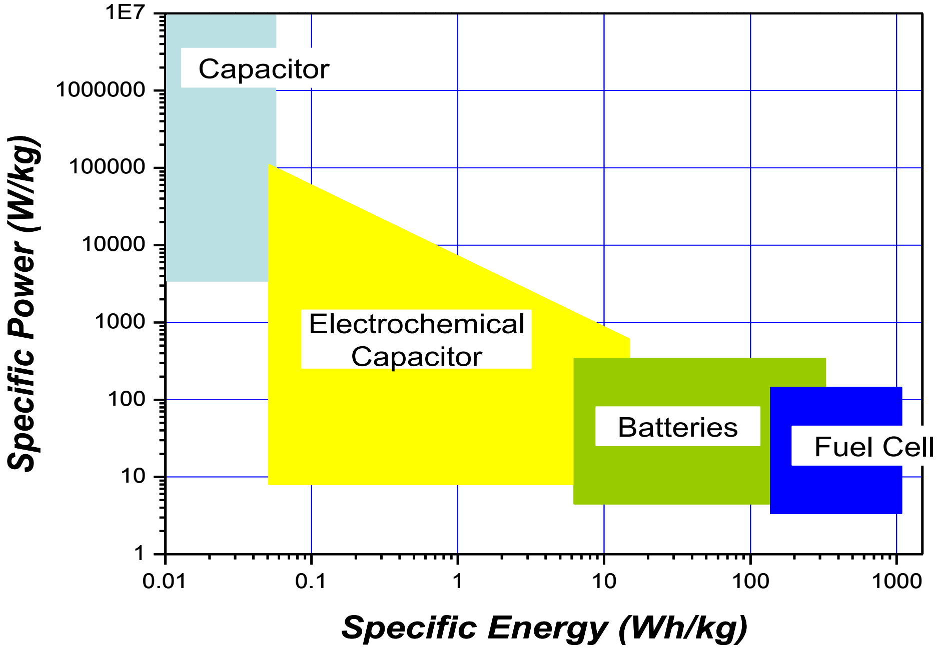

Figure 1.1. Ragone plot showing power density vs. energy density for various energy storage devices. An ideal device will have high specific power and high specific energy.

Supercapacitor devices are composed of two electrodes made from active material, two current collectors, and a separator. The current collectors are electronically conductive and serve as leads to transfer electrons to and from the electrodes. The separator is porous to allow ions in the electrolyte to conduct between the electrodes and also electronically insulating to avoid self-discharge. The active material is both electrically and ionically conductive. The electrodes and separator are surrounded by an ionically conducting medium, most commonly a liquid electrolyte, but solid electrolytes are also used. The device is usually sealed in a container, making it a thermodynamically isolated system as it exchanges only energy with the external environment, as opposed to mass in the form of reactants or products. There are also no moving parts in these devices, making them mechanically stable.[10]

Capacitance C is related to surface area A, effective dielectric constant ε, and charge separation distance d, according to Equation 1,

$$C = \frac{\varepsilon A}{d} \qquad (1)$$

Conventional dielectric capacitors consist of two parallel conducting plates, separated by a dielectric material. Electrostatic polarization occurs in the dielectric when an external voltage is applied, and the plates become oppositely charged. When the external voltage is removed, the charge separation persists and energy is stored until the capacitor is allowed to discharge. However, in traditional dielectric capacitors, the capacitance is limited by the thickness of the dielectric material. The thinnest dielectric layers are 2-5 μm thick.[11]

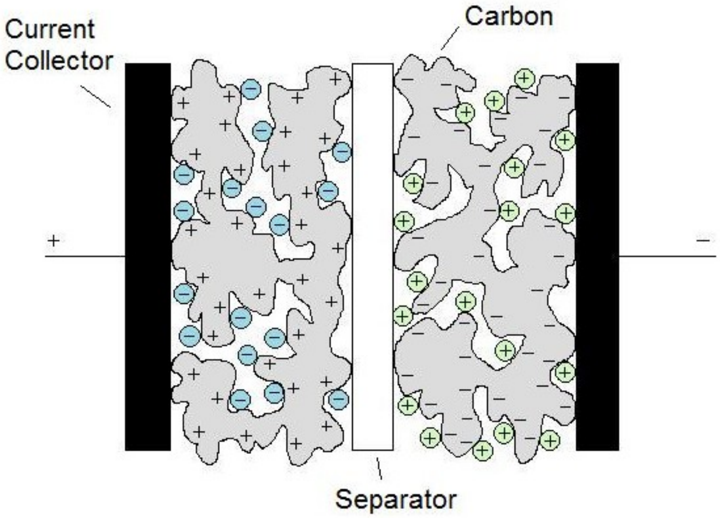

Figure 1.2. Illustration of the electric double-layer mechanism in a supercapacitor.

However, in the case of supercapacitors, charge separation distances are on the order of 1 nm. Additionally, the flat plate electrodes in conventional capacitors are replaced by highly porous electrodes. These materials contain a mixture of micropores (<2 nm), mesopores (2-50 nm), and macropores (>50 nm), the presence of which create a significantly higher specific surface area than nonporous materials. The combination of high surface area and small charge separation result in storage capacities that are several orders of magnitude higher than that of conventional dielectric capacitors. Charge storage takes place through the formation of an electric double-layer structure at the interface between the solid electrode and the electrolyte, as illustrated in Figure 1.2. The electrode material is charged by an applied voltage and oppositely charged ions in the electrolyte adsorb onto the electrode surface. Supercapacitors that make use of this charge storage mechanism are also referred to as electric double layer capacitors (EDLCs). Because a double layer forms on each of the two electrodes, a supercapacitor can be thought of as equivalent to two capacitors in series, each with its own capacitance, C_1 and C_2. As such, the total capacitance C of the system is given by Equation 2,

$$\frac{1}{C}=\frac{1}{C_1}+\frac{1}{C_2} \qquad (2)$$

The total capacitance is determined by the electrode with the smallest capacitance. As such, the amount or type of active material in each electrode is often adjusted to obtain matching capacitances.

Commercially available supercapacitors are usually based on porous carbon materials, such as activated carbon. Porous carbon electrodes are deposited on an aluminum foil current collector and a thin porous separator material is placed between them to prevent electrical contact but still allow electrolyte ion transport. The assembly is rolled into a cylinder, packaged, and impregnated with liquid electrolyte. Most commercially available supercapacitors use organic electrolyte, leading to maximum working voltages of 2.5-2.7V. For higher working voltages, several supercapacitor cells can be connected in series. The capacitance can reach as high as 5000 F, but when the packaging is taken into account, this translates to a specific capacitance of only 10 F/g. Likewise, the maximum energy density is less than 10 Wh/kg.[12] This presents a tremendous opportunity for the improvement of carbon-based supercapacitors.

Figure 1.3. Examples of commercially available supercapacitors manufactured by Maxwell Technologies.

1.1. Carbon

Carbon has the ability to form a number of different allotropes, of which diamond and graphite are probably the most well-known, but fullerenes and carbon nanotubes are gaining in popularity due to their unique properties. The electronic configuration of carbon is $1s^2 2s^2 2p^2$. The 2s and 2p orbitals can form three different hybridizations, sp,

sp^2, and sp^3 when chemical bonds are formed with other atoms. The sp orbital is has two σ electrons and two π electrons, sp^2 has three σ electrons and one π electron, and sp^3 has four σ electrons. It is because of these three hybrid orbitals that carbon can form numerous allotropes with a wide range of properties. Figure 1.4 shows some common carbon structures.

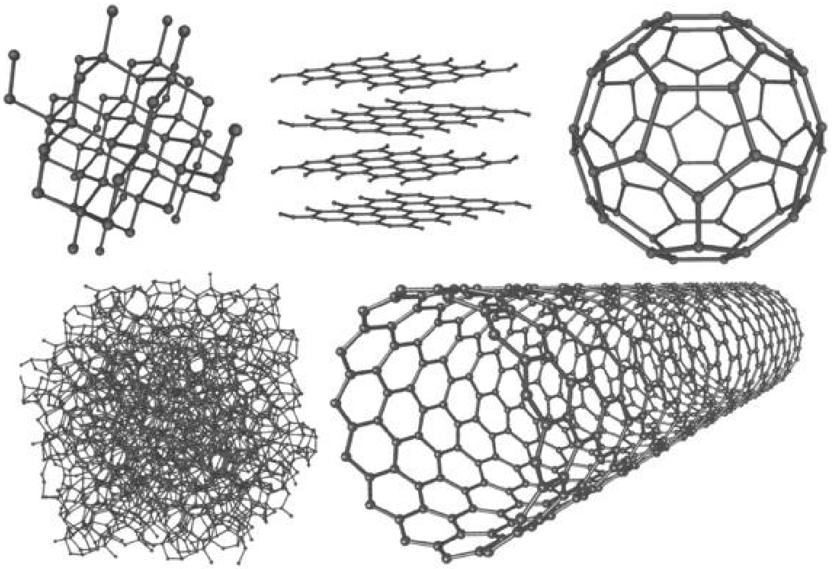

Figure 1.4. Common allotropes of carbon. (a) Diamond, (b) graphite, (c) C60, (d) amorphous carbon, and (e) carbon nanotube.

Diamonds are composed of a three dimensional network of carbon atoms with sp^3 hybridization. Each atom is tetrahedrally bonded to four other atoms and forms the same cubic crystal system as silicon and germanium. Because the C-C bonds are so strong, diamond is the hardest naturally occurring substance. It is also highly transparent and electrically insulating. Diamond-like carbon also has sp^3 hybrid bonds and is very hard, but it forms an amorphous structure due to random rotation between the tetrahedra. This material usually exists as a thin film, as it is difficult to maintain random repetition of tetrahedra over long distances.

Graphite is a two dimensional structure composed of planar hexagons of sp^2 hybridized carbon bonds. Each carbon atom is trigonally bonded to three other atoms. The planes tend to stack together due to weak van der Waals-like interactions between the π electron clouds of each of the layers. These weak interactions allow the sheets to slip past each other easily, making graphite soft enough to be used as a lubricant. The delocalized π electrons also give rise to high electrical conductivity, but only in the plane of the hexagonal carbon layers. A single sheet of graphite is referred to as graphene.

With the introduction of pentagons into the hexagonal structure of graphite, the flat sheets can be curved to form closed shells called fullerenes. These materials retain sp^2 hybridization. The smallest fullerene is C_{60}, which consists of 20 hexagons and 12 pentagons of carbon atoms. Larger structures, such as C_{70}, C_{240}, and C_{540}, are possible by the introduction of additional hexagons while keeping the closed-shell structure. Carbon nanotubes are also part of the fullerene family. The nanotube wall is formed by a graphene sheet that has been rolled into a cylinder and the nanotube ends are capped by hexagons and pentagons of carbon atoms.[10]

1.2. Highly porous carbon

Carbon materials are playing a significant role in the development of alternate clean and sustainable energy technologies.[13] For example, fullerene-containing n-type semiconducting materials are used extensively in organic photovoltaics.[14] Lithium intercalation/deintercalation in between graphite layers played a large role in the development of lithium-ion batteries.[10] Carbon nanotubes and graphene are also studied for the development of batteries.[15-17] Porous carbon is commonly used as an adsorbent material for hydrogen and natural gas storage.[18-21] Furthermore, highly porous carbon has been widely used as filters, sorbents, scaffolds, and matrices in many other technically important fields. Examples include water purification,[22-24] artificial livers and kidneys,[25-28] and catalyst support,[29-32] among others. Porous carbon has also become the most commonly used electrode material in supercapacitor devices[33] because it is electrically conductive, easy to process, chemically inert, stable, lightweight, abundant, and inexpensive.[5]

There are a number of ways to obtain highly porous carbon. Perhaps the easiest way is to pyrolyze and activate naturally occurring carbonaceous precursors such as coal, wood, coconut shells, fruit stones, and other agricultural byproducts. While carbon derived from natural products are inexpensive and readily available, the nanostructure is limited by the nature of the carbon precursor and is hard to control. These materials can have very large pore size distributions and often the pores are randomly connected, which results in poor conductivity and ionic transport.[2] Additionally, naturally-derived carbons can contain a high amount of impurities that can cause short circuiting and unwanted redox reactions when used in devices. Synthetic carbon, on the other hand, can be tailored to obtain the desired pore structure and there is greater control over the level and type of impurities. Methods to synthesize highly porous carbon include etching metal carbides (carbide-derived carbon), templating carbon, and sol-gel processing. Recent research has also investigated the use of advanced carbons, such as carbon nanotubes (CNTs) and graphene. In order for these carbons to be useful for supercapacitors, both high surface area and tailored pore structure are extremely important, as these make more active material available to the electrolyte.[34, 35]

Carbide-derived carbons (CDC) are synthesized through the selective removal of non-carbon atoms from carbides. The most commonly used removal methods are high temperature chlorination and vacuum decomposition, but using halogens and etching in supercritical water are other possibilities. The porous structure, including average pore size, pore size distribution, pore volume, and specific surface area of CDC can be tailored through selection of the precursor (different spatial distributions of carbon atoms in the carbide structure) and the heat treatment conditions (nanotextural reorganization). The resulting porous carbons can have surface areas greater than 2000 m^2/g and pores that are approximately 0.3-10 nm in diameter.[10, 36]

For example, Presser *et al.*[37] developed CDC nanofibrous felts using electrospun titanium carbide nanofelts as the precursor. Conformal transformation of TiC into CDC conserves the main features of the precursor, including the high interconnectivity and structural integrity. The TiC-CDC nanofelts are mechanically flexible and resilient, and can be used as an electrode material for supercapacitors without the addition of a binder. After synthesis through chlorination of the precursor at 600°C, the TiC-CDC nanofelts show an average pore size of ~1 nm and a high specific surface area of 1390 m^2/g, and the nanofibers have graphitic carbon ribbons embedded in a highly disordered carbon matrix. Korenblit *et al.*[8] prepared CDC from SiC. An ordered mesoporous SiO_2 template was infiltrated with the precursor polycarbosilane and the template was then etched away, leaving mesoporous SiC. The technique produced porous CDC nanorods with aligned mesopores between the particles. Pore sizes were less than 4 nm and the BET specific surface area was 2250-2430 m^2/g, which is higher than previous studies of SiC-CDC. The ordered mesopores allow for fast ion conductivity into the bulk CDC particles, leading to capacitance retention at high current densities.

Templated carbon is synthesized through carbonization of an organic precursor impregnated in an inorganic template followed by removal of the template.[38] Common template materials include clay, where the carbon precursor is infiltrated between the lamellae,[10, 39] and mesoporous molecular sieves, which are often made from mesoporous silica.[40-42] Yet another material is zeolites, which possess long-range order, three-dimensional channels, and an open microporous structure. Since the micropores of the resulting carbons are uniform and ordered, all of the pores are expected to be accessible to the electrolyte. Because of the precise control of the pore size, creating carbons with microporosity and very little mesoporosity, surface areas can reach over 4000 m^2/g.[10, 43] However, there are several drawbacks to this method. This technique uses an expensive template material, which also requires a harsh chemical treatment to remove, such as washing in HF. Both of these issues make scaling up and commercial development very difficult.

Carbon nanotubes and graphenes have also been used in the manufacturing of supercapacitors.[12, 44] CNTs are highly conductive and have an accessible pore network of mesopores, allowing for fast ion transport for EDLCs. However, the lack of micropores leads to a moderate surface area of only 120-500 m^2/g.[9] A higher capacitance can be achieved by introducing defects. For example, more defected outer CNT walls and the presence of a thin layer of amorphous carbon on the walls results in better charge accumulation.[45] Additionally, increasing the surface area through activation processes can also improve the capacitance. An *et al*.[46] obtained high capacitance by heating CNTs to enhance their specific surface and pore distribution. However, the specific surface area of CNTs still remains low compared to other activated carbon electrodes (specific surface area up to 3000 m^2/g) or mesoporous carbons (up to 1730 m^2/g).[47, 48]

The theoretical surface area of graphene is 2675 m^2/g. However, this has yet to be achieved due to agglomeration of the graphene sheets, decreasing the accessible surface area and leading to moderate capacitances.[49-51] Wang *et al*.[52] used a gas-solid reduction process to avoid aggregation and achieved a high specific capacitance in aqueous electrolyte with an high energy density. Liu *et al*.[53] fabricated supercapacitors with curved graphene to prevent the sheets from restacking, obtaining a very high energy density using an ionic liquid electrolyte. Several groups report the effectiveness of using CNTs as a spacer in between the graphene sheets, preventing agglomeration and also acting as a conductive additive and binder. The ideal weight ratio of graphene sheets to CNTs was found to be 9 to 1, leading to the high specific capacitance.[54, 55]

Carbon aerogels and cryogels prepared by sol-gel processing have been highly researched for a number of years because they have the advantage of possessing a tunable three-dimensional hierarchical morphology. Additionally, they can be easily fabricated in large quantities in the form of monoliths on the macroscopic scale. Aerogels and cryogels have low mass densities, continuous porosities, and high surface areas. The microstructure consists of nanometer-sized particles interconnected in a three-dimensional network. These materials are typically synthesized through sol-gel processing, where organic precursors are polymerized to form highly cross-linked organic gels. Specialized drying techniques (e.g., supercritical drying or freeze drying) are used to remove the solvent while retaining the porous solid network. The dried gel is then pyrolyzed at elevated temperature in an inert atmosphere to obtain highly porous carbon.

Pekala was the first to synthesize organic and carbon aerogels through the polycondensation reaction of resorcinol and formaldehyde.[56] Since then, other precursor materials have been used to synthesize gels through sol-gel processing as well, such as phenol-furfural, melamine-formaldehyde, and others.[57-60] The morphology and properties of the final carbon can be controlled by adjusting the sol-gel chemistry.[61] Specifically, several researchers have demonstrated that the surface area and pore size can be manipulated by changing the precursor to catalyst ratio and the solid content of the sol.[20, 62, 63] Early research achieved surface areas of 400-800 m^2/g with pore sizes less than 100 nm.[58] Tamon *et al.* were the first to report on carbon cryogels, which used freeze drying to remove solvent rather than the supercritical drying process that is used for carbon aerogels. They found that micropores (<2nm) form more easily in cryogels than aerogels when pyrolyzed, leading to surface areas above 1200 m^2/g.[64]

Carbon cryogels are glassy carbons, composed of graphene ribbons with short-range crystalline order, but lacking long-range order. This interrupted structure results in a large amount of dangling bonds. All the carbon bonds are graphite-like with sp^2 hybridization.[65] Each sp^2 orbital is composed of three σ electrons and one π electron, giving rise to planar hexagons of carbon atoms.[10] The presence of delocalized π electrons results in the porous carbon's high conductivity,[65] making them excellent candidates for energy storage devices. Sol-gel derived highly porous carbon with surface areas of 1000 m^2/g or higher typically have capacitances ranging from 50 to 200 F/g for aqueous electrolytes and 30 to 100 F/g for organic electrolytes.[9]

1.3. Factors affecting supercapacitor performance

According to Equation 1, the capacitance of a supercapacitor is directly dependent on the electrode surface area. As such, significant research efforts have been made to achieve a higher capacitance by maximizing the surface area of carbon through careful thermal, chemical, or electrochemical treatment. However, some problems arise as the specific surface area increases. For example, an increase in surface area may result in an increase in electrical resistivity due to surface scattering effects. Additionally, the linear relationship between capacitance and surface area exists only up to a certain point. Above 1500 m^2/g, the capacitance begins to level off, no longer increasing linearly with surface area. One explanation for this is that the increased pore volume at very high surface areas results in pore walls that are too thin. As the thickness of the pore walls decreases, it approaches the screening length of the electric field created by the electric double layer. If the walls are too thin, the electric field and charge density will not decay to zero within the pore walls. Therefore, a thinner pore wall cannot accommodate the same amount of charge as a thicker pore wall can at a given potential. Further increases in surface area will be accompanied by a decrease in capacitance.[66] Another reason for the leveling off of capacitance is that the number of small micropores (~1 nm) increases for high surface area samples. Micropores of this size could be too small to allow electrolyte ions to diffuse inside, resulting in inaccessible surface area that is not available for charge storage. Therefore, surface area measurements can overestimate the actual surface area available for ion adsorption.[61, 66] However, some recent research concluded that once the pores become smaller than the solvated ion radius, the specific capacitance increases again. This is due to a distortion and reduction in size of the solvated shell surrounding the ion, allowing the ion to get closer to the electrode surface and decreasing the charge separation distance *d* in Equation 1. The above discussion demonstrates that not only surface area, but pore structure is important for achieving high capacitance.

The porous structure also has a significant effect on the electrolyte ion transport kinetics, which impacts the supercapacitor performance as well. First, the pore volume must be large enough to store electrolyte. Additionally, the pore channels need to be tailored to allow the electrolyte ions effective access to the all of the active surfaces of the electrode, as well as rapid transport to and from the active sites.[9] Important factors to consider include the pore size, tortuosity, length and shape of the pores, as all of these will affect the resistance of the electrode.[61] The pore size distribution is important as well. Micropores can store more energy because they provide high surface area, which results in a higher energy density. Mesopores and macropores, on the other hand, result in faster ion transport as there is less resistance due to pore wall interactions. This creates devices with higher power density.[9, 61] Therefore, for high energy and power density, a hierarchical pore structure is necessary, creating a balance between small and large pore sizes.

Engineering surface chemistry is also an effective way to improve the storage capacitance. Voltage dependent reversible *Faradaic* reactions between the electrode and the electrolyte are introduced, either in the form of surface adsorption/desorption of ions, redox reactions with the electrolyte, or doping/undoping of the electrode materials. These reactions are often referred to as pseudocapacitive reactions. In this way, electric energy is stored in the form of chemical potential. The alteration of surface chemistry may also permit a higher working voltage for a supercapacitor. An appropriate modification of surface chemistry permits a significant increase in the energy storage density. In addition, an appropriately modified surface may suppress the influence of impurities that limit the cyclic life of supercapacitors when they react with the electrolyte.

Recent research has shown the benefit of pseudocapacitive reactions in supercapacitors made from porous carbon. This is achieved by the introduction of foreign elements in the carbon network as heteroatoms, or by the addition of surface functionalities. Oxygen is perhaps the most studied element added to carbon, but there has been a growing interest in other elements, such as nitrogen. However, adding foreign elements must be done with care, as some are detrimental to supercapacitor performance.[67] For example, heavy metals in amounts of 100 ppm or more may cause short circuiting.[68] Additionally, foreign elements in the bulk network can reduce the electrical conductivity by disrupting sp^2 hybridization in the graphene sheets.[69] In order to avoid this issue, the addition of surface functionalities may be a better option. This must be done with care as well since some surface groups (including those containing oxygen) create decomposition products in certain electrolytes that can block pores, which increases resistance and causes capacitance fading.[70] However, with careful tailoring of electrode surface chemistry and electrolyte selection, the capacitance can be significantly increased. Several studies have already demonstrated the benefits of foreign elements in aqueous electrolytes.[71-75] However, few studies have tested these materials in organic electrolytes.[72]

Aqueous electrolytes, such as KOH or H_2SO_4, are very popular in the literature due to the high capacitance they can achieve. This is because of the small diameter of the ions, allowing more ions to adsorb on the electrode’s surface than would be possible with larger diameter ions. Additionally, they have high conductivity of approximately 1 S/cm.[10] However, aqueous electrolytes are limited in that the voltage window for device operation is rather small. The maximum voltage is less than 1V as voltages above this value approach the thermodynamic voltage window of water (1.23V), at which point the electrolyte decomposes.[76] Because the potential at each electrode is not easily controlled due to capacitance mismatch, the voltage window is typically restricted to 0.7-0.8V for supercapacitors in aqueous medium.[10] Devices that use organic electrolytes often have lower capacitances than those that use aqueous electrolytes due to the decreased conductivity (~0.02 S/cm)[10] and the larger size of the ions. For example, tetraethylammonia tetrafluoroborate (TEATFB) in propylene carbonate has ionic diameters of approximately 0.68 nm for $(C_2H_5)_4N^+$ and 0.46 nm for BF_4^-.[5] The diameters are larger when considering the solvated shells that form around the ions in solvents. For instance, the ionic diameters increase to 1.35 nm for $(C_2H_5)_4N^+$ and 1.4 nm for BF_4^- in propylene carbonate (PC).[77] In comparison, solvated ionic diameters for ions in aqueous electrolytes typically range between 0.362 nm and 0.421 nm for both cations and anions.[5] However, the voltage window for organic electrolytes is much larger. The typical stability window is 2.7V,[10] with decomposition voltages varying between 3V and 5V.[76] For example, supercapacitor devices prepared from single wall carbon nanotubes were shown to operate at 4V using TEATFB in propylene carbonate as the electrolyte.[67] However, special care must be taken to limit the presence of impurities, as these can lead to electrolyte decomposition at lower voltage windows than expected. Even small traces of water have been shown to have a dramatic effect on the stability window of acetonitrile. At high purity, the voltage window is 5.9V, but this decreases to 3.8V and

2.7V when 14 ppm and 40 ppm of water is added, respectively.[10, 78] Nonetheless, the increased voltage window makes organic electrolytes very attractive for multiple applications, especially those that require higher energy and power density.

1.4. Research rationale

Ongoing research in the field of highly porous carbon for supercapacitors mostly focuses on increasing the surface area to increase charge storage according to Equation 1. However, there are limits to how large this value can be while still maintaining good electrochemical performance of the material. Alternatively, the carbon can be modified with foreign elements, both in the bulk or on the pore surfaces, to induce pseudocapacitive reactions. This pseudocapacitance adds to the capacitance that is already present due to double layer formation. In this work, highly porous carbon prepared through sol-gel processing is modified with nitrogen both in the bulk carbon network and on the pore surfaces. The process for modification is adjusted and refined to achieve the optimum nitrogen content, taking into consideration the changes that might occur to the underlying porous structure. The nitrogen-modified carbon is investigated for pseudocapacitive behavior, with the goal of increasing the total capacitance above that of unmodified carbon.

Next, the nitrogen-modified carbon is tested at higher working voltages in an attempt to significantly increase the energy density and power density of supercapacitors. Improving these two properties is essential for practical application of these devices. While energy density scales linearly with increasing capacitance, it is also directly dependant on the square of the working voltage. Therefore, increasing the voltage has a much greater impact on energy density than increasing capacitance. Power density is also directly dependant on the square of the working voltage. For supercapacitors composed of electrodes in an organic electrolyte, the typical working voltage is 2V. However, when impurities such as water and oxygen are minimized, the voltage can be pushed higher. Porous carbon electrodes, both with and without nitrogen coating the pore surfaces, are tested up to a working voltage of 3V. The objective is to determine under what conditions (nitrogen content and working voltage) the energy density and power density are maximized. Cyclic stability is also measured to see what effect the increased voltage has on the durability of the devices.

Finally, lignin (a complex polymer derived from renewable resources) is utilized as a novel precursor for porous carbon. This abundant material might be able to replace other precursors that are expensive and sometimes toxic. Additionally, because the process mirrors that used for synthetic phenolic resins, it may provide more precise control of pore structure and chemical composition than carbon derived from the direct pyrolysis and activation of biomass. Both the nitrogen-modified carbon and the lignin-derived carbon are characterized using techniques such as thermogravimetric analysis, nitrogen sorption analysis, x-ray photoelectron spectroscopy, cyclic voltammetry, galvanic cycling, and electrochemical impedance spectroscopy.

2. Electrochemical behavior

2.1. Double-layer formation

Classic carbon-based supercapacitors store charge through the formation of a double layer. When an electrode is connected to a power source, the surface of the electrode charges and attracts oppositely charged ions from the electrolyte. The electrolyte ions approach the electrode material, but they are not absorbed into it.[79] This forms an electric double layer, where the charges are physically separated by the interface between the electrode and the electrolyte. Figure 2.1 shows schematic illustrations of the electric double layer structure. When a voltage potential is applied, there is an increased concentration of charges that form a plane near the surface of the electrode. The inner Helmholtz plane (IHP) is associated with ions in the electrolyte that are specifically adsorbed onto the electrode surface. Ions that are within the electrolyte near the electrode surface but are not specifically adsorbed contribute to a diffusive region of charge. The outer Helmholtz plane (OHP) represents the closest distance that free solvated ions in the electrolyte can approach. There is no plane of charge associated with the OHP as it only represents the inner limit of the diffuse region of charge.[80] The diffuse layer is represented by a characteristic Debye length, and is usually on the order of 1 nm.[81] The charges in both the Helmholtz planes and the diffuse layer contribute to the capacitance.[82]

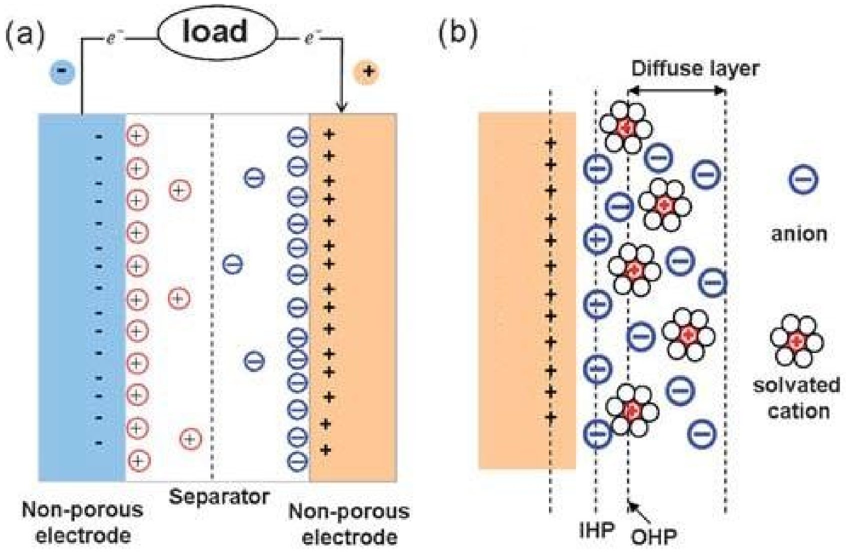

Figure 2.1. Schematic illustration of the double layer structure for simplified electrodes that do not take porosity into account. Each electrode of the two-electrode supercapacitor device stores charge through double layer formation (a), which is composed of a plane of charge within the electrode, and an inner Helmholtz plane (IHP), an outer Helmholtz plane (OHP), and a diffuse layer within the electrolyte (b).[82]

2.2. Equivalent circuits and impedance

An equivalent circuit that can be used to describe an EDLC consists of a resistor R_s and capacitor C in series, as seen in Figure 2.2a. R_s, or the equivalent series resistance (ESR), is a measure of the non-ideal behavior of a device. It is the sum of several ohmic resistances that exist in the device, such as the electrolyte resistance, the contact resistance between the carbon particles and at the interface between the current collector and carbon electrode, and the intrinsic resistance of the current collectors and the carbon. Since the resistivity of the metal current collectors is low, the ESR is mainly due to the electrolyte resistance both in the bulk and in the pores of the electrode, and contact resistance between the current collector and active material.[10] The capacitance C represents the double layer capacitance. A Nyquist plot, which graphs the real and imaginary impedance of a device over a range of frequencies, is shown in Figure 2.2b for this simple *RC* circuit. The x-intercept represents the ESR and the vertical line corresponds to an ideal capacitor.

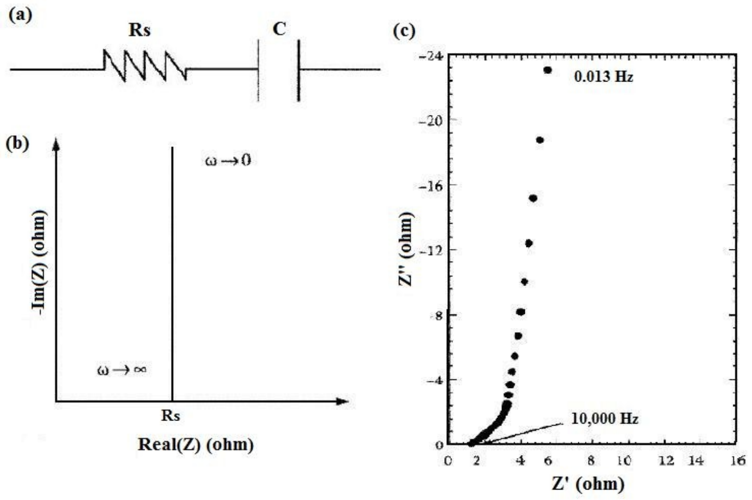

Figure 2.2. (a) Simple equivalent circuit with resistor and capacitor in series, (b) Nyquist plot for equivalent circuit, and (c) Nyquist plot for a real EDLC.[10]

However, the Nyquist plot for a real EDLC is much different than the model RC circuit, as shown in Figure 2.2c. The model circuit assumes two flat electrodes facing each other with a dielectric material of constant thickness between them. However, EDLCs use three dimensional porous electrodes, making the actual equivalent circuit much more complicated than the model *RC* circuit. In reality, the porous electrode can be thought of as a series of RC components that represent the delay in electrical response of the charging double layer as it starts from the interface with the bulk electrolyte and moves to the inner pore surfaces.[10] This corresponds to the Transmission Line Model developed by De Levie, which is illustrated in Figure 2.3.[83] When a potential difference is applied to two electrodes, ions from the bulk electrolyte transport to the electrode outer surface, inducing a resistance R_s due to ionic resistivity of the solution. The surface for double layer charging is at the top of the porous electrode, leading to a capacitance C_1.

More ions travel into the electrode pores, leading to another resistance R_1, until a second site for charging is found in the pore with a capacitance C_2. This pattern continues along the pores until the bottom of the electrode is reached, resulting in the equivalent circuit seen in Figure 2.3b.[10]

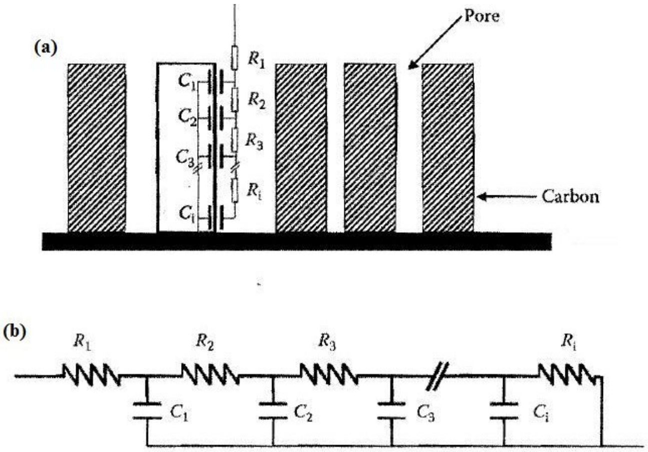

Figure 2.3. (a) Transmission line model for double layer formation in a porous carbon electrode and (b) the corresponding equivalent circuit.[10]

From this model, the Nyquist plots of real devices can be separated into three parts. At high frequencies, only the outer surface of the electrode is accessible to the electrolyte ions, resulting in a purely ohmic resistance R_S. In this frequency range, the device is under kinetic, or charge transfer, control. Often a semicircle will be seen in the Nyquist plot, which is associated with the surface properties of the porous electrode and corresponds to a *Faradaic* charge transfer resistance R_{CT}. As the frequency decreases, the migration of the ions into the electrode pores results in increased impedance due to the formation of multiple RC components. The device is now under diffusion, or mass transfer, control and both the capacitance and resistance depend on the frequency. Finally, at low frequencies, both the capacitance and resistance have reached their maximum values and the impedance starts resembling the vertical line of an ideal capacitor. Here, the capacitance is no longer dependant on the frequency.[10, 84]

3. Characterization methods

3.1. Composition, morphology, and surface chemistry

Perhaps the most useful technique for the characterization of highly porous materials is nitrogen sorption isotherms. This is a quick, easy, and powerful technique that accurately measures specific surface area, pore volume, average pore size, and pore size distribution. Additionally, it can provide information about pore morphology. The nitrogen sorption isotherms are measured using a Quantachrome NOVA 4200e. Samples are degassed at an elevated temperature under vacuum for at least 6 hours prior to measurement. The multipoint Brunauer-Emmett-Teller (BET) method is used to determine the total surface area. For the mesopore surface area, pore volume, and pore diameter, the Barrett-Joyner-Halenda (BJH) method is used. Micropore surface area and pore volume are determined using the t-method, and the micropore diameter is determined using the Dubinin-Astakhov (DA) method.

X-ray photoelectron spectroscopy (XPS) is used to determine the atomic composition of the porous carbons. Spectra are taken on a Surface Science Instruments S-probe spectrometer. X-ray spot size is 800 x 800 μm and the take-off angle is 55°, corresponding to a sampling depth of approximately 50-70 Å. Data analysis is carried out using the Service Physics ESCA 2000-A analysis program (Service Physics, Bend, OR). Images of the nanostructure were taken with a JEOL JSM-7000 scanning electron microscope (SEM). Energy dispersive X-ray spectroscopy (EDX) can also be used to perform elemental analysis on the SEM samples.

One very important characteristic for porous carbon electrodes is their wettability, as this is a measure of how well the electrolyte will interact with the material. A high affinity between the electrode surface and the electrolyte is important for double-layer formation.[85] With improved wettability, the electrolyte can more easily penetrate onto the carbon, leading to enhanced utilization of the available electrode surface. Additionally, the ionic conductivity at the interface increases, decreasing resistance and energy consumption by the device.[86-88] To investigate this property, contact angles were measured with the static sessile drop method using a VCA Optima goniometer. Surfaces were wet with approximately 1 μL of DI water and analyzed immediately after the droplet touched the sample. Multiple droplets were placed on each surface at different spots to avoid remeasuring an area that had already been wet. VCA OptimaXE software was used to measure angles on both the left and right sides of the droplet and the average angle was calculated.

3.2. Electrochemical characterization

Electrodes for electrochemical measurements are prepared from porous carbon by first grinding the large pieces into a fine powder. Approximately 3 wt% of polytetrafluoroethylene (PTFE) is incorporated as a binder. The mixture is rolled into sheets with a thickness of 0.07-0.08 mm (70-80 μm) and electrodes are punched out with a diameter of 10 mm. While thinner electrodes will have higher power density due to increased ion transport, they would not meet the mass and volume requirements for practical applications.[67] Each electrode is placed on a specially coated aluminum contact used as a current collector. The current collector is necessary to transfer the applied potential across the entire electrode, creating only a potential distribution in the thickness direction of the electrode perpendicular to the current collector.[67] A Celgard® porous film (monolayer polypropylene, thickness=25 μm, pore size = 0.043 μm) is sandwiched between the electrodes to prevent short-circuiting. Pressure is applied to the assembly to increase the contact between the electrodes and the current collectors, as inadequate contact is perhaps the largest source of resistance in the device and can greatly reduce the performance of the supercapacitor by causing the ESR to increase. The electrolyte used is tetraethylammonium tetrafluoroborate (TEATFB) in saturated 50/50 propylene carbonate/dimethylcarbonate. The electrode assembly is placed in a flat cell and electrolyte is added three times under an argon-rich environment. The samples are placed under a -70 kPa vacuum after each electrolyte addition to increase the penetration of the electrolyte into the pores. The final electrode assembly is sealed in the flat cell under argon to prevent oxygen contamination during testing. A schematic illustration of a flat cell and the actually device are shown in Figure 3.1.

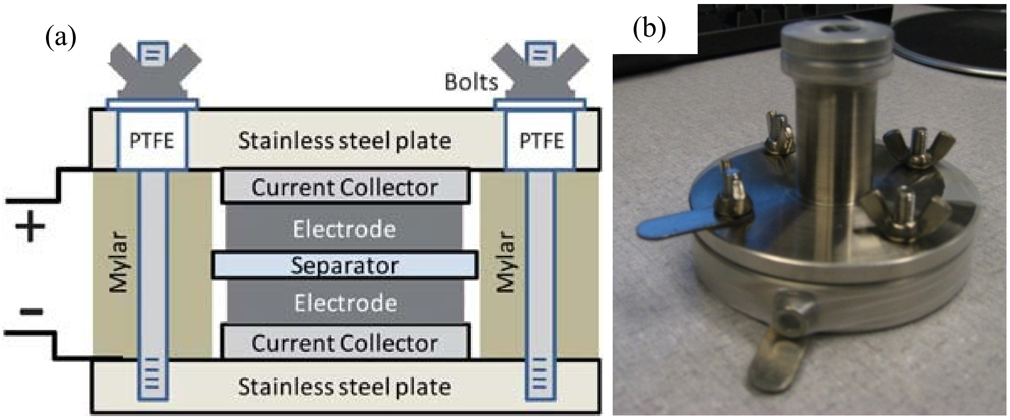

Figure 3.1. (a) Sample flat cell assembly,[89] and (b) the flat cell used here.

Three techniques are used for electrochemical characterization: cyclic voltammetry, galvanic cycling, and electrochemical impedance spectroscopy. Cyclic voltammagrams (CV) and galvanic cycles (GC) are taken using a Solatron 1287A.

Typically, the voltage range is between 0 and 2V. The CVs are measured at scan rates of 100, 50, and 10 mV/s and the GCs at 100, 50, 10, 5, 1, and 0.5 mA. Electrochemical impedance spectroscopy is performed using the Solartron 1287A in conjunction with a Solartron 1260FRA/impedance analyzer. The samples are cycled and pretreated for 10 minutes at the working voltage (e.g. 2V) before measurements. An AC voltage amplitude of 10 mV and frequency range of 0.1 MHz - 1 mHz is used for this scan.

Cyclic stability is another important characteristic of supercapacitors because it measures the durability and lifetime of the device. Materials that store charge based on double-layer formation theoretically have extremely long lifetimes as the energy is stored physically rather than through chemical reactions, as is seen in batteries. As such, lifetimes for carbon-based EDLCs can exceed 100,000 cycles while batteries have lifetimes that are usually less than 1000 cycles.[90] Still, supercapacitor performance degrades with cycling due to several reasons. First, there may be mechanical breakdown of the electrodes due to swelling during charging and discharging cycles. Additionally, unwanted impurities may cause chemical reactions that degrade the electrolyte.[67] This can lead to decomposition products accumulating in the pores, decreasing the accessible surface area and increasing resistance.[70] To measure the cyclic stability, devices were subjected to repeated charge and discharge to their selected working voltage up to 200 cycles at a rate of 0.1 mA.

The specific capacitance in F/g is calculated from the discharge slope during galvanic cycling according to the following equation:

$$C = \frac{4I\Delta t}{\Delta V m} \quad (2)$$

where I is the discharge current in amps, Δt is the discharge time in seconds, ΔV is the discharge voltage in volts, and m is the total mass of the active materials in both electrodes given in grams.[91] The capacitance based on specific surface area in F/m^2 is calculated by dividing the specific capacitance by the surface area of the electrode material in units of m^2/g. Volumetric capacitance in F/cm^3 is calculated by multiplying the specific capacitance by the density of both electrodes in g/cm^3.

4. ***Porous carbon synthesis***

4.1. Introduction

The highly porous carbon used here is synthesized through sol-gel processing. Using a sol-gel technique has advantages over other techniques because of the ease of processing and the ability to tune the porous structure. Tuning the morphology leads to easier accessibility of the electrolyte ions and reduced diffusion distances.[8] This allows for higher current density and faster response time.[92, 93] Additionally, the chemistry or surface chemistry of carbon cryogels can be tuned through incorporation of pre-selected precursors during the polycondensation process.

In general, an organic gel is made, which is composed of a three-dimensional solid network and liquid contained in the pores. The liquid is removed through specialized drying techniques such as supercritical drying or freeze drying, resulting in an aerogel or cryogel, respectively. The dried gel is then carbonized by heating at elevated temperatures in an inert atmosphere. This results in highly porous carbon with high surface area. Activation can then be performed to further increase the porosity and specific surface area, and tune the porous structure to meet the requirements of specific applications.

Synthesis of the organic gel takes place through a polycondensation reaction between precursors and a catalyst in the presence of a solvent. Perhaps the most common precursors are resorcinol and formaldehyde, but resorcinol and furaldehyde produce excellent gels as well.[57, 94] In resorcinol-formaldehyde systems, the formaldehyde reacts at the para and ortho sites on the resorcinol molecule, forming hydroxymethyl phenol. The hydroxymethyl group can react with another free para or ortho site to form a methylene bridge, or another hydroxymethyl group to form an ether bridge. As the reactions proceed, the substituted resorcinol rings condense with each other and form nanometer-sized clusters. Crosslinking of the surface groups on the clusters, such as -CH_2OH, results in a gel with a three dimensional network structure.[63, 95] This reaction is shown in Figure 4.1. The catalyst can be either basic or acidic, each resulting in different microstructures of the final porous carbon. Linear or slightly branched polymers are formed when under acid conditions, which then entangle and crosslink to form a gel. Under basic conditions, branched polymeric clusters are formed, which subsequently crosslink together.[56] A basic catalyst is often preferred because they create a higher density of crosslinked networks due to increase polymerization. This, in turn, creates stronger networks that are more resistant to shrinkage during solvent removal than more linear polymer chains with limited crosslinking.[57] Here, the catalyst is hexamethylenetetramine (hexamine, $(CH_2)_6N_4$), a basic organic catalyst containing nitrogen. Hexamine not only promotes the reaction between the precursors, but it also participates in the reaction, adding nitrogen to the carbon network in the form of amines, amides, imides, imines, and nitriles.[95] This is an important characteristic, as will be seen later. The precursors are mixed in the solvent first, then the catalyst is added. The mixture is sealed and cured in an oven at an elevated temperature for several days to allow for gelation and aging to strengthen the newly-formed three-dimensional gel network. The surface area and pore size of the gels can be controlled by adjusting the precursor to catalyst ratio and the solid content.[20]

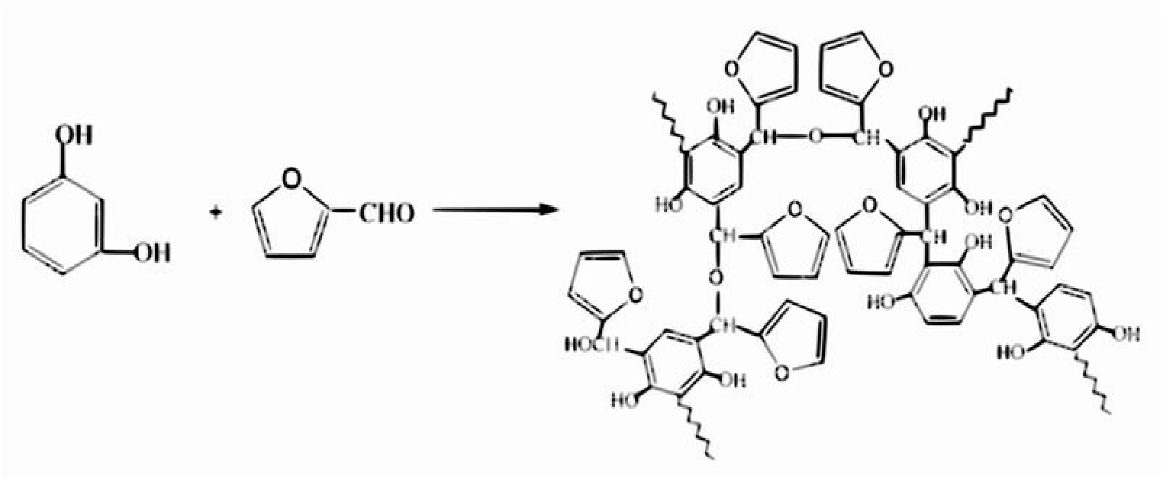

Figure 4.1. Schematic illustration of the resorcinol-furaldehyde polycondensation reaction.

After gelation and aging, the gel is dried. Specialized drying techniques such as supercritical drying or freeze drying are necessary because the capillary forces created when a gel is air dried could cause the porous structure to collapse. These techniques avoid the solvent's transition from liquid to gas, thereby avoiding any capillary forces. Supercritical drying requires the solvent to pass above its critical point at high pressure and temperature, where there is no longer a distinction between gas and liquid phases. Typically, a series of solvent exchanges are necessary to completely wash away the original solvent with liquid carbon dioxide at high pressure. The liquid carbon dioxide is then heated to a temperature above its critical point. Next, the pressure is gradually released, allowing the gas to escape and leaving the dried gel. Materials synthesized using this method are referred to as aerogels, and are highly porous with porosity up to 99.9% and specific surface area exceeding 1000 m^2/g.[96] While effective, supercritical drying generates a significant amount of waste due to the solvent exchange steps. Freeze drying, on the other hand, does not generate as much waste, and is an efficient alternative. This technique also avoids a solid-liquid transition by moving directly from the solid phase to the gas phase at low temperature and pressure. After the solvent has been pre-frozen to below its eutectic temperature, the pressure is reduced and a small amount of heat is supplied to the sample, allowing the solvent to sublime. The gas is pulled from the sample by using a cold trap at a lower vapor pressure to collect the solvent, leaving a dried gel that is referred to as a cryogel. Like aerogels, cryogels are highly porous and have high specific surface area.[97]

The dried sample is then pyrolyzed in nitrogen at high temperature to remove unwanted organics and increase the internal surface area. This process is often referred to as carbonization. Resorcinol-furfural gels are typically pyrolyzed at 900°C (or higher) to get complete carbonization, but some precursors may require temperatures up to 2000°C. At the beginning of pyrolysis, from about 200°C to 600°C, low molecular weight aliphatic and then aromatic compounds are released as gases. At the same time, cyclization and aromatization proceed in the sample, followed by polycondensation of the aromatic molecules. As the temperature approaches 600°C, oxygen, hydrogen, and other foreign atoms are released as compounds such as CO_2, CO, and CH_4. Above 800°C, usually only H_2 gas is released, and the sample can now be referred to as carbonaceous. However, some hydrogen and small amounts of foreign atoms, such as oxygen, nitrogen, and sulfur, still remain as impurities and their removal requires further heating to 2000°C. The carbonization process is highly dependent on the precursors and the pyrolysis heating conditions, including temperature, heating rate, and dwell time, and the final nanostructure of the carbon is determined by this process.[10]

Activation can be used to further open the porous structure and increase the specific surface area. This step is particularly important if there are concealed micropores, as these are inaccessible to the electrolyte and therefore not utilized for charge storage. There are two types of activation: chemical and physical. Chemical activation requires impregnating the aerogel or cryogel with certain chemicals, such as H_3PO_4, KOH, or NaOH, then heating at elevated temperatures usually between 450-900°C. It is believed that carbonization and activation take place simultaneously.[1, 98] Samples that are physical activated are heated at elevated temperatures in an oxidizing environment, such as oxygen gas, CO_2, air, or steam. In both chemical and physical activation, the carbon reacts with its environment and more disorganized carbon is removed, resulting in mass loss.[1] The level of mass loss depends on the activation conditions, such as time and temperature, and can be tuned for specific applications. For supercapacitors, the ideal level of activation is approximately 50%, as this leads to the maximum surface area due to the exposure of new micropores. A higher level of activation, fewer micropores are uncovered, leading to an increase in the average pore size and subsequently a decrease in the surface area.[20]

The final structure of the carbon cryogels is a three-dimensional network of interconnected nanoparticles.[57] The density and how these nanoparticles are assembled define the amount of micropores, mesopores, and macropores in the final structure. The structure can be tuned by adjusting the solid content and the ratios of precursors to catalyst. A low catalyst ratio (more catalyst) promotes a polymer-like structure with smaller nanoparticles making up the three-dimensional network, whereas a higher catalyst ratio (less catalyst) promotes a colloidal-like structure with larger nanoparticles.[61, 99] This is illustrated in Figure 4.2. SEM images of a typical carbon cryogel at three different magnifications are shown in Figure 4.3. Each piece of the powder-like sample shown at the lowest magnification is composed of interconnected nanoparticles that are less than 50 nm in diameter.

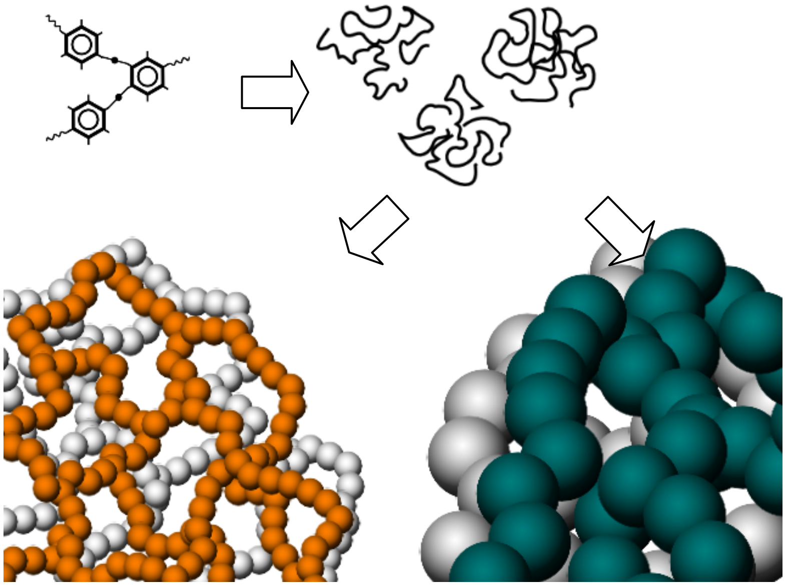

Figure 4.2. Mechanism for network formation. After polycondensation, the polymer chains form nanoparticle clusters, which assemble into interconnected three-dimensional networks. A low catalyst ratio (more catalyst) promotes a polymer-like structure formed from small nanoparticles, while a high catalyst ratio (less catalyst) promotes a colloidal-like structure with large nanoparticles. *Figure by Betzaida Batalla Garcia.*

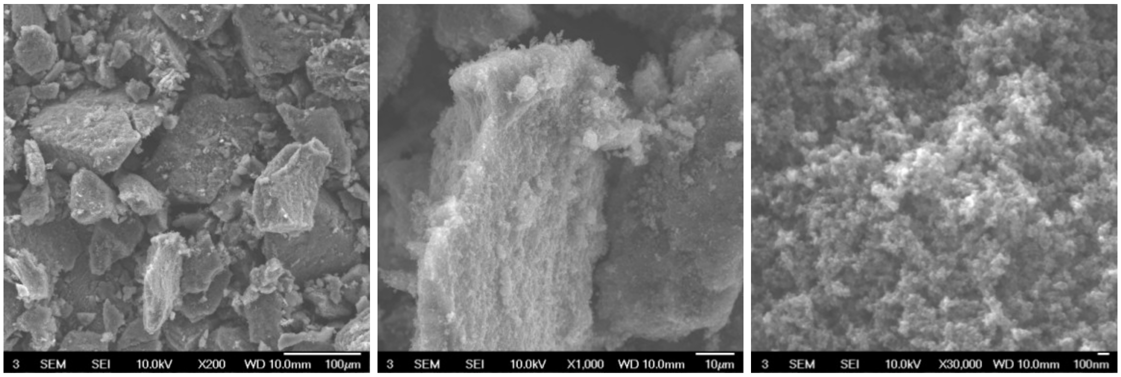

Figure 4.3. SEM images of activated carbon cryogel. The powder is composed of small, nanometer sized particles.

4.2. Effect of different catalyst ratios

To test the effect of different catalyst ratios on the pore structure of carbon cryogels, three resorcinol-furaldehyde organic gels were prepared using tert-butanol as the solvent and hexamine as the catalyst. The furaldehyde to resorcinol ratio was set to 2 and the solid content was set to 25%. Three different ratios of resorcinol to catalyst (RC) were used, specifically 25, 50, and 75. These samples are labeled as 25RC25, 25RC50, and 25RC75, respectively. According to previous studies, the RC ratio is the most important factor for determining the porous structure of the organic gel.[20] Each of these samples was subsequently freeze dried then pyrolyzed under N_2 at 900°C for 3 hours.

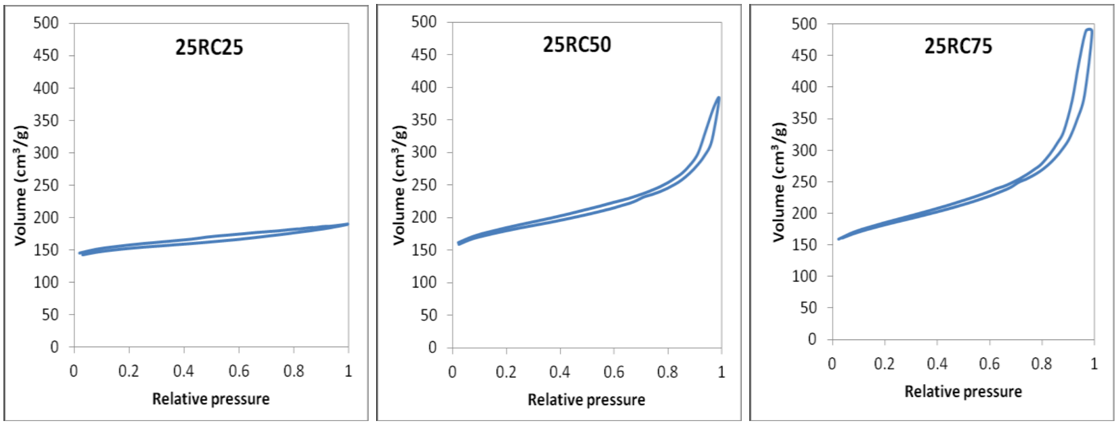

Figure 4.4. Nitrogen sorption isotherms for resorcinol-furaldehyde carbon cryogels with the same solid content (25%) but different resorcinol to catalyst (RC) ratios.

Table 4.1. Surface area, pore volume, and pore size for carbon cryogels with different RC ratios.

Sample	**Surface Area (m^2/g)**			**Pore Volume (cm^3/g)**		**Pore Diameter (nm)**	
	Total	**Mesopores**	**Micropores**	**Mesopores**	**Micropores**	**Mesopores**	**Micropores**
25RC25	437.8	40.4	365.4	0.059	0.204	3.7	1.0
25RC50	541.3	117.3	359.5	0.340	0.200	3.2	1.2
25RC75	551.7	164.9	316.3	0.524	0.178	3.2	1.3

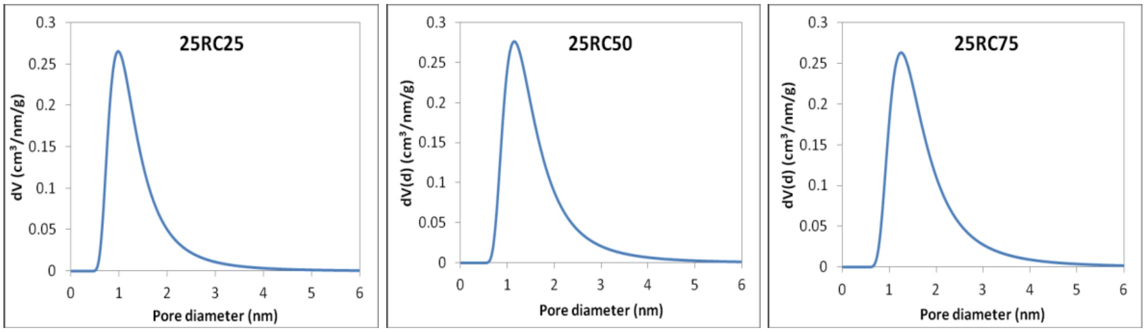

Figure 4.5. Micropore size distribution for carbon cryogels with different resorcinol to catalyst ratios.

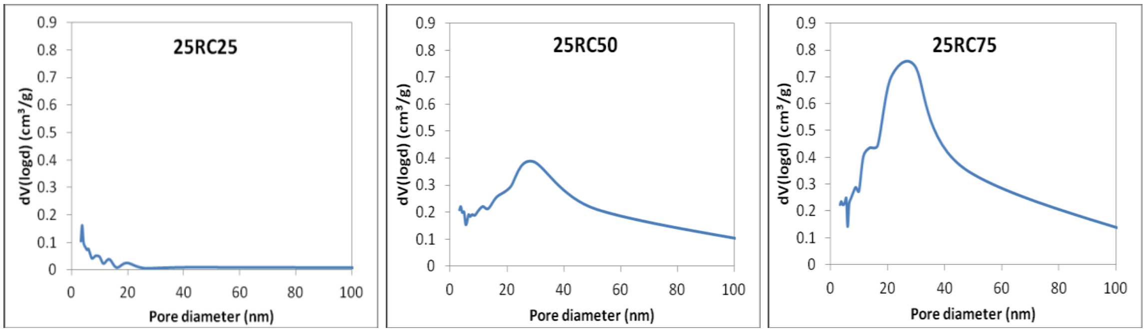

Figure 4.6. Mesopore size distribution for carbon cryogels with different resorcinol to catalyst ratios.

The effect of RC ratio is seen in the nitrogen sorption isotherms in Figure 4.4 and the corresponding data in Table 4.1. All three samples contain micropores, as can be seen by the high volume at relative pressures <0.2. The micropore size distributions shown in Figure 4.5 indicate that all three samples have approximately the same amount of micropores. From the data in Table 4.1, it can be seen that a lower RC ratio (more catalyst) results in a slightly larger micropore surface area and micropore volume, and a smaller average pore size. When there is a higher concentration of catalyst, the nucleation sites are more densely packed. This leads to less reactant being available per particle during growth, resulting in smaller particles. When these small particles interconnect to form a 3-dimensional networked structure, they can pack closer together, resulting in a smaller average pore size. When there is a lower concentration of catalyst, there are less nucleation sites. More reactant is available per particle, so the particles can grow larger and form a larger average pore size in the final interconnected structure. This mechanism is illustrated in Figure 4.7.[99]

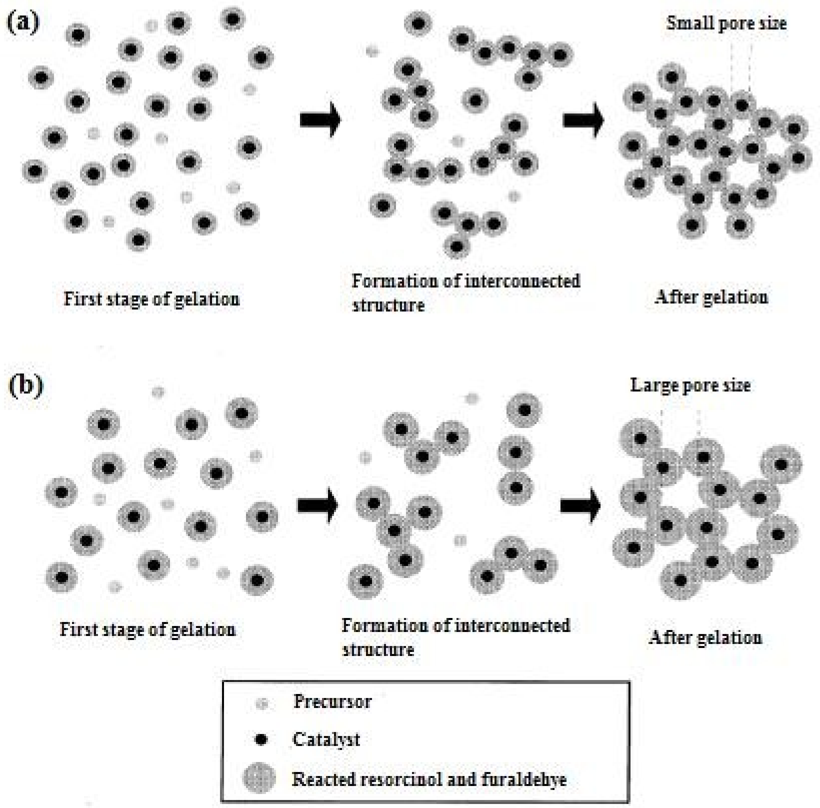

Figure 4.7. Mechanism for gelation with (a) more catalyst to create smaller pores and (b) less catalyst to create larger pores.[99]

As the RC ratio increases, the increase at ~0.5 relative pressure indicates that more mesopores are present. The 25RC75 sample appears to have the most mesopores of the three samples due to the steeper increase in volume in this region. The data in Table 4.1 supports this, as 25RC75 has the highest surface area and pore volume in the mesopore region. The 25RC25 sample, on the other hand, has very little pore volume from mesopores. The mesopore size distribution curves in Figure 4.6 clearly illustrate the differences in the three samples. These curves confirm the trends noted from the isotherms in Figure 4.4 and data in Table 4.1, showing the dramatic increase in pore volume as the catalyst ratio increases.

Finally, from the isotherms in Figure 4.4, the sharp increase in volume at relative pressures >0.8 signify a high occurrence of macropores for samples with higher RC ratios. Again, 25RC75 appears to have the most macropores of the three samples, as indicated by the highest maximum volume as the relative pressure approaches 1.

4.3. Activation

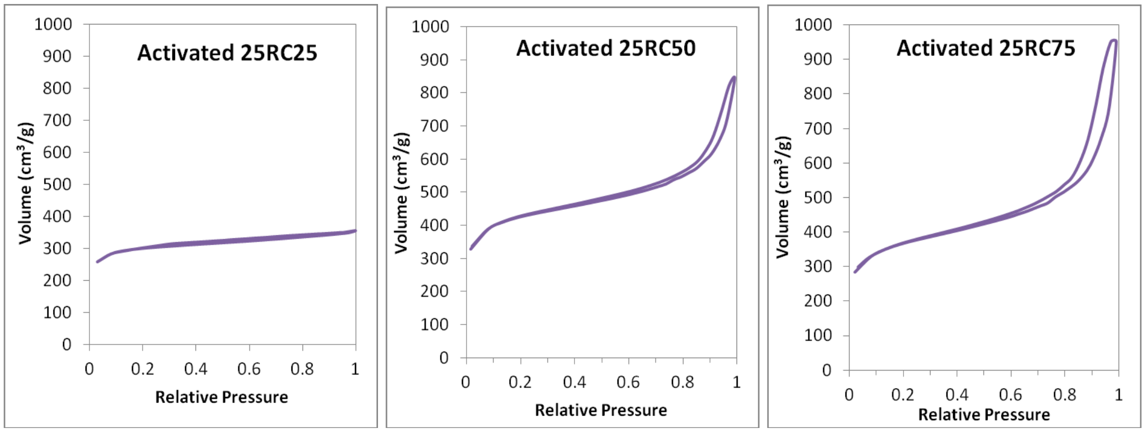

Figure 4.8. Isotherms for activated carbon cryogels with different RC ratios.

The effect of activation on 25RC25, 25RC50, and 25RC75 can be seen in Figure 4.8 and Table 4.2. As seen in the isotherms, all samples experience an increase in the amount of micropores. Table 4.2 shows that the contribution to surface area from micropores nearly tripled for 25RC50 and more than doubled for 25RC25 and 25RC75.

Furthermore, the contribution from this significant increase in the micropore surface area is reflected in the overall surface area, which also experiences a large increase. From the comparisons of micropore size distributions shown in Figure 4.9, it can be seen that activation dramatically increases the micropore volume as well. Similarly, there is also a large increase in the mesopore volume, as can be seen in the mesopore size distributions in Figure 4.10.

Table 4.2. Surface area, pore volume, and pore size for activated carbon cryogels with different RC ratios.

Sample	**Surface Area (m^2/g)**			**Pore Volume (cm^3/g)**		**Pore Diameter (nm)**	
	Total	**Mesopores**	**Micropores**	**Mesopores**	**Micropores**	**Mesopores**	**Micropores**
25RC25	865.2	51.68	742.3	0.094	0.414	3.2	1.6
25RC50	1281	224.5	926.7	0.710	0.507	3.2	1.4
25RC75	1117	301.0	706.1	1.005	0.390	3.2	1.5

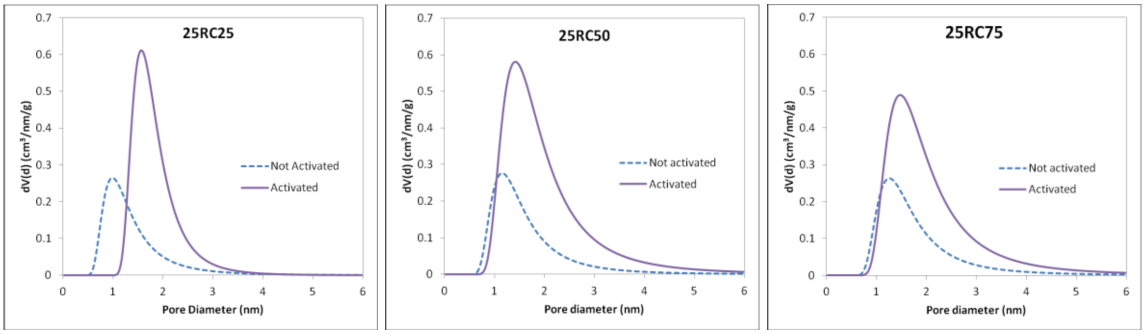

Figure 4.9. Micropore size distribution for activated carbon cryogels with different RC ratios. Activation increases the average micropore size and micropore volume.

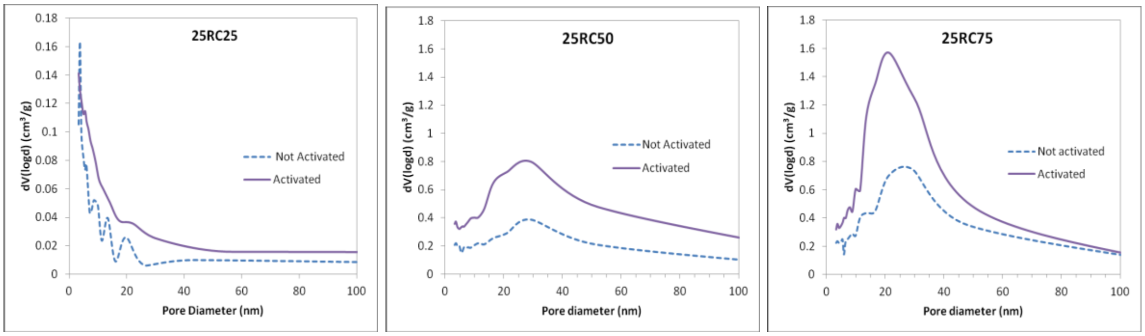

Figure 4.10. Mesopore size distribution for activated carbon cryogels with different RC ratios. Activation increases the mesopore volume.

4.4. Summary

Sol-gel processing can be used to make highly porous carbon with a tuneable pore structure. Synthesis begins with a polycondensation reaction between precursors resorcinol and furaldehyde and the catalyst hexamine in the solvent tert-butanol. A 3-dimensional crosslinked network of interconnected nanoparticles is formed, which must be dried using a specialized drying technique in order remove solvent from the pores without causing pore collapse. The resulting organic cryogel can be heated at high temperature in inert atmosphere to obtain the final porous carbon cryogel. Characteristics of the carbon such as surface area, pore volume, and pore size can be controlled through careful manipulation of the processing conditions. Activation processes can also be used to further open the pore structure and uncover hidden micropores, resulting in higher surface area and pore volume. The ease and flexibility of sol-gel processing makes it an ideal way to tailor the pore structure of porous carbon for advance applications, including supercapacitors with high performance.

5. Nitrogen-modified carbon for improved capacitance

5.1. Introduction

Pseudocapacitance can be induced through the introduction of foreign elements in highly porous carbon used for electric double layer supercapacitors.[100] These elements modify the electron donor/acceptor properties of the carbon, which in turn affect the charging of the electric double layer and provide pseudocapacitive *Faradaic* reactions.[73, 76, 101] The majority of work in this area has focused on introducing oxygen heteroatoms into the graphene layers of the carbon network because it closely associates with the carbon surface.[101] Often the oxygen functionalities are acidic in nature, inducing electron acceptor characteristics into the carbon material.[74] For example, quinone-type groups are believed to be involved in reversible redox reactions in aqueous electrolytes, transforming to hydroquinone at a characteristic potential, then back to quinone when the potential is reversed. Oxygen also exists in porous carbon in the form of carboxyl, lactone, pyrone, and phenolic functionalities.[10] Kim *et al.* proposed the following *Faradaic* reactions in aqueous electrolyte for CNTs oxidized through treatment in a concentrated H_2SO_4/HNO_3 solution:[85]

$$\text{- COOH} \leftrightarrow \text{- COO} + H^+ + e^-$$
$$> \text{C - OH} \leftrightarrow \; > \text{C=O} + H^+ + e^-$$
$$> \text{C = O} + e^- \leftrightarrow \; > \text{C-O}^-$$

This study and a number of others show that oxygen is beneficial in aqueous electrolytes.[69, 86, 88, 102] However, the issue remains that the presence of oxygen functionalities would be detrimental in organic electrolytes due to irreversible reactions between oxygen and the electrolyte ions.[70] An alternative element to oxygen that also induces pseudocapacitive reactions is necessary for use in devices that take advantage of organic electrolytes for their higher voltage window.

Recently, a number of studies have reported improved capacitance by using carbon enriched with nitrogen in aqueous electrolytes.[71, 72, 103-106] Preliminary results also show that nitrogen can improve capacitance in organic electrolytes,[72, 101, 105] but the number of these studies is still very limited. It is believed that nitrogen heteroatoms, like oxygen heteroatoms, contribute pseudocapacitance through *Faradaic* reactions such as the following proposed by Frackowiak[101] in acidic medium:

$$- C = NH + 2\,e^- + 2\,H^+ \leftrightarrow - CH - NH_2$$
$$- C - NHOH + 2\,e^- + 2\,H^+ \leftrightarrow - C - NH_2 + H_2O$$

Additionally, there have been several studies demonstrating that the addition of nitrogen changes the porous structure of the carbon, leading to increased surface area and pore volume. For example, activated carbon treated with solution of ammonium hydroxide and hydrofluoric acid resulted in the formation of surface nitrogen and fluorine functional groups. The modified activated carbons had increased specific surface area, total pore volume, and mesopore volume when compared to unmodified activated carbon.[73] Resorcinol-formaldehyde-derived porous carbon co-doped with nitrogen and boron showed an increase in specific surface area, micropore surface area, mesopore volume, and micropore volume.[107]

While the state of oxygen in graphite-like carbon is fairly well researched, the state of nitrogen in carbon is much less understood. Nitrogen can either be incorporated into the carbon network itself, substituting into the graphene sheets, or occur in the form of functional groups. Substitutional nitrogen atoms are often referred to as heteroatoms and they contribute to the formation of delocalized π electrons throughout the carbon matrix, creating electron-donor characteristics.[74]

The possible locations of the nitrogen in the carbon network as determined by XPS are shown in Figure 5.1. Two of the most common structures found include pyrrole groups with nitrogen in a 5-member ring and pyridine groups with nitrogen in a 6-member ring.[108] The presence of pyrrolic nitrogen adds two p-electrons to the delocalized π-electron system and a hydrogen atom, which is bound in the plane of the ring. Pyridinic nitrogen contributes one p-electron to the π-electron system and one lone electron pair in the plane of the ring.[108] Nitrogen also occurs as quaternary nitrogen, which is within a 6-member ring as well, but located at so-called "center" or "valley" positions.[74] Quaternary nitrogen is slightly more positively charged, resembling quaternary nitrogen in ammonium ions (NH_4^+).[109] Some researchers have argued about the prevalence of this positively charged quaternary nitrogen in carbon materials (it was originally observed in coals) due to the presence of delocalized electrons in the graphene sheet.[10, 108] It has been suggested that the quaternary nitrogen is a form of pyridinic nitrogen associated with a nearby hydroxyl or carboxyl group, which protonates the nitrogen by forming a hydrogen bridge.[108] Other researchers claim that the quaternary nitrogen has pyrrolic characteristics, increasing the electron-donor effect.[74] Nitrogen also occurs as a heteroatom in conjunction with oxygen, as seen in Figure 5.1. Like pyrrolic nitrogen, pyridone nitrogen adds two p-electrons to the π-electron system and a hydrogen atom bound in the plane of the ring.[74, 108]

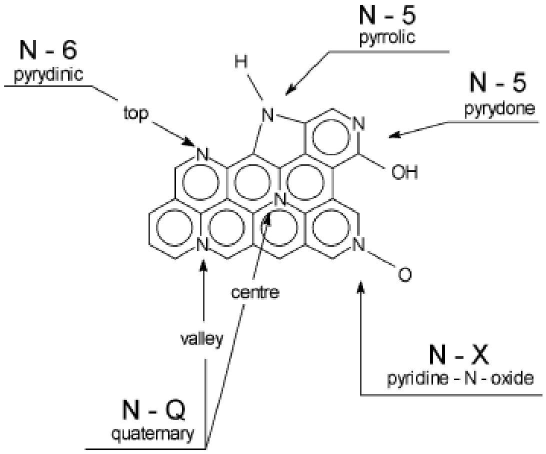

Figure 5.1. Locations of nitrogen heteroatoms in graphene structure.[74]

In addition to substituting into the carbon network, nitrogen can also be added to porous carbon in the form of surface functional groups. This is often at the relatively reactive graphene edges, where carbine- and carbine-type free edge sites are present.[10] Common functional groups include amines, imines, amides, and imides.[10, 74] There is also the possibility for functional groups to be bonded within the basal plane rather than at the edge atoms. The reactivity could be due to the presence of delocalized unpaired electrons, which occur due an uneven number of C-H bonds in the polyaromatic structure of graphene.[10]

Perhaps the best argument for this possibility is seen in curved graphenes such as carbon nanotubes (CNT), where such modifications are referred to as sidewall functionalization. CNT treated with nitrogen plasma resulted in the formation new broad peak in XPS spectra, attributed to amine, nitrile, amide, and oxime groups. Ultraviolet photoelectron spectroscopy valence band spectra also found that the N-treated CNT have lone pair electrons from sp^2 hybridized nitrogen.[110] Another research group found that treating CNT with ammonia plasma also resulted in amine, imine, nitrile, amide, and imide groups, with imine and amide groups occurring in the highest percentage.[111] It has also been shown that it is possible to functionalize sidewalls of CNTs with nitrogen containing groups. The disruption of the graphene π-bonding electron structure and increase in sp^3 hybridization as measured by Raman spectroscopy, and later confirmed by UV-vis-NIR spectroscopy, suggests that the nitrogen functional groups are covalently bonded to the sidewalls.[112] Theoretical[113, 114] and experimental[115, 116] studies conclude that the CNT remain conductive even with the disruption to the π-bonding structure, the degree of which depends on the type and concentration of the functional group.[113]

Adding nitrogen to the porous carbon network can be done in a number of different ways. One is to use nitrogen-containing precursors to obtain a carbon with nitrogen heteroatoms. Templated carbon prepared from melamine, an inexpensive polymer with 45 wt% nitrogen, was found to produce pseudocapacitance when tested in sulfuric acid as the electrolyte. The carbon contained pyridine, quaternary, and oxidized nitrogen in different amounts that varied with pyrolysis temperature. The relative amount of quaternary nitrogen increases as the pyrolysis temperature increases from 650°C to 1000°C. Adding a stabilization step, where the melamine precursor is burned in air at 250°C for 4 hours before pyrolysis, results in an increased amount of pyridine nitrogen when compared to non-stabilized carbon.[71] Heat treatment in oxygen or CO_2 results in an decrease in the relative amount of quaternary nitrogen accompanied by an increase of pyridine and pyrrole nitrogen.[109] A sample moderate surface area of 442 m^2/g but an N/C ratio of 0.24 achieved a capacitance of 204.8 F/g in 1 M H_2SO_4. This large capacitance is attributed to H^+ interacting with a pair of electrons provided by pyridine nitrogen on the periphery of the graphene sheets,[71] as illustrated in Figure 5.2.[75] This theory is further supported by a stabilized sample, which has a higher relative amount of pyridine nitrogen, achieving a similar capacitance of 200.1 F/g despite a lower surface area (256 m^2/g).[71] Other nitrogen-containing precursors that show similar effects include pyridine, quinoline, acrylonitrile, and polyaniline.[5, 39, 103, 105]

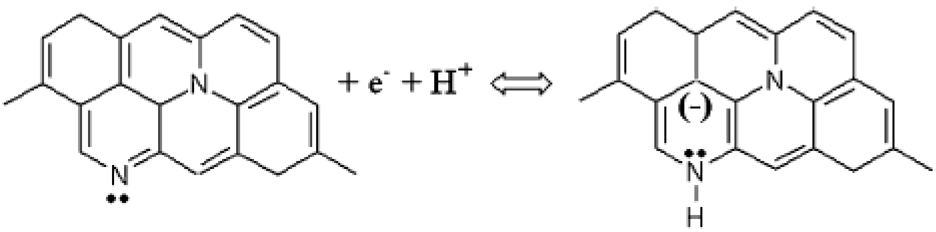

Figure 5.2. Proposed pseudocapacitive reaction mechanism for pyridinic nitrogen in aqueous electrolyte.[75]

Another method to introduce nitrogen into porous carbon is through heat treatments in the presence of nitrogen-containing chemicals. Ammoxidation, which involves heating samples in a mixture of ammonia and air, is another technique used to introduce nitrogen heteroatoms at different stages in the synthesis of activated carbon.[74, 117] An improvement in capacitance of up to approximately 10% was noticed for carbons that were subjected to ammoxidation after pyrolysis but before activation. It was observed, however, that all samples that underwent ammoxidation have less developed porous structure and total surface area than unmodified carbon. It is concluded that nitrogen somewhat blocks the out-gassing of carbon during activation. This is the most prominent when ammoxidation was performed on the precursor, resulting in a sample with the most nitrogen heteroatoms retained after activation.[74] As such, increasing the amount of nitrogen present as heteroatoms does not always increase the capacitance because it comes at the expense of surface area.[117] In order to achieve high capacitance, nitrogen must be added in such a way so as not to significantly decrease porosity and surface area.

There is ongoing research investigating the modification of the carbon surface with nitrogen-containing functional groups. In this way, nitrogen is on the surface of the carbon rather than in the bulk as heteroatoms. Recently, researchers have been looking at the deposition of nitrogen-containing conductive polymers, such as polyaniline and polypyrrole,[33, 118-120] on high surface area carbon. These polymers create *Faradaic* pseudocapacitance by reversibly oxidizing and reducing over a potential range. Polyaniline is perhaps the most researched because it has several oxidation-state structures.[121] Adding this nitrogen-containing polymer to carbon has been found to increase the capacitance significantly due to the combined effects from double-layer capacitance and pseudocapacitance.[33] However, special care must be taken to avoid blocking the carbon pores with the polymer during deposition. Additionally, swelling and shrinking of the polymers may lead to decreased cyclic stability.[33, 122]

The research performed here utilizes porous carbon both containing nitrogen heteroatoms in the bulk and with nitrogen modification on the surface of the pores. The carbon was first prepared using resorcinol and furfural as the precursors and hexamethylenetetramine (hexamine) as the catalyst. Historically, a metal ion catalyst such as NaOH has been used. However, this can leave impurities in carbon that are detrimental to the electrolyte used for supercapacitors, reducing the cyclic stability of the device. Hexamine, on the other hand, contains no metal ions and actually participates in the polycondensation reaction, adding nitrogen to the bulk. Resorcinol-furaldehyde gels catalyzed with hexamine have been studied previously and the pore structure has been optimized for supercapacitor and energy storage applications.[123]

Porous carbon is modified with nitrogen on the pore surfaces using hexamine. This nitrogen-containing molecule was selected for modification for multiple reasons. First, it is a small, cage-like molecule that can easily penetrate into the porous structure. Second, hexamine does not contain oxygen. Like metal ions, oxygen deteriorates the organic electrolyte, decreasing device lifetime. Two separate approaches were taken to modify the pore surfaces with nitrogen. First, organic gels were modified before freeze drying using a solvent exchange method. After modification, the gels were dried and pyrolyzed. Additionally, some samples were activated. The second method is to modify the porous carbon after activation. In each method, the goal is to maximize the amount of nitrogen coated on the pore surface while maintaining a high specific surface area.

5.2. Solvent exchange modification

5.2.1. Synthesis

To synthesize resorcinol-furaldehyde gels, the furaldehyde to resorcinol molar ratio is set to 2.5 and the resorcinol to hexamine molar ratio is 50. The resorcinol and furaldehyde are mixed together first, followed by the addition of the solvent tert-butanol. Hexamine is added last as the reactive catalyst. If the hexamine is not quick to dissolve, a small amount of deionized water is also added. The mixture is sealed and cured in an oven at 80°C for 7 days to allow for gelation and aging to strengthen the newly-formed three-dimensional gel network.

Nitrogen modification of the organic gel takes place during solvent exchange. This procedure has been used previously to dope porous carbon with ammonia borane for hydrogen storage applications.[107] Solvent exchange is performed by placing the gel in 10 times its volume of tert-butanol for 24 hours, then repeating the process two more times with fresh tert-butanol. For modification, 2 wt% of hexamine is dissolved in tert-butanol during the first solvent exchange step. The subsequent two steps are performed in pure tert-butanol to avoid precipitation of hexamine in the pores. After modification, the gels are dried under vacuum at -50°C in a Labconco FreeZone 1 L freeze dryer.

The dried sample is then pyrolyzed in nitrogen at high temperature to remove unwanted organic functional groups and increase the internal surface area. The resorcinol-furfural carbon is pyrolyzed at 900°C as previously studied,[124] as pyrolysis at this temperature or higher usually results in more complete carbonization.[10, 125] However, when carbon is heated above 850°C, the amount of nitrogen that can be found within the bulk dramatically decreases.[71, 101] According to a recent study of melamine, pyrolysis at 650°C results in the highest nitrogen to carbon ratio, while 750°C shows the highest surface area.[71] Pyrolysis at 700°C is expected to provide a favorable combination of both high surface area and high nitrogen content. Therefore, pyrolysis is performed at one of two temperatures: 900°C or 700°C. Resorcinol-furaldehyde gels that were pyrolyzed as-is at 700°C and 900°C are labeled as RF 700 and RF 900, respectively. Gels that were modified with nitrogen through solvent exchange were also pyrolyzed at 700°C and 900°C and labeled as RFN 700 and RFN 900, respectively. All four samples contain nitrogen heteroatoms in the carbon network from the reactive catalyst hexamine.

5.2.2. Composition and structure

Table 5.1. Chemical composition in atomic % from XPS.

Sample	**Composition (Atomic %)**		
	Carbon	Oxygen	Nitrogen
RF 700	96.6	2.7	0.7
RF 900	97.7	1.8	0.5
RFN 700	93.0	4.4	2.7
RFN 900	97.2	2.0	0.8

Results from XPS are shown in Table 5.1. RFN 700 has the highest nitrogen content at 2.7 atomic %. Pyrolysis of nitrogenated carbon at this lower temperature results in a nitrogen content that is more than three times higher than pyrolysis at 900°C, as high temperature favors the removal of nitrogen.[101] One explanation for why nitrogen is preferentially removed at 900°C is the difference in bond strength between carbon-carbon bonds and carbon-nitrogen bonds. The carbon-carbon bond has a bond strength of approximately 715 kJ/mol while the carbon-nitrogen bond has a strength of 174-300 kJ/mol depending on the type of bonding.[126] Since the carbon-nitrogen bond is weaker, it will break more readily than the carbon-carbon bond, leading to more nitrogen loss at higher pyrolysis temperatures. However, a higher oxygen content is also seen in RFN 700 when compared to the other samples.[105] Further experiments are underway to determine the reason for this. One possibility is that the surface modification blocked the removal of oxygen from the underlying carbon network. Also, because RF 700 has increased oxygen content when compared to RF 900, it is possible that less oxygen is removed at this lower pyrolysis temperature.

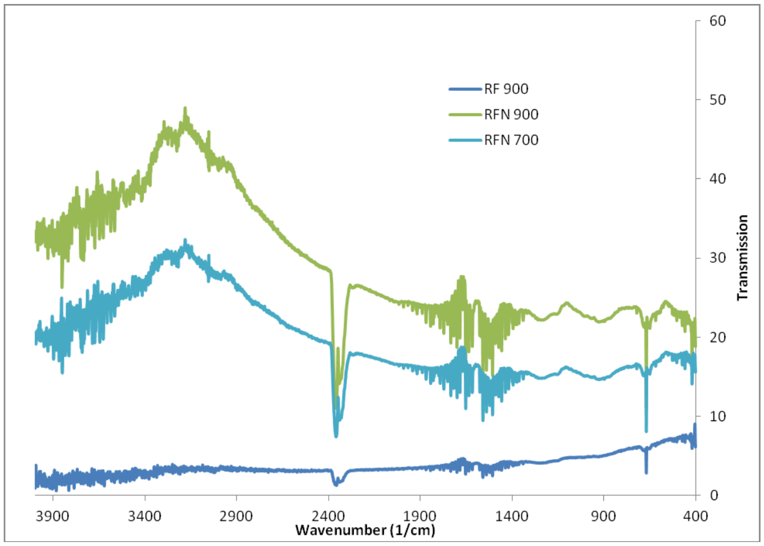

Figure 5.3. FTIR transmission spectra for unmodified carbon and nitrogen-modified carbon prepared at different pyrolysis temperatures.

FTIR was used to further characterize the nitrogen modified carbon samples pyrolyzed at different temperatures. Transmission spectra are shown in Figure 5.3. The nitrogenated carbon samples show evidence of nitrogen bonds in three areas of the spectrum. The peaks between 3500 and 3300 cm^{-1} can be attributed to N-H bonds. Near 2400 cm^{-1}, there are double and triple bonds of C and N. Lastly, there are C-N single bonds near 660 cm^{-1}.

Nitrogen sorption was used to determine how the surface area, pore volume, and pore diameter change with nitrogen modification and different pyrolysis temperatures. Isotherms are shown in Figure 5.4 and the corresponding data is presented in Table 5.2. For the unmodified samples, the surface area increases when the temperature is raised from 700°C to 900°C. The higher temperature is necessary to remove unwanted functional groups more completely and open the porous structure. From the micropore size distribution in Figure 5.5a and the mesopore size distribution in Figure 5.6a, it can be seen that increasing the pyrolysis temperature from 700°C to 900°C for unmodified carbon also increases the pore volumes. The increase is much more significant for mesopores, as noted in Table 5.2. The pore size also shifts to a larger diameter, evidence that the higher pyrolysis temperature is helping to open the pore structure.

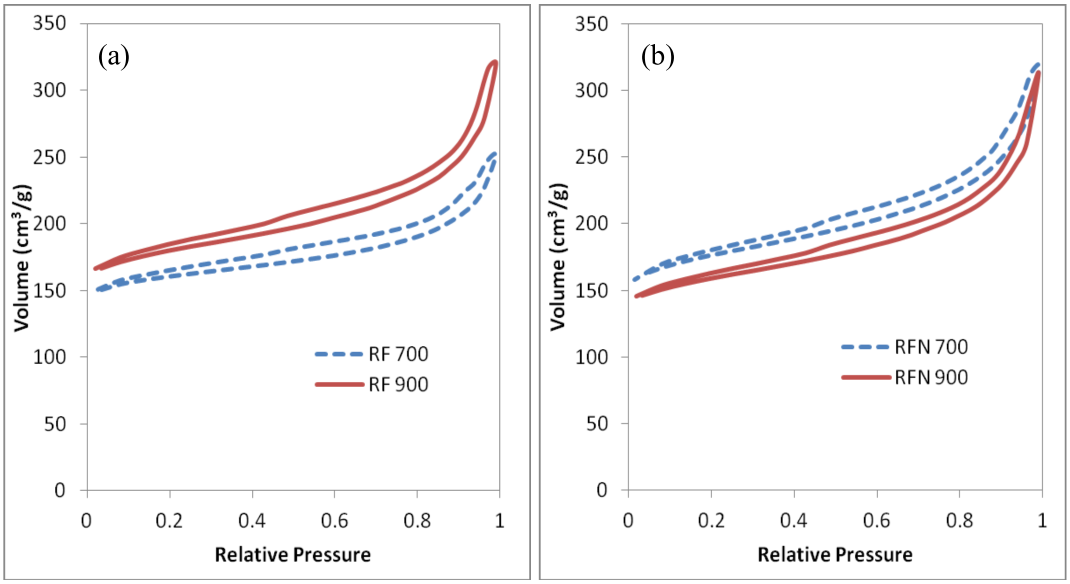

Figure 5.4. Nitrogen sorption isotherms for (a) unmodified RF 700 and RF 900, and (b) nitrogenated RFN 700 and RFN 900.

Table 5.2. Surface areas, pore volumes, and pore diameters of each sample based on nitrogen sorption analysis.

Sample	Surface area (m^2/g)			Pore Volume (cm^3/g)		Pore Diameter (nm)	
	Total	Mesopores	Micropores	Mesopores	Micropores	Mesopores	Micropores
RF 700	461.9	60.1	379.8	0.150	0.213	3.7	1.0
RF 900	525.5	89.4	399.9	0.236	0.224	3.7	1.1
RFN 700	514.3	96.3	375.4	0.242	0.213	3.7	1.1
RFN 900	468.7	90.9	340.1	0.259	0.191	3.7	1.1

For the nitrogen-modified carbons, the opposite behavior is noticed. RFN 700 has higher overall surface area than RFN 900, in addition to higher surface area in the mesopore and micropore regions. The micropore size distribution in Figure 5.5b shows that the nitrogen-modified carbon pyrolyzed at 700°C also has a slightly higher pore volume than the sample pyrolyzed at 900°C. From the mesopore size distribution in Figure 5.6b, the pore volume is also higher for mesopores below 20 nm when the pyrolysis temperature is lower.

As shown in a previous study that modified carbon with ammonia borane,[107] chemical modification during solvent exchange results in an increased surface area after pyrolysis. This trend can be seen when comparing RF 700 to RFN 700. However, the surface area is significantly smaller for RFN 900 when compared to RF 900. This surface area decrease is seen in the micropore region. RFN 900 also has a decreased micropore volume, while maintaining a similar micropore diameter to RF 900. This suggests that the total amount of micropores in RFN 900 is decreased. The surface nitrogen is affecting the pyrolysis behavior of the underlying carbon at higher temperatures, particularly in the formation and/or retention of micropores and smaller mesopores.

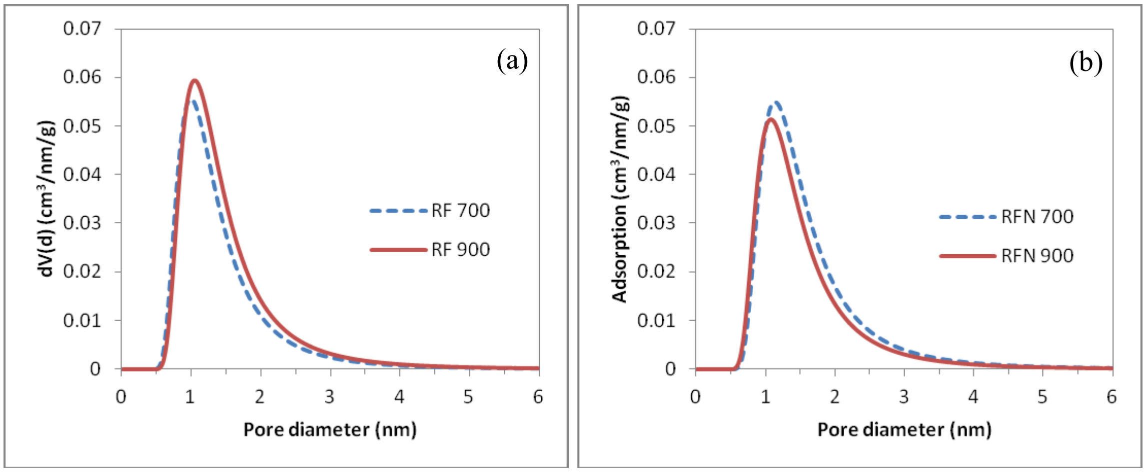

Figure 5.5. Micropore size distributions for (a) unmodified and (b) nitrogen modified carbon pyrolyzed at 700°C or 900°C.

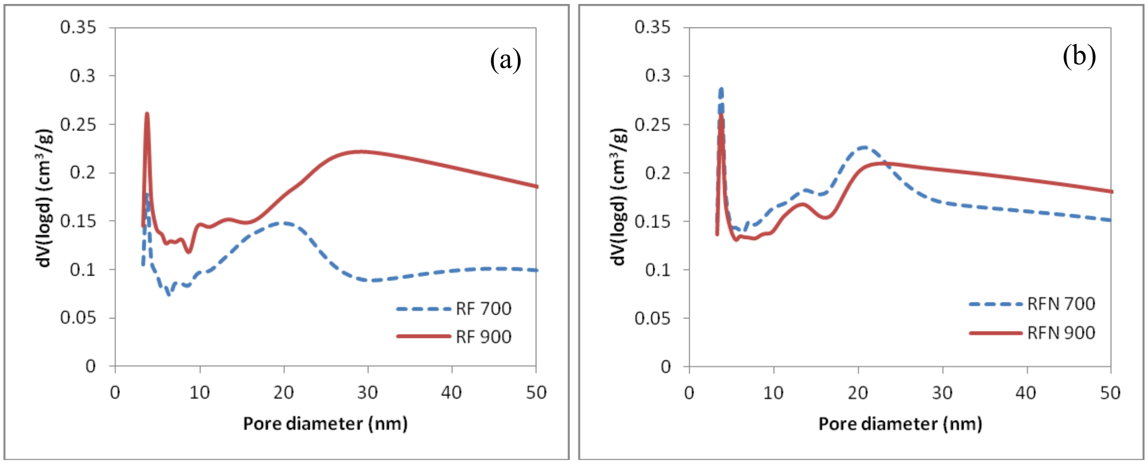

Figure 5.6. Mesopore size distributions for (a) unmodified and (b) nitrogen modified carbon pyrolyzed at 700°C or 900°C.

Contact angles were measured to assess how the nitrogen modification affects the surface properties of the carbon. Since the wettability is an indication of how the electrolyte will interact with the material, all measurements were performed with samples that had been rolled into sheets for making electrodes. As illustrated in Figure 5.7, the samples modified with nitrogen had very different wetting behavior than the unmodified carbon. While droplets formed on the RF 700 and RF 900, the surface of the RFN 700 and RFN 900 wet out such that a contact angle was impossible to measure. Since all of the samples have relatively similar pore structure, this drastic change in surface chemistry can be attributed to modifying the carbon with nitrogen. This is further supported when comparing the two unmodified carbon samples. As evidenced in Figure 5.7 and Table 5.3, RF 700 has a slightly smaller contact angle than RF 900. It can be concluded that the better wettability of RF 700 is because of the higher nitrogen content in the bulk carbon network due to the lower pyrolysis temperature of this sample.

Other researchers have noticed a similar effect with increasing nitrogen content. During H_2O adsorption-desorption analysis, carbon containing nitrogen experienced rapid H_2O adsorption at a lower pressure than carbon without added nitrogen. Because of the similar micropore size between the two samples, the difference in uptake pressure can be attributed to the carbon surface chemistry alone. While both samples have some oxygen present, the N-free carbon had double the oxygen content, suggesting that the presence of nitrogen groups in the carbon is more effective for increasing the hydrophilic nature.[127]

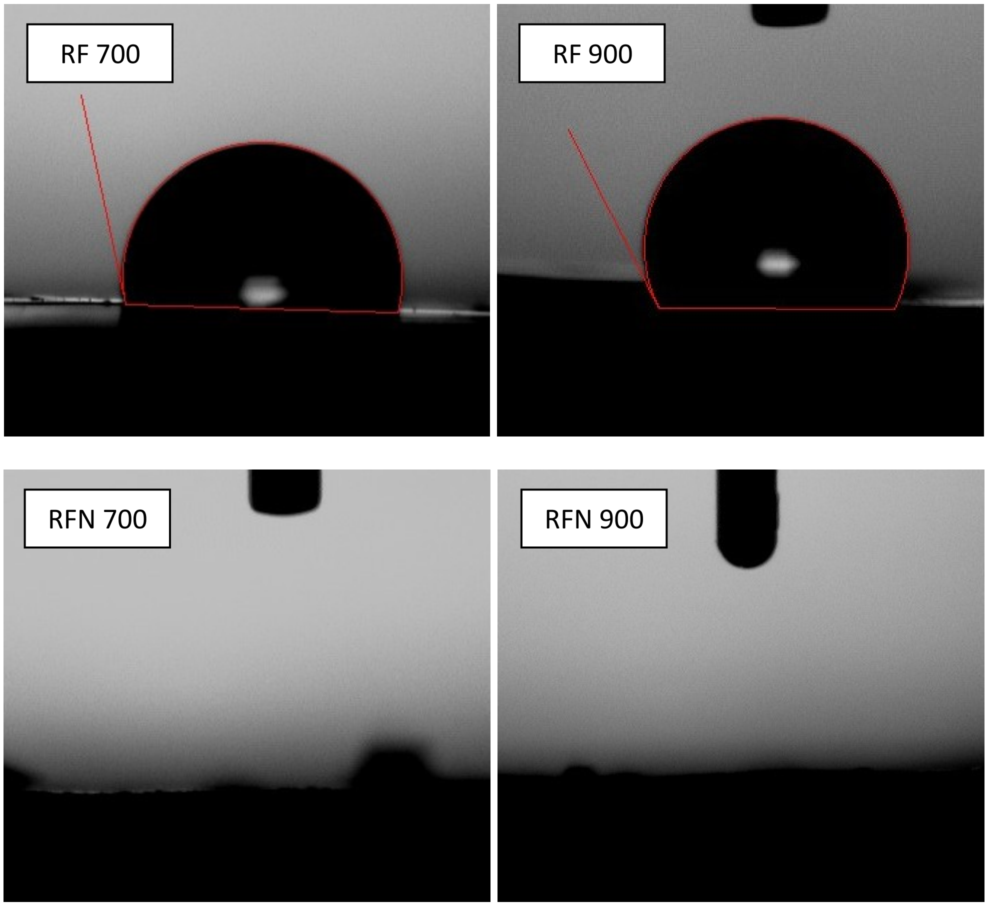

Figure 5.7. Images showing the wettability of unmodified and nitrogen-modified carbons. Each image was taken immediately after the droplet touched the surface. The uneven surfaces in RFN 700 and RFN 900 are from the edges of the sample rolling up and did not affect the measurements.

Table 5.3. Average contact angles measured immediately after the droplet touched the surface.

Sample	**RF 700**	**RF 900**	**RFN 700**	**RFN 900**
Contact angle	102.3°	118.3°	Complete wetting	Complete wetting

5.2.3. Electrochemical analysis

To test the supercapacitor performance of the four samples, asymmetric two-electrode devices were prepared. The working electrode was made of the sample of interest and the counter/reference electrode was RF 900 for all devices. Symmetric devices that use the same material for both electrodes did not work, with the exception of the RF 900/RF 900 device. This hints at the mechanism for how nitrogen creates pseudocapacitance, which will be discussed later.

CVs taken at a scan rate of 10 mV/s are shown in Figure 5.8. The fairly rectangular shape of RF 900 indicates capacitive behavior from the formation of an electric double layer. RFN 700, on the other hand, exhibits small, broad peaks in addition to the rectangular shape. This indicates pseudocapacitive reactions from nitrogen on the interior surface of the porous carbon. RFN 900 also shows these pseudocapacitive peaks, suggesting that some nitrogen remains on the surface despite the higher pyrolysis temperature. Nitrogen in the bulk of the carbon network does not appear to contribute to pseudocapacitance as much as surface nitrogen, as the RF 700 CV shows no evidence of pseudocapacitive reactions. RF 700 also indicates increased resistance to rapid charging, which is likely due to the smaller surface area of this sample, particularly in the mesopore region.

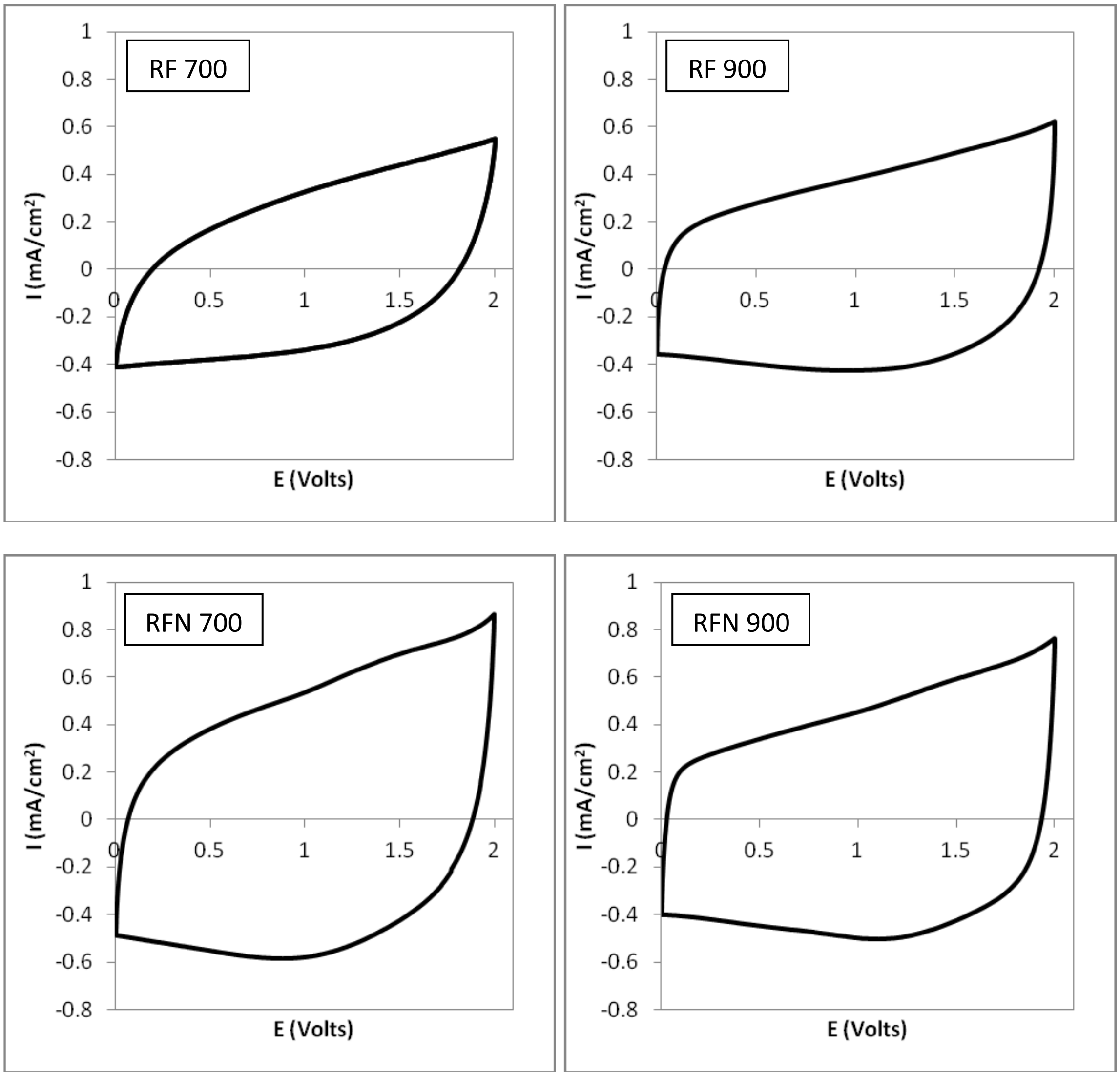

Figure 5.8. CVs of unmodified and nitrogenated carbon samples. Both RFN 700 and RFN 900 show small, broad peaks, indicative of pseudocapacitive reactions.

The exact mechanism for how nitrogen is inducing pseudocapacitance in these samples is still unknown at this time. However, following the reactions discussed earlier for nitrogenated carbon in aqueous medium,[101] new reactions can be proposed for nitrogenated carbon in organic electrolytes. It is believed that pseudocapacitance arises from *Faradaic* reactions induced by lone electron pairs from the nitrogen groups interacting with the cations in the electrolyte. The following are reactions that could be taking place on the nitrogenated carbon surface:

$$- C - NH_2{:} + (C_2H_5)_4^+ \leftrightarrow - C - NH_2 : (C_2H_5)_4^+$$

$$- C = NH{:} + (C_2H_5)_4^+ \leftrightarrow - C = NH{:}\ (C_2H_5)_4^+$$

$$- C \equiv N{:} + (C_2H_5)_4^+ \leftrightarrow - C \equiv N{:}\ (C_2H_5)_4^+$$

Galvanic cycling further illustrates pseudocapacitance and resistance in the samples. Figure 5.9 shows the GCs measured at 0.5 mA. All samples exhibit non-linear charging behavior characteristic of pseudocapacitive reactions.[124] The specific capacitance is calculated from the discharge slopes of these curves using Equation 1. The results are shown in Table 5.4. RFN 700 has the most gradual discharge slope, resulting in the highest specific capacitance. The capacitance is almost twice that of either of the unmodified carbon samples. It is also higher than RFN 900, suggesting that it is the nitrogen retained on the surface of the carbon network that is adding to the capacitance through pseudocapacitive reactions.

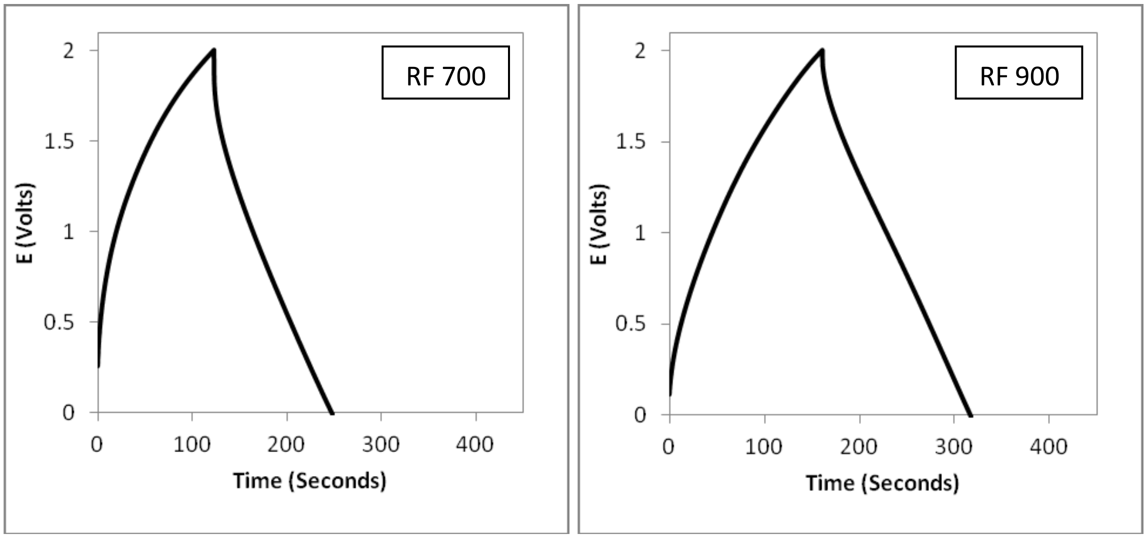

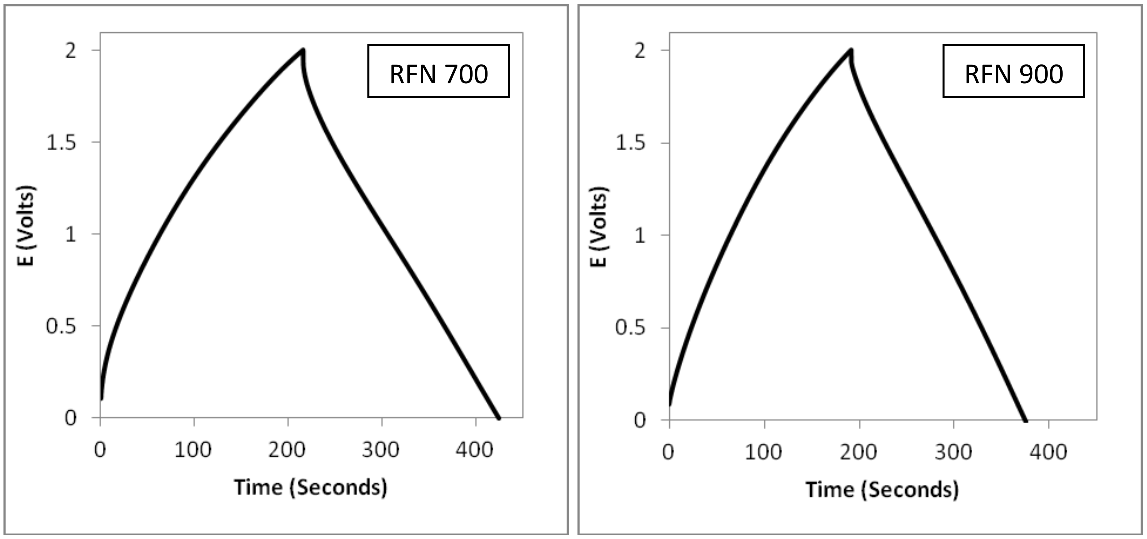

Figure 5.9. GCs of unmodified and nitrogen-modified carbon. RFN 700 shows the most gradual discharge slope, suggesting the highest specific capacitance.

Table 5.4. Capacitance based on mass, surface area, and volume. RFN 700 shows the highest capacitance in all three areas. These samples have not been optimized for high capacitance values.

Sample	**Specific Capacitance (F/g)**	**Capacitance Based on Total Surface Area (F/m^2)**	**Volumetric Capacitance (F/cm^3)**
RF 700	9.6	0.021	5.8
RF 900	10.1	0.019	6.0
RFN 700	18.6	0.036	18.0
RFN 900	11.5	0.025	6.9

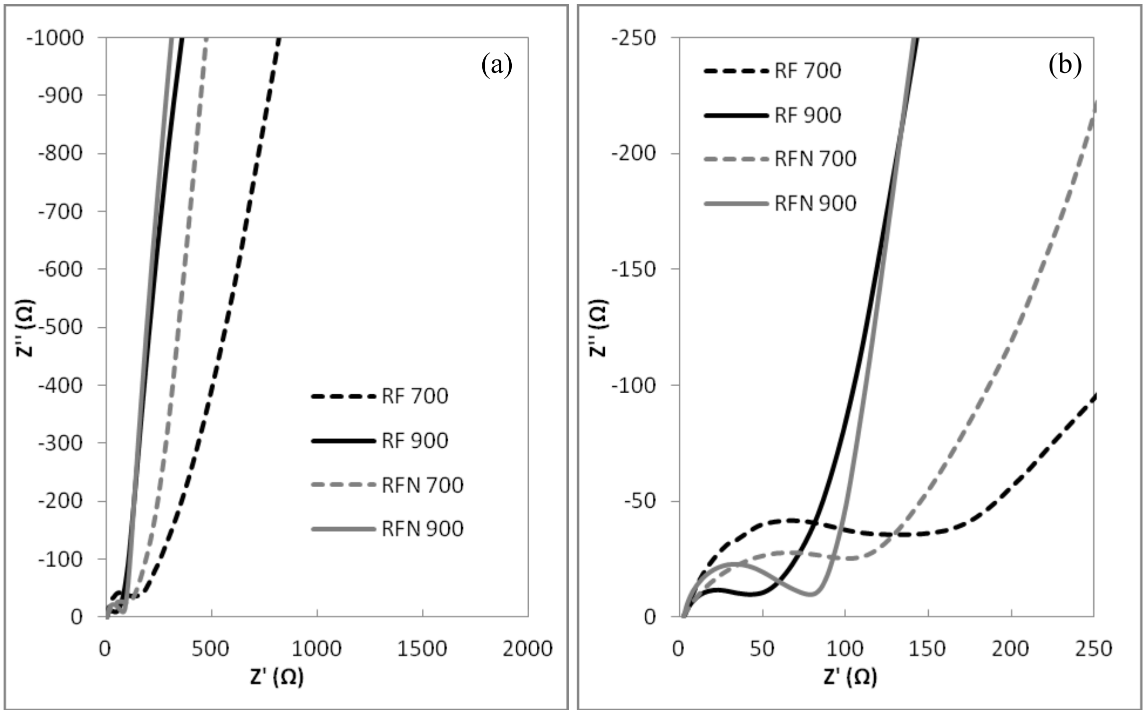

Figure 5.10. Nyquist plots at (a) high and low frequencies, and (b) high frequencies only. RFN 700 shows the highest capacitance despite a higher diffusivity resistance and charge transfer resistance.

Table 5.5. Equivalent series resistance (ESR). Both pyrolysis at higher temperature and the addition of nitrogen decreases the ESR.

Sample	**RF 700**	**RF 900**	**RFN 700**	**RFN 900**
ESR (Ω)	3.55	2.74	2.84	2.28

Electrochemical impedance spectroscopy can provide insight into how the nitrogen modification is affecting the performance of the samples. Nyquist plots are shown in Figure 5.10. At low frequencies, RF 700 exhibits the highest diffusivity resistance, as seen by the more gradual slope at higher Z’ values. Nitrogen sorption illustrated that pyrolysis of unmodified carbon at 700°C results in smaller micropores and lower mesopore surface area, which hinders the diffusion of the electrolyte ions through the pores. When the pyrolysis temperature is raised to 900°C, the diffusivity resistance decreases because the pores become larger. This increases the capacitance due to improved electrolyte penetration and therefore double-layer formation. RFN 700 also shows evidence of high diffusivity resistance at low frequencies, which can be attributed to the presence of pseudocapacitive reactions.[124] When the nitrogenated carbon is pyrolyzed at 900°C, the sample loses some of the evidence of *Faradaic* reactions, behaving very similarly to the unmodified carbon pyrolyzed at the same temperature.

Values for the equivalent series resistance (ESR) from EIS are listed in Table 5.5. The ESR is a measure of the ohmic resistance from several factors, such as the electrolyte resistance, the contact resistance between the current collector and carbon electrode, and the intrinsic resistance of the carbon. Because the electrolyte processing conditions are the same for all samples, it can be assumed that the intrinsic resistance of the carbon has the most influence on the ESR. By increasing the pyrolysis temperature from 700°C to 900°C, the ESR decreases for both unmodified carbon and nitrogen-modified carbon. This suggests that the higher pyrolysis temperature results in more complete carbonization of the organic gel, creating a more conductive material. However, modifying with nitrogen also works to decrease the ESR, suggesting that nitrogen also helps to increase the conductivity of porous carbon.

Differences in charge transfer resistance (R_{CT}), an indication of how charged ions in the electrolyte interact with the electrode surfaces, are evident at high frequencies as seen in Figure 5.10b. RF 700 has the highest R_{CT}, due to the functional groups that remain on the carbon surface from the low pyrolysis temperature. Likewise, RF 900 has the smallest R_{CT}, since the elevated temperature is high enough to remove the unwanted functional groups during pyrolysis. The larger R_{CT} of RFN 700 is an artifact of nitrogen modification on the surface of the carbon. This is further supported by the decrease in R_{CT} for RFN 900, since nitrogen in the sample is lost at this higher pyrolysis temperature. Still, some nitrogen is retained in RFN 900 since the R_{CT} is larger than RF 900. While modifying carbon with nitrogen groups does increase the charge transfer resistance in the samples, the added pseudocapacitance is significant enough to greatly increase the overall capacitance.

While it can be seen that nitrogen both in the bulk and on the surface of the carbon increases the capacitance, as seen by the superior capacitance of RFN 700, the values obtained here are relatively low. According to nitrogen sorption, the total surface area of all four of these samples is relatively small, as some studies of activated carbon have achieved surface areas exceeding 2000 m^2/g.[20] As such, Table 5.4 also shows the capacitance normalized to surface area. These values are relatively low as well, which is believed to be an artifact of the low mesopore surface area in these samples. Without adequate mesopores in the porous carbon, penetration of the electrolyte is limited by pores that are too small to allow the ions to pass through easily. The total accessible surface area is most likely much lower than the total surface area measured by nitrogen sorption.

5.2.4. Activation

5.2.4.1. Activating the reference electrode

Activation is often used to increase the specific surface area of porous carbon, making more active material accessible to the electrolyte. For example, activating a resorcinol-furaldehyde carbon that was pyrolyzed at 900°C results in increase in specific surface area from 525.2 m^2/g to 1117 m^2/g. A new supercapacitor device was then constructed using RFN 700 as the working electrode and this activated carbon as the reference electrode. This results in a significant increase in the capacitance when compared to the RFN 700 device using unactivated RF 900 carbon as the working electrode. Using unactivated carbon as the reference electrode, the specific capacitance is 18.6 F/g. This increases to 52.1 F/g when activated carbon is used as the reference electrode. CVs and GCs comparing these two devices are shown in Figure 5.11. The activation process increases the surface area of the unmodified carbon electrode, making more active material available for double layer formation. The voltage drop in the GC curves also decreases, indicating that there is less resistance for the electrolyte ions after activation due to a more open porous structure.

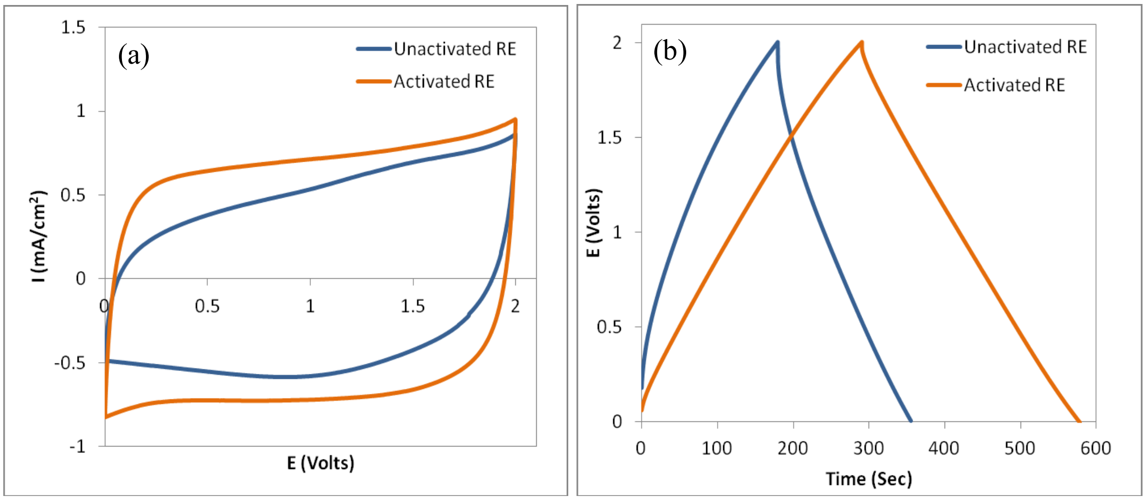

Figure 5.11. (a) CV and (b) GC for devices using RFN 700 as the working electrode and either unactivated or activated RF 900 as the reference electrode (RE).

5.2.4.2. Activating nitrogen modified carbon

The surface area of the nitrogen modified carbon used in these devices is still relatively low, so activation might be beneficial to increasing this value as well. However, as was seen with nitrogen sorption and contact angle measurements, the nitrogen coated on the surface of the pores affects the chemistry, and therefore heating behavior, of the underlying porous carbon. For unmodified resorcinol-furaldehyde carbon (e.g. RF 900), activation is performed in dry air at 420°C for 4 hours with a ramp rate of 5°C/min. This results in the desired 50% mass loss and an increase in specific surface area from 525.2 m^2/g to 1117 m^2/g. However, activation of RFN 700 under the same conditions results in a mass loss of 85%. By decreasing the activation time to 2 hours, there is a mass loss of 75%. Finally, an acceptable mass loss of 53% results when the sample is activated for only 28 minutes.

The level of activation for the nitrogenated carbon has an effect on the supercapacitor performance, as can be seen in the CVs and GCs shown in Figure 5.12 and Figure 5.13, respectively. The corresponding data is listed in Table 5.6. Using activated RF 900 as the reference/counter electrode, the decreasing activation time improves the specific capacitance of RFN 700, with 28 minute activation showing a capacitance of 82.4 F/g. This is also a significant improvement over the RFN 700 without activation, which had a capacitance of only 52.1 F/g.

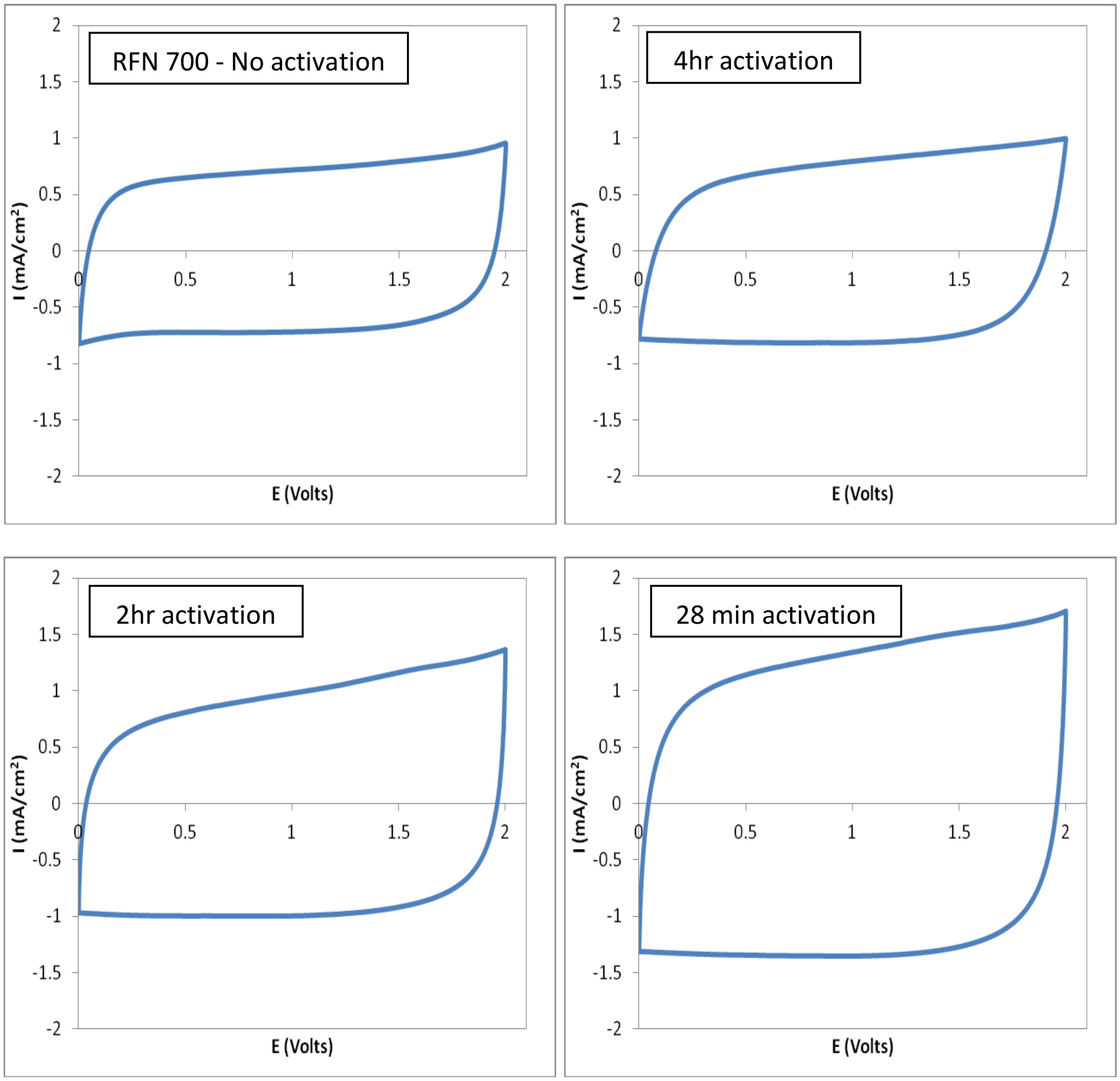

Figure 5.12. CVs taken at 10 mV/s for samples prepared from RFN 700 with different levels of activation.

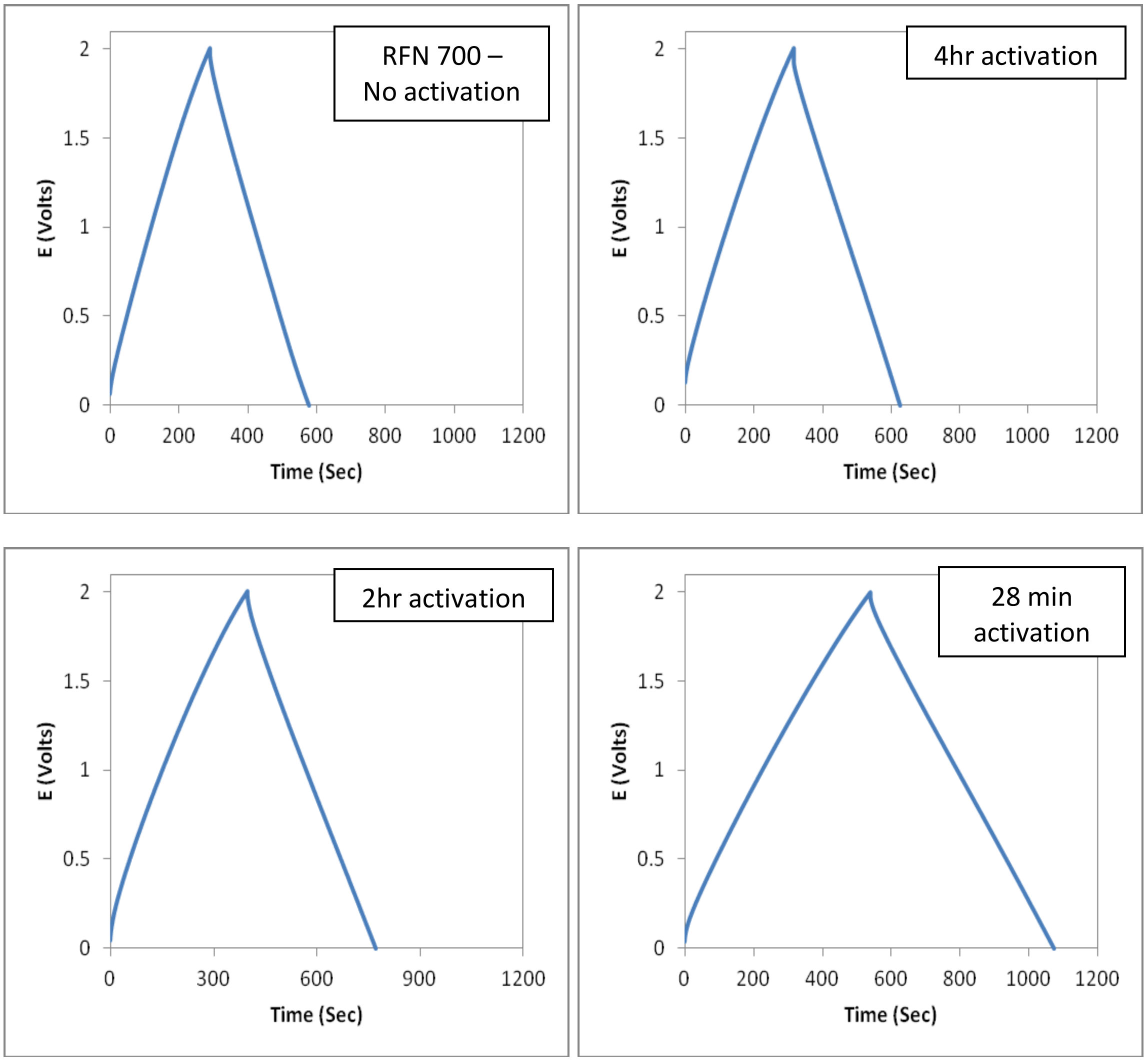

Figure 5.13. GCs taken at 0.5 mA for samples prepared from RFN 700 with different levels of activation.

Table 5.6. Level of activation of RFN 700 and the effect it has on mass loss and specific capacitance.

Activation Time	**Mass Loss**	**Specific Capacitance (F/g)**
No activation	-	52.1
4 hrs	85%	66.4
2 hrs	75%	79.9
28 min	53%	82.4

The Nyquist plots from EIS shown in Figure 5.14 help to illustrate how the sample with 28 minute activation has the highest capacitance. At low frequencies (Figure 5.14a), it can be seen that the sample with no activation has the highest diffusivity resistance. This is due to the limited surface area and pore volume in this sample, making the diffusion of the electrolyte ions into the material difficult. The three activated samples show similar values for diffusivity resistance, evidence that the activation process helps to reveal more micropores and open the porous structure, making more surface area accessible to the electrolyte ions. However, when the level of activation is too high, no new micropores are revealed and the average pore size begins to increase, decreasing surface area.[20] Additionally, high levels of activation can increase, as shown in Figure 5.14b. The sample activated for 4 hours has the highest charge transfer resistance, possibly due to more oxygen functionalities attaching to the surface during activation. The high capacitance for the sample activated for 28 minutes is thought to be due to the ideal level of activation, which results in increased surface are due to uncovered micropores with increased pore size, allowing better electrolyte penetration and easier diffusion. Also, more nitrogen can be retained at shorter activation times, increasing the capacitance due to additional pseudocapacitive reactions.

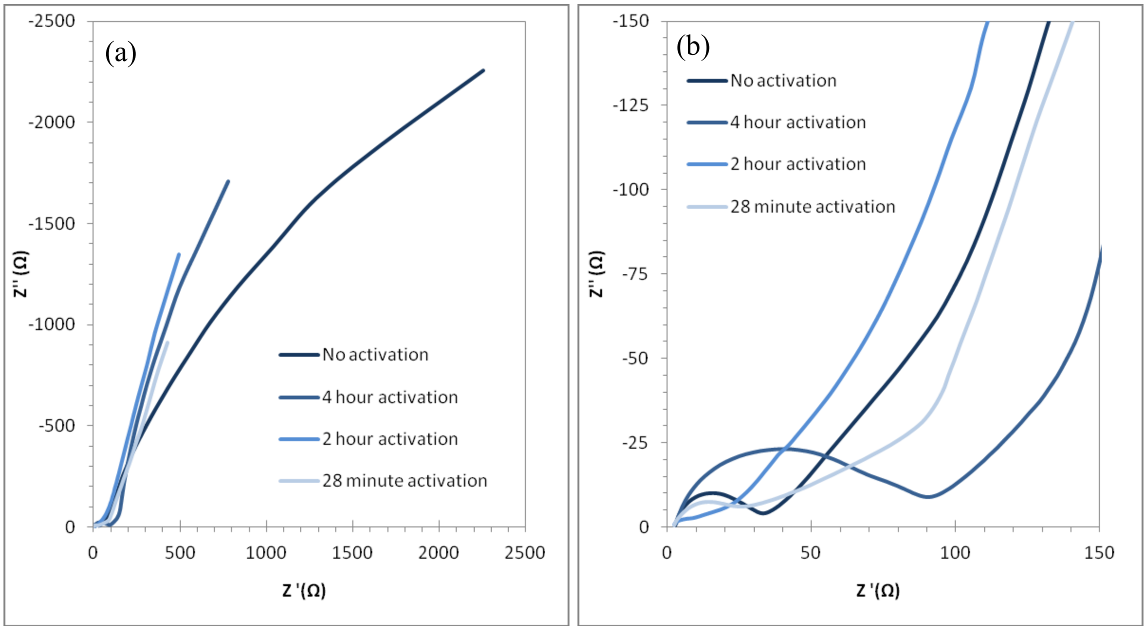

Figure 5.14. Nyquist plots at (a) high and low frequencies, and (b) high frequencies only. The sample with no activation shows the highest diffusivity resistance.

5.3. Hexamine solution modification after activation

5.3.1. Modification in hexamine solution with tert-butanol as the solvent

5.3.1.1. Synthesis

As mentioned above, a large specific surface area is very important to achieving a high capacitance due to an increase in active sites for double-layer formation and pseudocapacitive reactions. However, activation after nitrogen modification could result in a loss of nitrogen content. Therefore, resorcinol-furaldehyde carbon was also modified after activation using a simple solution method.

Resorcinol-furaldehyde gels were prepared using the same method as above. The resorcinol to furaldehyde molar ratio was again set to 0.5. The solid content was held at 25% in tert-butanol, and the resorcinol to hexamine molar ratio was either 50 or 75. After thoroughly mixing, the sol is placed in an oven at 80°C for 7 days for gelation and aging. The gels are freeze dried then pyrolyzed in N_2 at 900°C for 3 hours with a ramp rate of 5°C/min. Finally, the samples are activated in air at 420°C for 4 hours, then heated once again at 900°C in N_2 for 3 hours to remove any unwanted functional groups that arise during the activation process.

For nitrogen modification, hexamine is dissolved in tert-butanol. The weight percent of hexamine in solution was 2 wt%, 4 wt%, or 6 wt%. Large pieces of the activated carbon were placed in each hexamine solution and allowed to soak for approximately three days. The carbon was then removed from the solutions and freeze dried for several days. Devices were then prepared as described above, with nitrogen-modified carbon as the working electrode and unmodified activated carbon as the reference/counter electrode.

5.3.1.2. Composition and structure

From EDX results, it can be concluded that the modification step is successfully depositing nitrogen into the porous carbon, as shown in Table 5.7. While nitrogen is not detected in the unmodified carbon, which is likely the result of the high pyrolysis temperature and subsequent activation process, it is present in all three nitrogen modified carbon samples. With the lowest concentration of modification solution (2wt% hexamine in tert-butanol), approximately 4.0 at% is deposited. The amount of nitrogen in the porous carbon is increased to 5.7 at% by increasing the solution concentration to 4wt% hexamine in tert-butanol. However, with the highest concentration of hexamine in tert-butanol (6wt%), the amount of nitrogen deposited decreases slightly to 5.3 at%. At this concentration, hexamine may be precipitating, which might prevent it from getting into the smaller pores. Unfortunately, the sample with the highest nitrogen content also has the highest oxygen content. The additional oxygen can be detrimental for the cyclic stability of a supercapacitor device, as this impurity reacts irreversibly with the organic electrolyte. Ideally, the nitrogen content should be maximized while oxygen is minimized.

Table 5.7. Chemical composition in weight % and atomic % from EDX.

Sample	**Composition (Weight %)**			**Composition (Atomic %)**		
	Carbon	**Nitrogen**	**Oxygen**	**Carbon**	**Nitrogen**	**Oxygen**
Unmodified carbon	98.1	-	1.9	98.6	-	1.4
2wt% modification	94.1	4.6	1.2	95.1	4.0	0.9
4wt% modification	91.3	6.5	2.2	92.7	5.7	1.7
6wt% modification	93.1	6.1	0.8	94.1	5.3	0.6

SEM images of the unmodified carbon (25RC75) and 2wt% modified carbon are shown in Figure 5.15. The nitrogen coating does not seem to affect the nanotexture significantly. Both samples appear very similar, with small interconnected nanoparticles, creating a porous structure with high surface area.

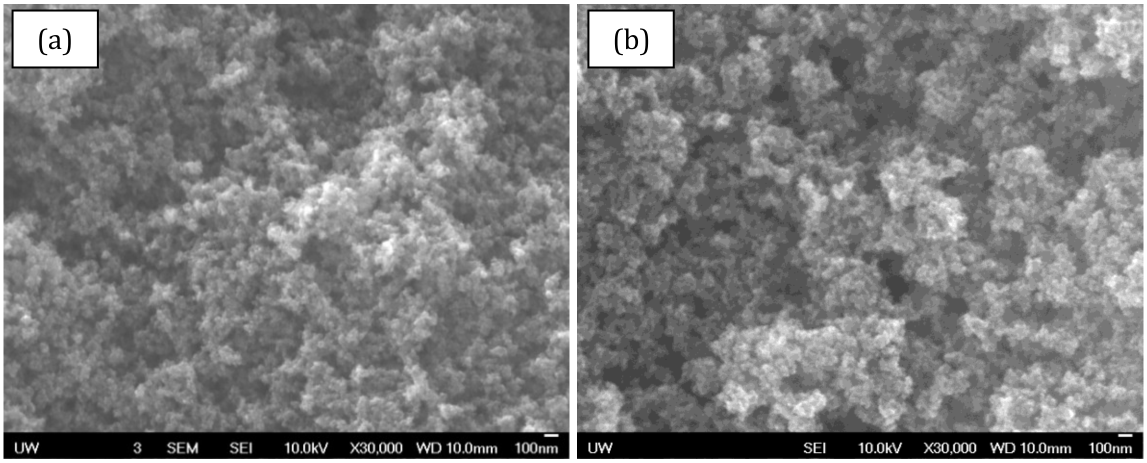

Figure 5.15. SEM images at 30,000x magnification comparing (a) unmodified carbon and (b) 2wt% modified carbon.

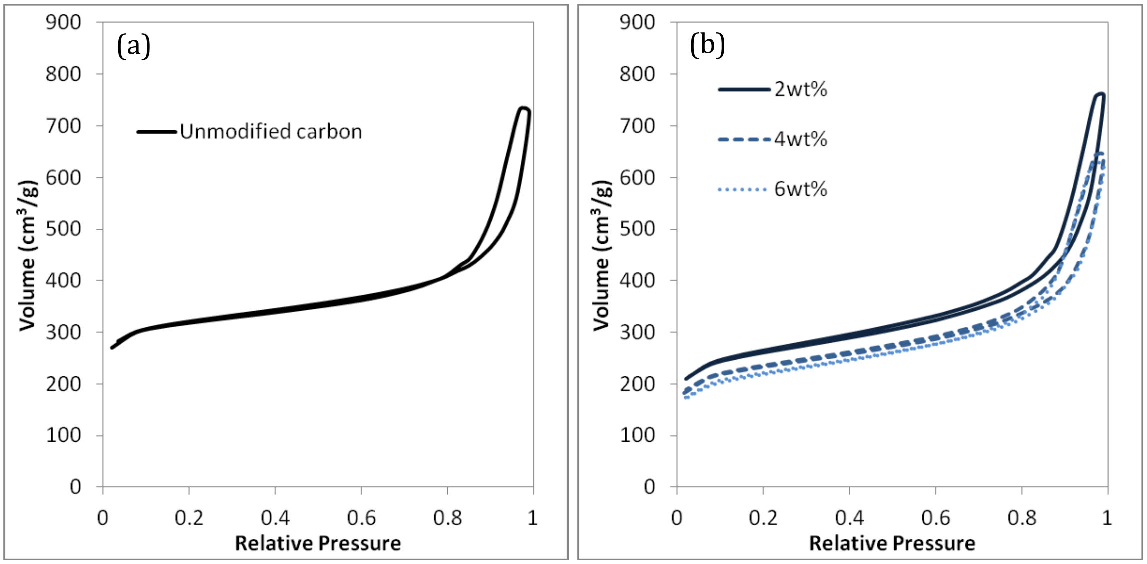

Figure 5.16. Nitrogen sorption isotherms for (a) unmodified carbon and (b) nitrogen modified carbon. There are fewer micropores for the nitrogen modified carbon, but more mesopores than unmodified carbon.

From nitrogen sorption analysis (Figure 5.16), it can be seen that the specific surface area decreases with increasing concentration of hexamine in solution, as listed in Table 5.8. The micropore surface area and pore volume also decrease with increasing concentration, suggesting that the hexamine is filling the micropores. The micropore size distributions in Figure 5.17 show the significant decrease in the pore volume after nitrogen modification. The average pore size remains approximately the same for all samples. Interestingly, there is not a similar trend for pores in the mesoporous region (2-50 nm in diameter). The mesopore surface area and actually increases for all of the nitrogen modified samples when compared to the unmodified carbon. The mesopore volume also increases for 2wt% and 4wt% nitrogen modification. This may be because the nitrogen is coating the surface of the macropores, decreasing the pore size into the mesoporous region. Figure 5.18 shows that the mesopore size distribution is narrowing slightly for the nitrogen modified carbon when compared to the unmodified carbon. The larger pores appear to disappear as the initial concentration of nitrogen increases, suggesting that nitrogen modification can be used to tune the pore structure of carbon.

Table 5.8. Surface areas, pore volumes, and pore diameters of unmodified carbon and carbon with 2 wt%, 4 wt%, and 6 wt% nitrogen modification based on nitrogen sorption analysis.

Sample	**Surface Area (m^2/g)**			**Pore Volume (cm^3/g)**		**Pore Diameter (nm)**	
	Total	**Mesopores**	**Micropores**	**Mesopores**	**Micropores**	**Mesopores**	**Micropores**
Carbon	949.0	152.0	701.2	0.672	0.390	3.2	1.4
2wt%	798.4	204.3	472.9	0.835	0.263	3.2	1.4
4wt%	714.8	175.3	432.8	0.687	0.238	3.2	1.4
6wt%	678.7	183.4	373.6	0.678	0.207	3.2	1.4

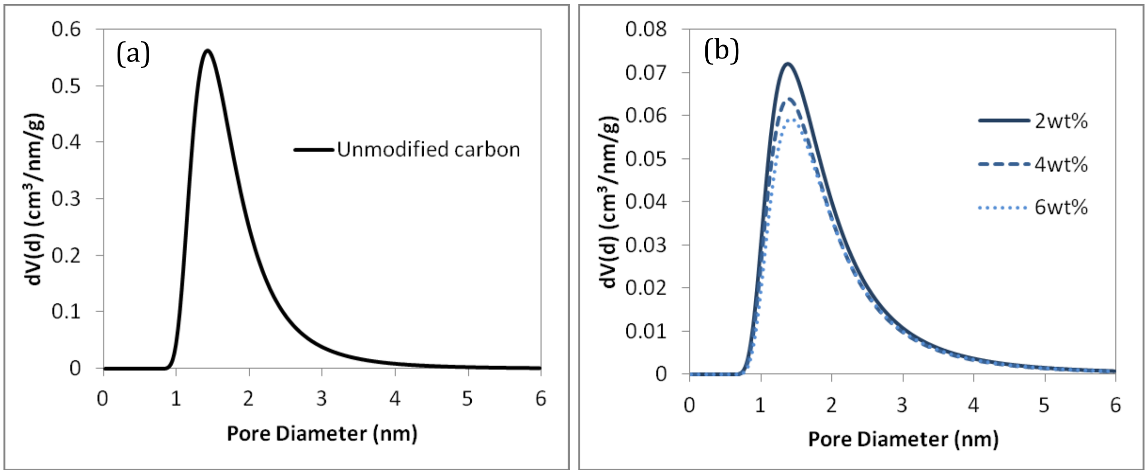

Figure 5.17. Micropore size distribution for (a) unmodified carbon and (b) nitrogen modified carbon. Nitrogen modification significantly decreases the total pore volume from micropores.

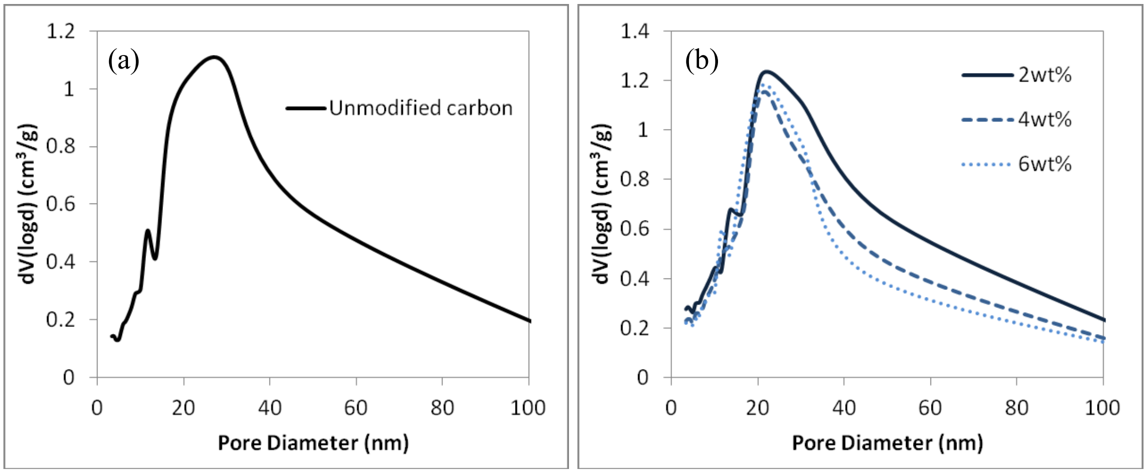

Figure 5.18. Mesopore size distribution for (a) unmodified carbon and (b) nitrogen modified carbon. Nitrogen modification slightly increases the mesopore volume and narrows the pore size distribution to smaller diameter pores.

FTIR spectroscopy provides insight into how the nitrogen is interacting with the carbon after modification. Spectra are shown in Figure 5.19 for 2wt%, 4wt%, and 6wt% hexamine modification. The nitrogen modified samples show the evolution of three small peaks that are not present in the unmodified sample, located at approximately 1230 cm^{-1}, 1000 cm^{-1}, and 665 cm^{-1}. Because of the multiple band overlaps in FTIR spectra, it is difficult to assign these peaks to one specific bond type. Each peak occurs in the fingerprint region, where a large number of adsorptions due to single bonds are present, including C-N and C-O. The peak at 1230 cm^{-1} may correspond to a C-O stretch from an alcohol, carboxylic acid, ester, or ether, or a C-N stretch due to aliphatic amines. The peak at 1000 cm^{-1} may also be due to the C-O bond stretching or a =C-H bond bending in an alkene. At 665 cm^{-1}, this peak may be due to an N-H bond found in primary and secondary amines.[128] The 4wt% modified sample shows the strongest peaks due to its high amount of both nitrogen and oxygen (Table 5.7).

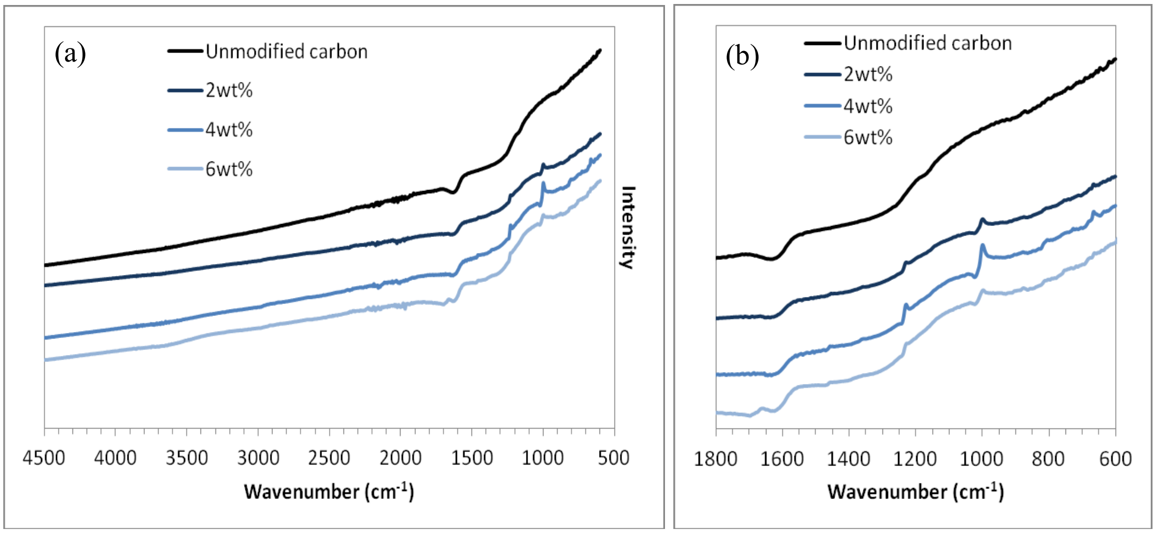

Figure 5.19. (a) FTIR spectra for unmodified carbon and nitrogen modified carbon and (b) enlarged view showing the evolution of peaks with higher nitrogen loading.

5.3.1.3. Electrochemical measurements

CVs taken at a scan rate of 10 mV/s for unmodified carbon, carbon with 2 wt% modification, carbon with 4 wt% modification, and carbon with 6 wt% modification are shown in Figure 5.20. The unmodified carbon shows a rectangular shape that is typical of electric double layer capacitors. When nitrogen is coated onto the surface of the porous carbon, the CV curve expands and distorts. The changes to the shape of the CV curves are indicative of other processes taking place besides double layer formation, such as pseudocapacitive reactions. This effect appears the most dramatic for the 2wt% and 6wt% samples, which both contain a fair amount of nitrogen. However, according to EDX, the 4wt% sample has the highest nitrogen content. This sample also exhibited the strongest peaks in FTIR, but the distortion of the CV curve is subtle. Galvanic cycling will show how these differences affect capacitance.

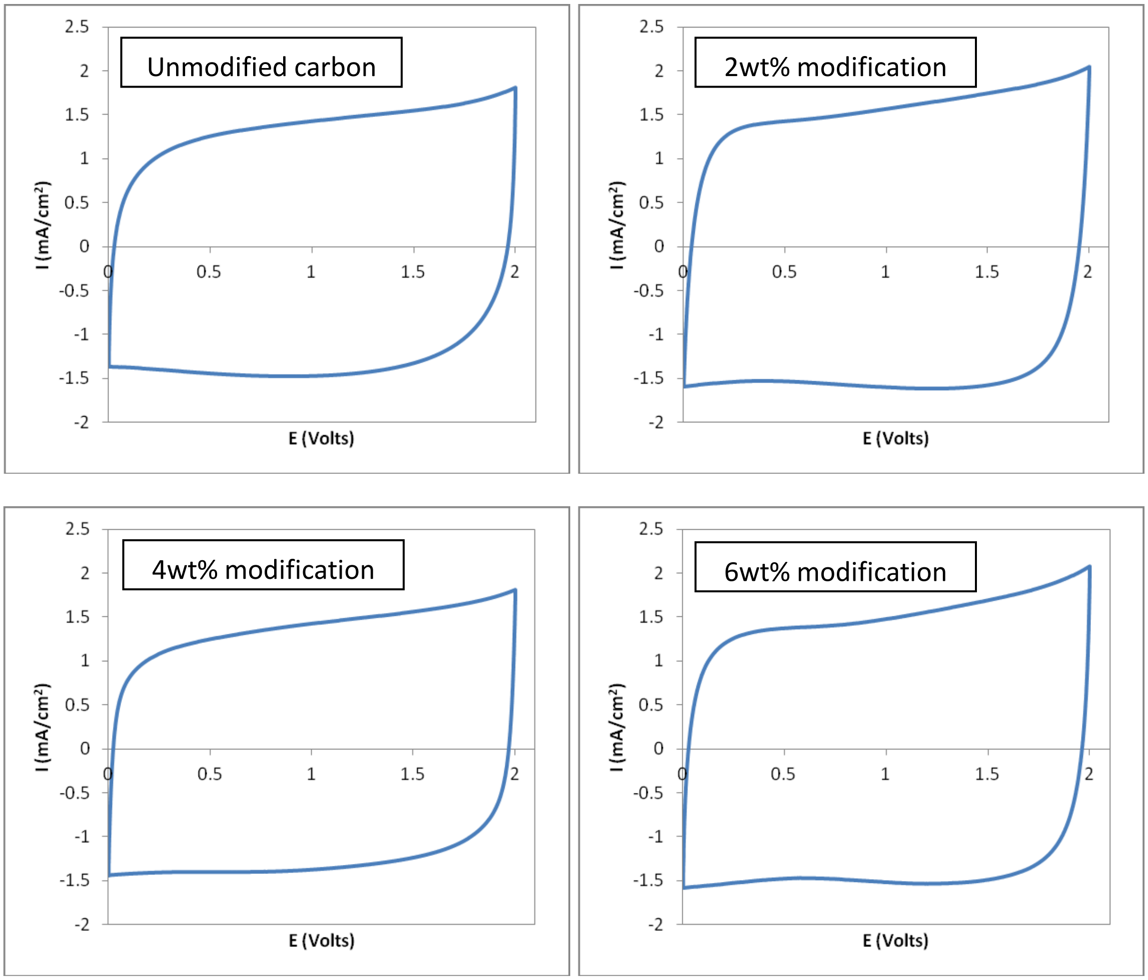

Figure 5.20. CV taken at 10 mV/s for unmodified carbon and nitrogen modified carbon.

The GC curves in Figure 5.21 show that all three nitrogen modified samples have nearly symmetric charging and discharging behavior, which is similar to the unmodified carbon. Additionally, each sample has a very limited voltage drop during discharge. This suggests that the nitrogen coating does not significantly increase resistance when cycled. The capacitance for each sample is listed in Table 5.9. The gravimetric capacitance of the 2wt% sample is slightly higher than that of unmodified carbon, but it is lower for the 4wt% and 6wt% samples. As seen previously, nitrogen increases the capacitance of porous carbon. However, the additional nitrogen in this case also increases the mass of the carbon. For the 2wt% sample, the amount of nitrogen coated on the pore surfaces is relatively low. Therefore, the sample mass is only slightly increased, so the charge storage added due to nitrogen pseudocapacitive reactions is noticeable in the value for gravimetric capacitance. However, in the case of the 4wt% and 6wt% samples, the added mass from the nitrogen overshadows the increased charge storage when capacitance is normalized to the sample mass. Therefore, it is also useful to examine the capacitance normalized to surface area and volume.

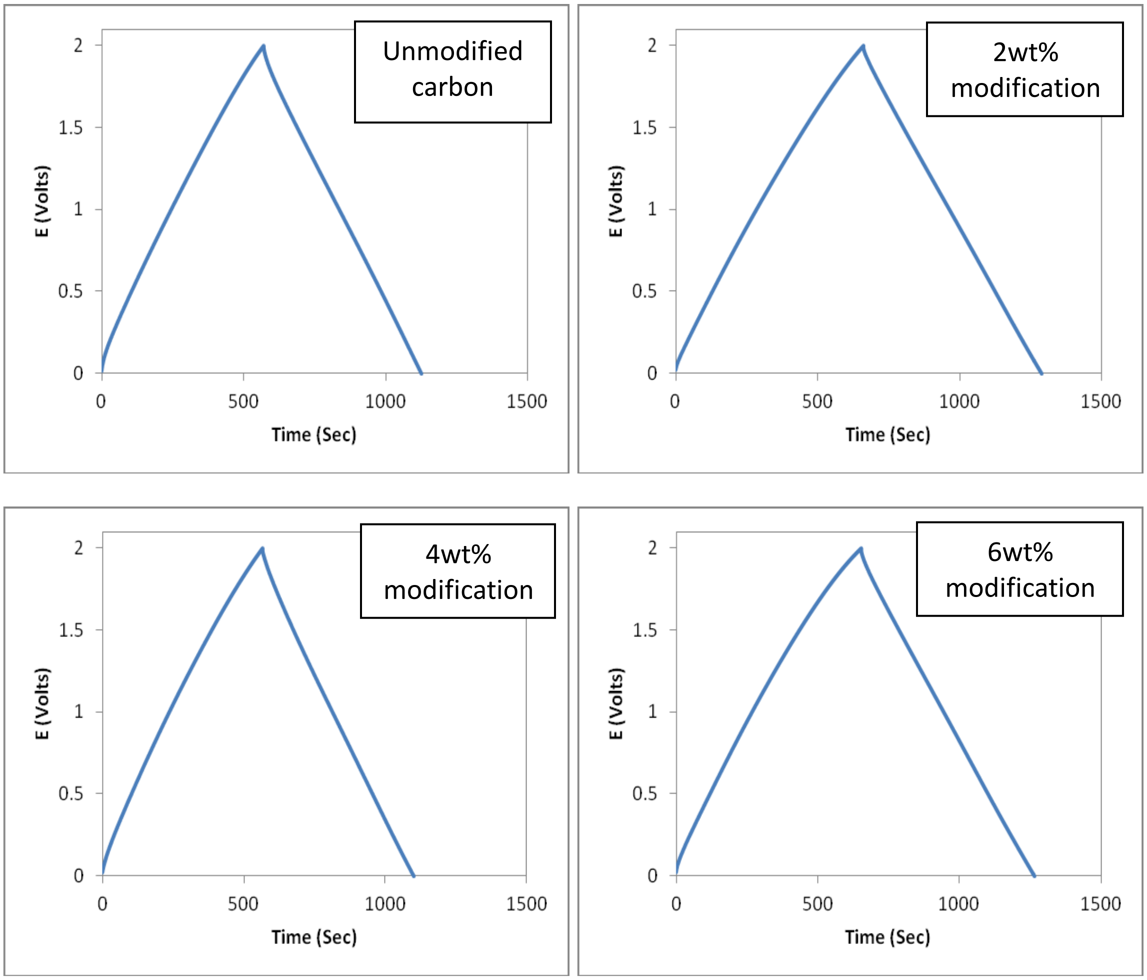

Figure 5.21. GCs taken at 0.5 mA for unmodified carbon and nitrogen modified carbon.

Table 5.9. Capacitance based on mass, total surface area, and volume for unmodified carbon and nitrogen modified carbon.

Sample	Specific Capacitance (F/g)	Capacitance Based on Total Surface Area (F/m^2)	Volumetric Capacitance (F/cm^3)
Unmodified carbon	94.7	**0.100**	41.9
2wt% modification	97.3	**0.108**	50.4
4wt% modification	80.4	**0.113**	40.3
6wt% modification	81.7	**0.120**	46.1

As seen from nitrogen sorption, coating with nitrogen decreases the total specific surface area depending on the amount of nitrogen added. When the capacitance is normalized to the surface area, the improved performance from the nitrogen coating can be seen.[129] All samples that were modified with nitrogen have higher capacitance than the unmodified carbon. Additionally, as the initial concentration of the nitrogen during modification increases from 2wt% to 6wt%, the capacitance normalized to specific surface area also increases. This improvement is due to contributions from pseudocapacitive reactions induced by nitrogen. While the decreased specific surface area decreases the capacitance contribution from double-layer formation, the addition of pseudocapacitance counteracts this loss. Volumetrically, the 2wt% sample has the highest capacitance. The 6wt% also shows an increase in capacitance when compared to unmodified carbon. Both of these samples showed the most distortion in their CV curves in Figure 5.20, suggesting that they have the largest contribution to overall performance from pseudocapacitance.

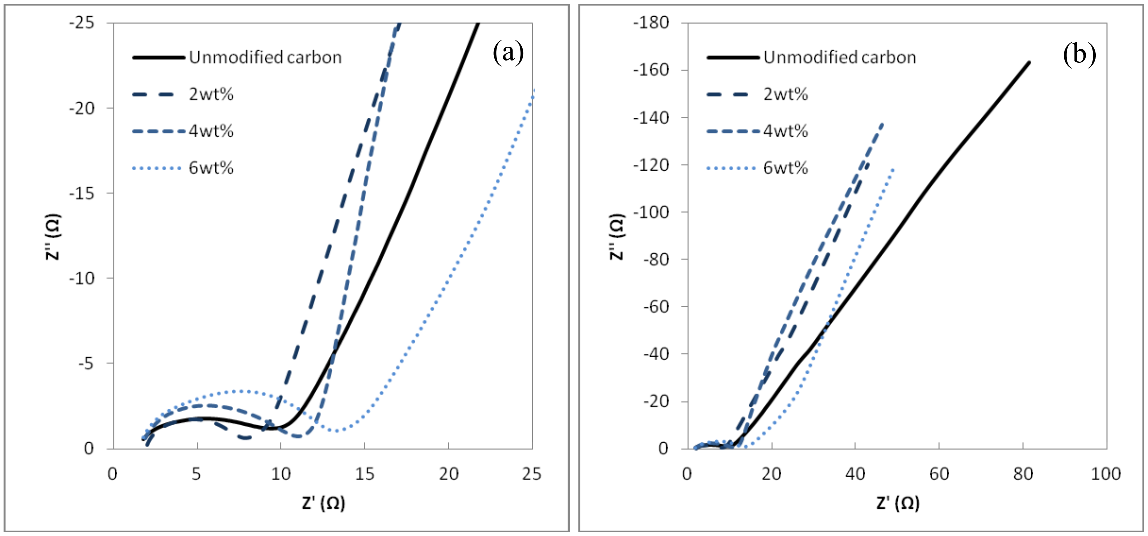

Figure 5.22. Nyquist plots for unmodified carbon and nitrogen modified carbon (a) at high frequency and (b) over the entire frequency range.

Table 5.10. Equivalent series resistance (ESR) and charge transfer resistance (R_{CT}) of unmodified carbon and nitrogen modified carbon.

	Carbon	**2wt%**	**4wt%**	**6wt%**
ESR (Ω)	1.80	2.03	1.90	1.77
R_{CT} (Ω)	7.66	5.84	9.14	11.4

Nyquist plots from EIS are shown in Figure 5.22 and corresponding values for equivalent series resistance (ESR) and charge transfer resistance (R_{CT}) are listed in Table 5.10. The ESR initially increases when nitrogen is coated on the porous carbon surface, but decreases with more nitrogen added. The 6wt% sample was synthesized with the highest concentration of nitrogen in solution, allowing more nitrogen to coat the carbon pore surfaces. This could lead to more conformal coverage of the nitrogen coating, decreasing the intrinsic resistance of the material. Figure 5.22a and Table 5.10 show how R_{CT} changes as the level of nitrogen modification changes. R_{CT} increases as nitrogen modification increases from 2wt% to 6wt%, which is due to a higher amount of pseudocapacitive reactions occurring due to more nitrogen. Interestingly, at the lowest level of nitrogen modification, R_{CT} is actually lower than unmodified carbon. The nitrogen coating may be improving the conductivity of the carbon surface, making it easier for the electrolyte ions to align at the electrode/electrolyte interface. Furthermore, it can be seen that nitrogen modification also works to decrease the diffusivity resistance of carbon, as indicated by the more vertical slope of the straight line at low frequency in Figure 5.22b. The nitrogen coating could be making the pore surface smoother, which would reduce scattering effects and allow the electrolyte to move in and out of the pores more freely. Increasing the pore volume is another possibility for the same reason. Additionally, increased surface area will increase the amount of active sites available for pseudocapacitive reactions.

5.3.2. Altering processing conditions

5.3.2.1. Synthesis

The EDX results shown in Table 5.7 indicate that the amount of nitrogen added to the carbon is relatively low and might not be high enough to cause a significant increase in the electrochemical performance of the supercapacitor. In order to increase the amount of nitrogen coating the pore surfaces, adjustments were made to the processing conditions. Carbon cryogels were synthesized using sol-gel processing with a solid content of 25% and a resorcinol to catalyst ratio of 75. After gelation and freeze drying, the carbon cryogels were pyrolyzed at 900°C under nitrogen flow and activated at 420°C for 4 hours under air flow. To surface modify carbon, solutions of 4wt% hexamine in tert-butanol were stirred and heated at 80°C for several days. Next, large pieces of the activated carbon cryogels were soaked at 80°C in the hexamine solutions three days. The modified samples were then freeze dried to remove any remaining solvent. Samples without further processing are labeled as NC-As-is. To see the effects of heat treatment on the nitrogen coated carbon, samples were also heated at 500°C for 3 hours under nitrogen flow after nitrogen modification. This sample is labeled as NC-Heated. Unmodified carbon is labeled as UC.

5.3.2.2. Structure and composition

Isotherms from nitrogen sorption are shown in Figure 5.23 and the corresponding surface area, pore volume, and pore size are listed in Table 5.11. With nitrogen modification, the surface area and pore volume decreases. Compared to the nitrogen modified carbon samples discussed in Section 5.2, the decrease in surface area and pore volume between UC and NC-As-is is much more significant. This suggests that much more nitrogen is coating the porous carbon. After heat treatment, the mesoporous surface area becomes larger than unmodified carbon. At the same time, the microporous surface area decreases. During heat treatment, the nitrogen coating may cause the micropores to grow into mesopores, accounting for the increased mesopore surface area.

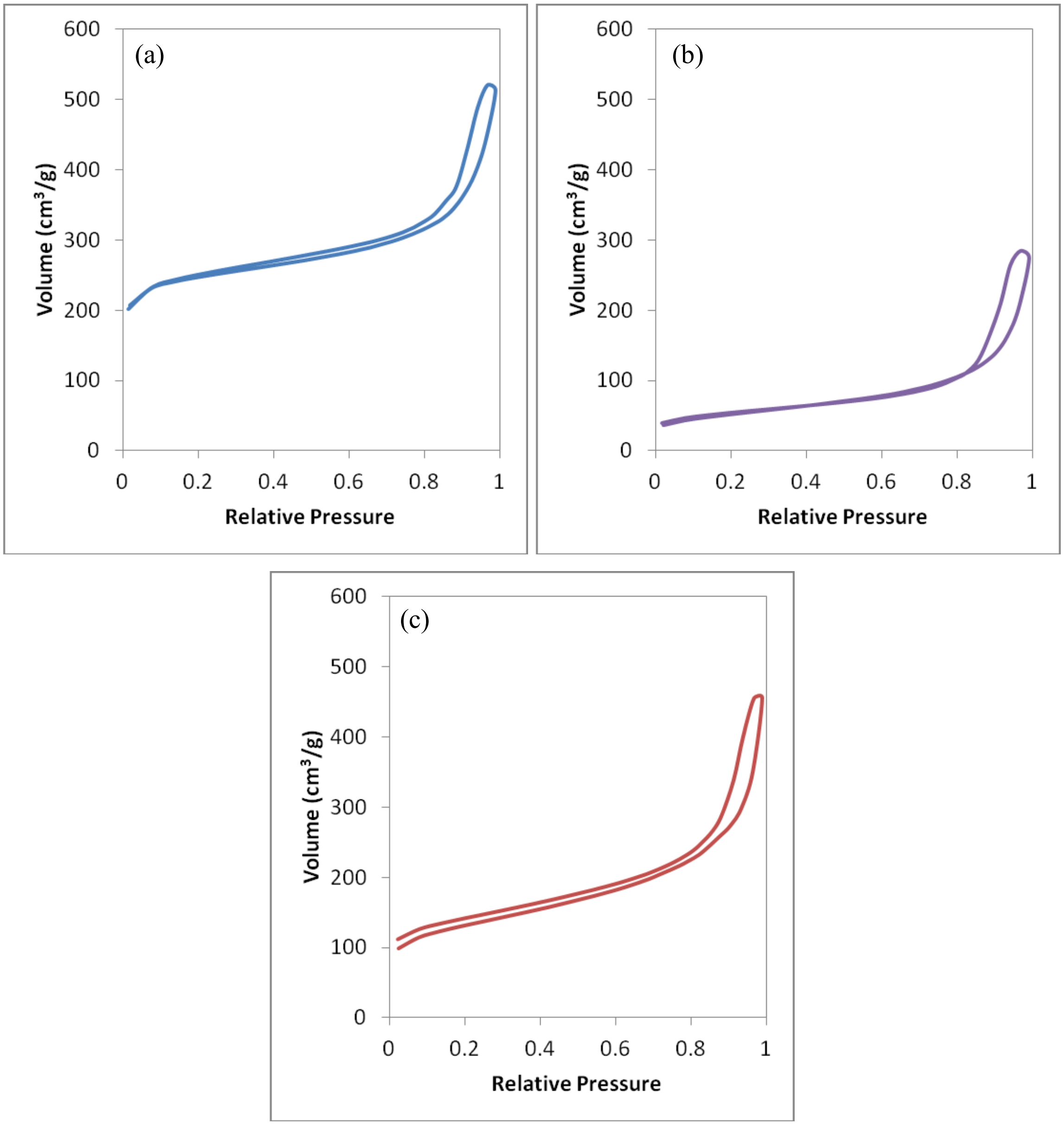

Figure 5.23. Nitrogen sorption isotherms for (a) UC, (b) NC-As-is, and (c) NC-Heated.

Table 5.11. Surface area, pore volume, and pore diameter from nitrogen sorption analysis.

Sample	**Surface Area (m^2/g)**			**Pore Volume (cm^3/g)**		**Pore Diameter (nm)**	
	Total	**Mesopores**	**Micropores**	**Mesopores**	**Micropores**	**Mesopores**	**Micropores**
UC	735.7	134.3	550.4	0.460	0.302	3.2	1.4
NC-As-is	172.4	96.35	346.1	0.394	0.020	3.7	1.6
NC-Heated	422.5	166.3	158.0	0.541	0.088	3.2	1.6

The mesopore size distributions in Figure 5.24 show how the mesopore volume changes after nitrogen modification. Without further heat treatment, nitrogen modified carbon has a slightly lower mesopore volume than unmodified carbon. However, after heating, the mesopore volume increases. Similarly, in the micropore region, the pore volume decreases significantly after nitrogen modification without further heat treatment, then increases again after heating. This suggests that the added nitrogen first fills the micropores, then causes the micropore volume to grow during heat treatment. These differences in pore structure between the three samples will have an effect on the electrochemical properties.

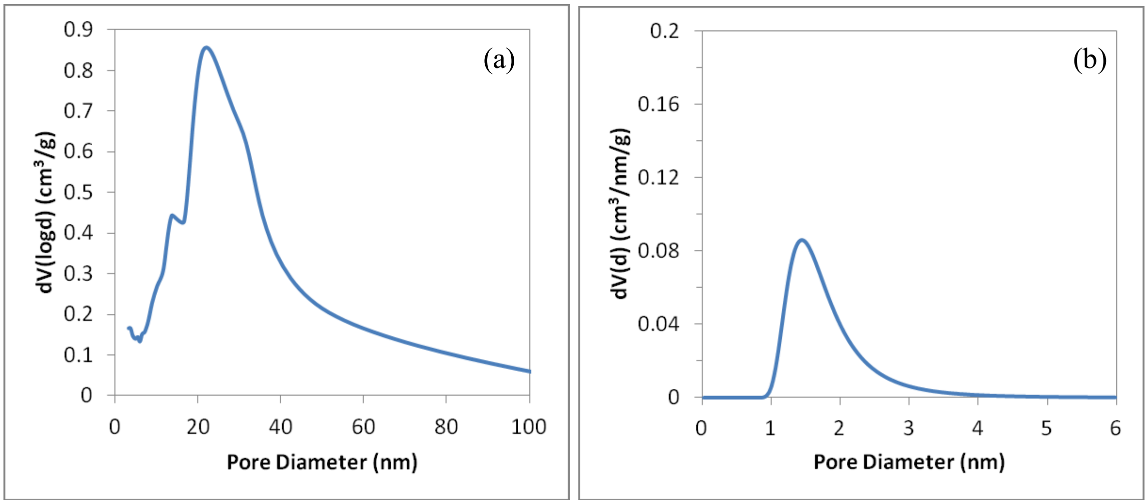

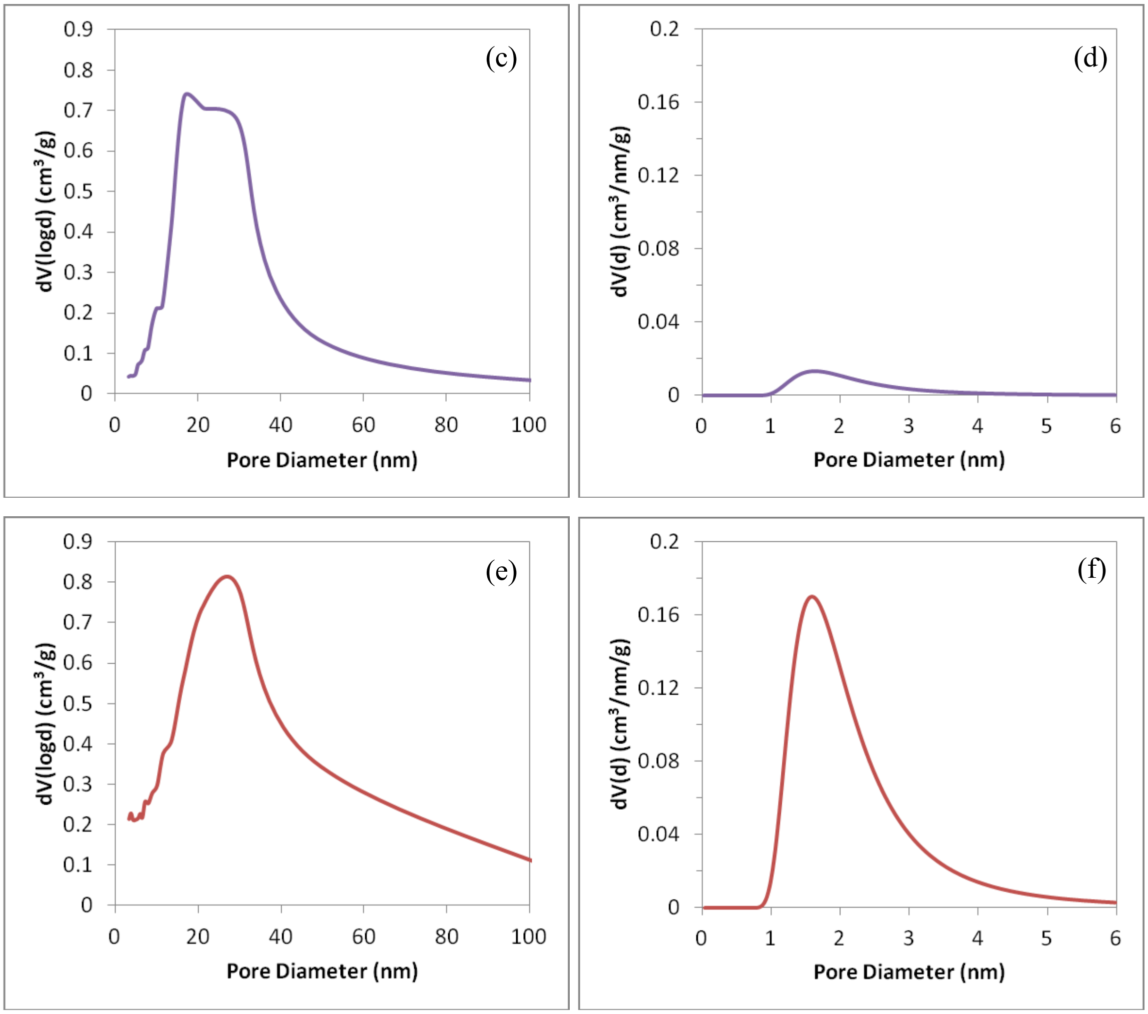

Figure 5.24. Mesopore (left) and micropore (right) size distributions for (a,b) UC, (c,d) NC-As-is, and (e,f) NC-Heated.

Table 5.12 lists the chemical compositions in weight % and atomic % for the three samples. Compared to the nitrogen modified samples in Section 5.3.1 (Table 5.7), NC-As-is and NC-Heated both show a higher nitrogen content. This indicates that the improved processing conditions helped to deposit more nitrogen onto the pore surfaces. NC-Heated has a larger amount of nitrogen than NC-As-is, which may be due to a more nitrogen depositing into this material during modification. Alternatively, as was seen in Section 5.2.4.2, adding a nitrogen coating changes the behavior of porous carbon when heated at high temperature. Therefore, the nitrogen coating in theses samples may cause the removal of some carbon, leading to the higher nitrogen content.

Table 5.12. Chemical compositions for UC, NC-As-is, and NC-Heated from EDX.

Sample	**Composition (Weight %)**			**Composition (Atomic %)**		
	Carbon	**Nitrogen**	**Oxygen**	**Carbon**	**Nitrogen**	**Oxygen**
UC	98.1	-	1.9	98.6	-	1.4
NC-As is	90.5	8.0	1.5	91.9	7.0	1.2
NC-Heated	89.0	9.8	1.2	90.5	8.6	0.9

To see how the nitrogen bonding structure may be affected by the heat treatment after modification, FTIR was performed on all three samples. Spectra are shown in Figure 5.25. As expected, more peaks were detected in NC-As-is when compared to UC. The most obvious ones occur at 1230 cm^{-1} and 1000 cm^{-1}, mirroring the findings in Section 5.3.1.2. The C-O bond stretch from an alcohol, carboxylic acid, ester, or ether may be responsible for these peaks. However, since UC has a higher oxygen content than NC-As-is, these peaks should also be present in its spectrum. Their absence suggests that they are due to C-N and C-H bonds instead. The peak at 1230 cm^{-1} therefore likely corresponds to the C-N stretch due to aliphatic amines and the peak at 1000 cm^{-1} may be due to =C-H bond bending in alkenes. For NC-Heated, the peaks disappear and the spectrum more closely resembles that of UC. This suggests that the nitrogen coating is undergoing a chemical change when heat treated, causing C-N bonds to transform into something else. However, no new peaks appear at different wavenumbers, so another technique, such as XPS, is necessary to determine what may be happening in this sample.

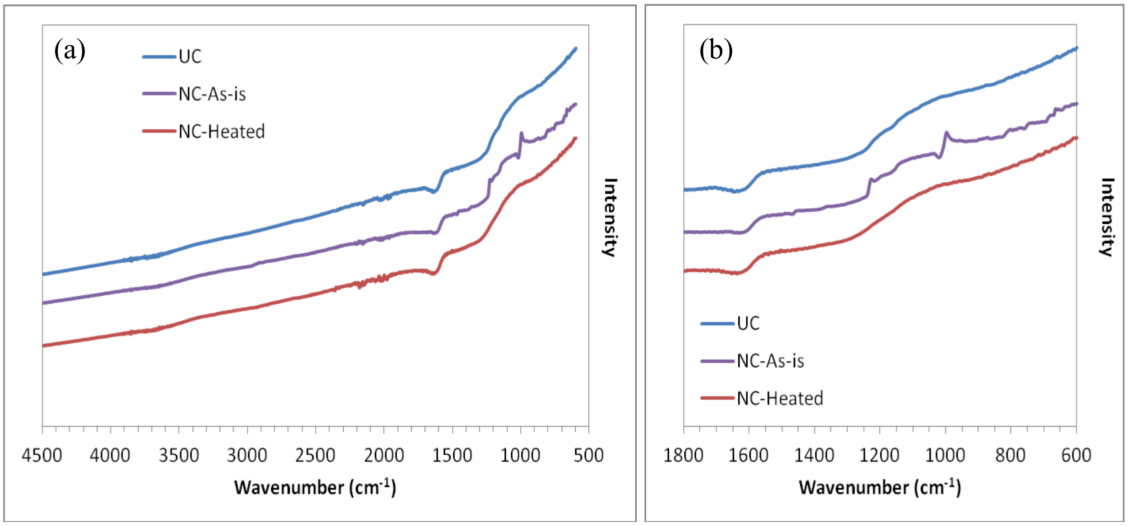

Figure 5.25. (a) FTIR spectra for unmodified carbon and nitrogen modified carbon with and without heat treatment, and (b) enlarged view showing the evolution of peaks for nitrogen modified carbon, but their disappearance following heat treatment at 500°C.

Survey spectra from XPS are shown in Figure 5.26 and detailed scans for the O 1s peak and N 1s peak are shown in Figure 5.27. In the survey scans, UC shows peaks for only carbon and oxygen, as well as a small peak for fluorine from the PTFE binder used to prepare samples. The nitrogen modified carbon samples also show carbon and oxygen peaks, in addition to nitrogen peaks. From the detailed scans, it can be seen that the heat treatment after nitrogen modification dramatically changes the bonding characteristics in the material. The most significant difference can be found in the N 1s peak position. UC and NC-As-is show a single peak, while NC-Heated shows two distinct peaks. For UC and NC-As-is, the peak at 399.5 eV may correspond to an amine group.[130] However, for NC-Heated, the peak at 400.5 eV may correspond to a cyanide group, while the peak at 398.5 eV may correspond to a heterocyclic group. This dramatic difference in the bonding of nitrogen will be shown to have a significant impact on the electrochemical behavior of the material.

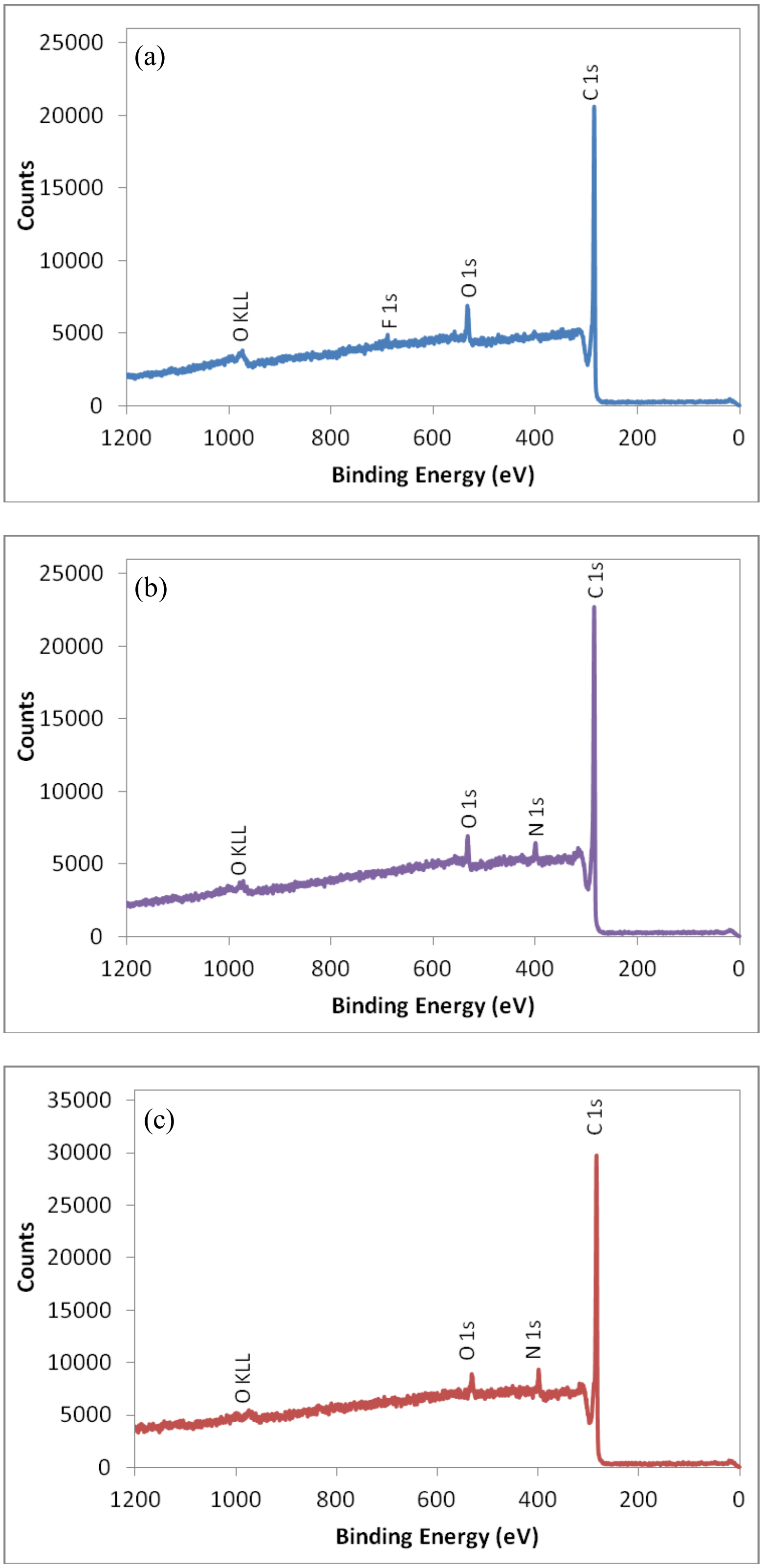

Figure 5.26. XPS survey scans for (a) UC, (b) NC-As-is, and (c) NC-Heated.

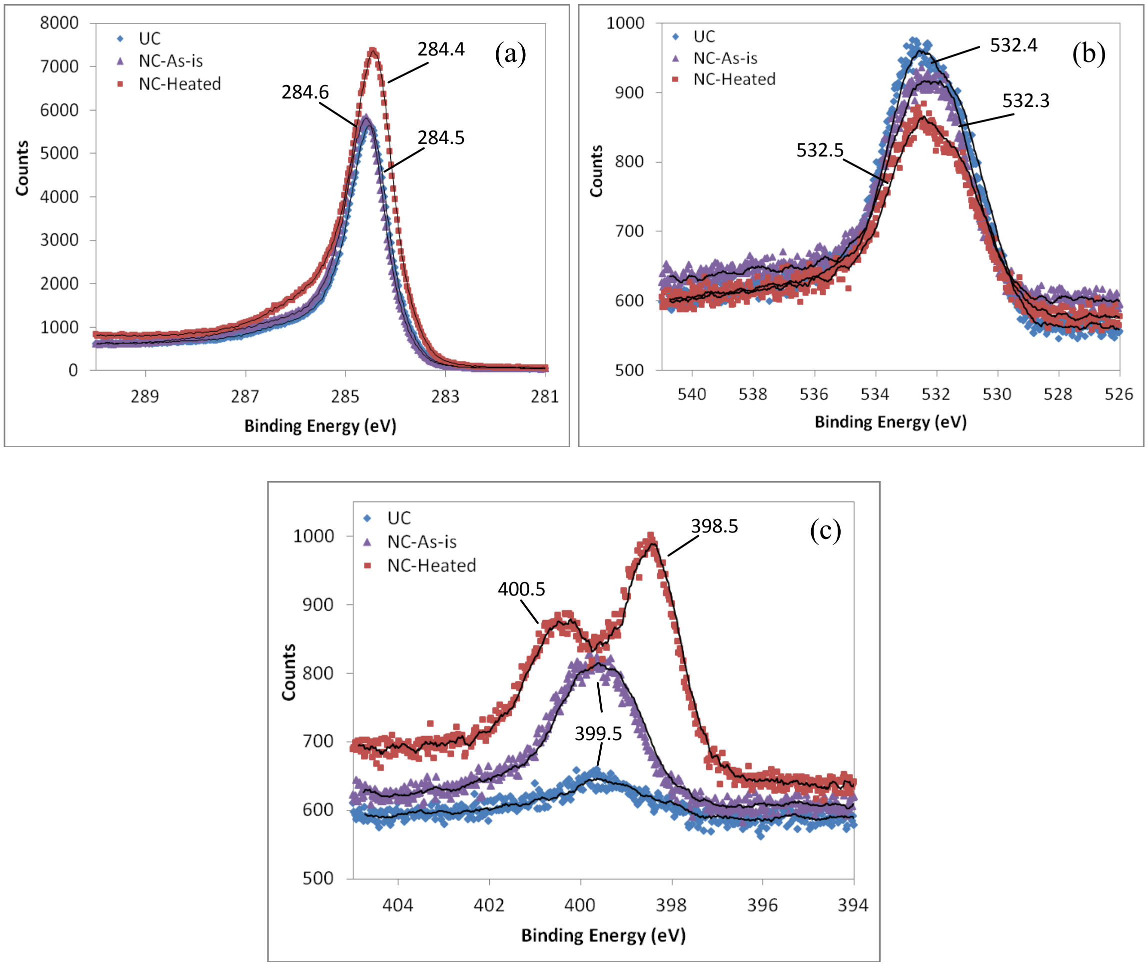

Figure 5.27. Detailed scans for the (a) C 1s peak, (b) O 1s peak, and (c) N 1s peak.

5.3.2.3. Electrochemical analysis

Cyclic voltammograms taken at 10 mV/s and galvanic cycling curves taken at 0.5 mA for each sample are shown in Figure 5.28. Compared to unmodified carbon, there is some distortion in the CV curves for nitrogen modified carbon both before and after heat treatment. NC-As-is exhibits some small peaks as charging approaches 2V and discharging approaches 0V. The measured current is also higher for this sample than UC, suggesting higher capacitance. Due to the much lower surface area for NC-As-is as compared to UC, it can be assumed that the enhanced performance is from pseudocapacitive reactions induced by the nitrogen coating. For the NC-Heated CV, the measured current is much lower than NC-As-is. Surprisingly, it is also slightly lower than the measured current for UC. A small peak still occurs as the voltage approaches 2V, suggesting that some pseudocapacitive reactions are still present. From the GC curves, all samples show minimal voltage drops at the onset of discharge. At 0.0065 Volts, NC-As-is has the smallest voltage drop, followed by UC at 0.0075 Volts and finally NC-Heated at 0.0087 Volts. However, the differences in discharge time are much more significant. Mirroring the findings from the CV curves, NC-As-is shows the best performance as evidenced by the longer discharge time, while NC-Heated has the lowest performance.

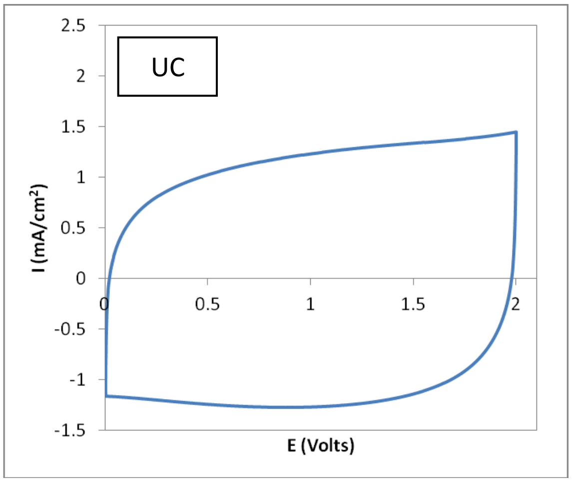

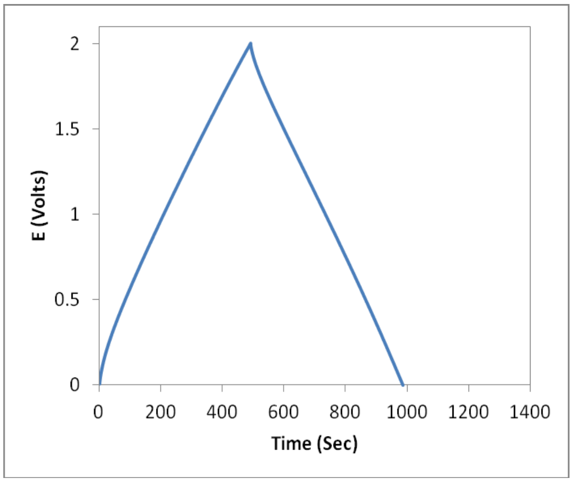

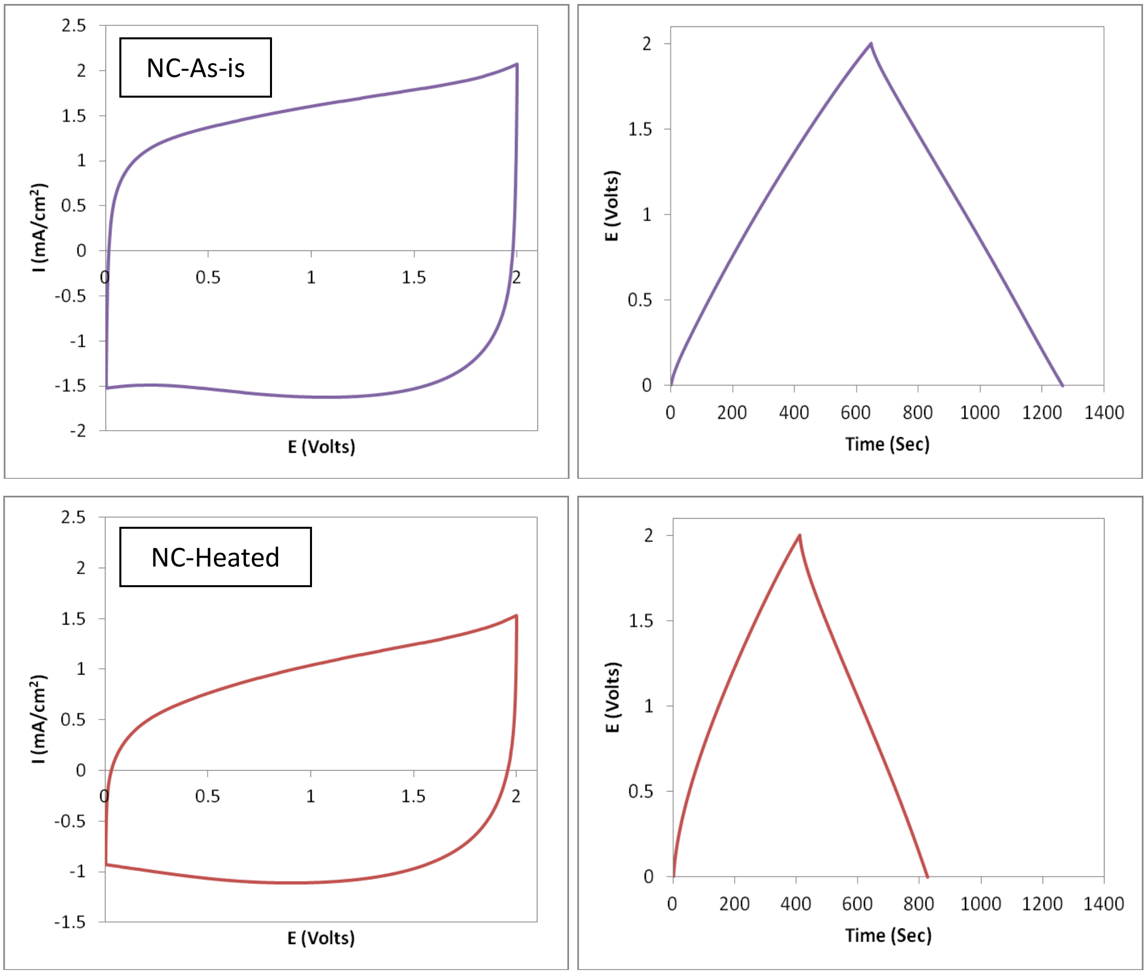

Figure 5.28. Cyclic voltammograms taken at 10 mV/s and galvanic cycles taken at 0.5 mA for UC, NC-As is, and NC-Heated.

Table 5.13. Capacitance normalized to mass, total surface area, and volume.

Sample	**Gravimetric Capacitance (F/g)**	**Capacitance Based on Total Surface Area (F/m^2)**	**Volumetric Capacitance (F/cm^3)**
UC	80.2	0.109	42.5
NC-As-is	87.8	0.509	49.8
NC-Heated	64.7	0.153	35.7

Values for capacitance normalized to mass, total surface area, and volume are listed in Table 5.13. The gravimetric capacitance is highest for NC-As-is, increasing by almost 10% when compared to UC despite the added mass from the nitrogen coating. Similarly, the volumetric capacitance is highest for NC-As-is. When the capacitance is normalized to total surface area, the effect of the nitrogen coating is even more prominent. The capacitance is nearly 5 times higher for NC-As-is than UC, a result of the improved processing conditions during the initial nitrogen modification step. However, heating after nitrogen modification is detrimental to charge storage as evidenced by the significantly decreased capacitance for NC-Heated.

From the Nyquist plots shown in Figure 5.29, it can be seen that the diffusivity resistance decreases for the carbon after nitrogen modification but without further treatment. The nitrogen coating may be smoothing the carbon pore surfaces, decreasing scattering effects and making it easier for the electrolyte ions to move in and out of the pores. However, after heat treatment of the nitrogen modified carbon, the diffusivity resistance increases and surpasses that of unmodified carbon. Table 5.14 shows that the ESR increases slightly for carbon after nitrogen modification, but there is very little difference before and after heat treatment. However, a difference can be seen for the R_{CT}, increasing by almost 50% after heat treatment. Since the starting nitrogen concentration is not higher for this sample, it can be assumed that this difference is due to the nitrogen coating structure changing after heating at 500°C. This alteration is non-ideal for supercapacitors, resulting in decreased performance. Interestingly, R_{CT} is lower for NC-As-is than for UC. This suggests that the nitrogen coating facilitates better charge transfer at the electrode/electrolyte interface, helping to significantly improve performance of this material for supercapacitors.

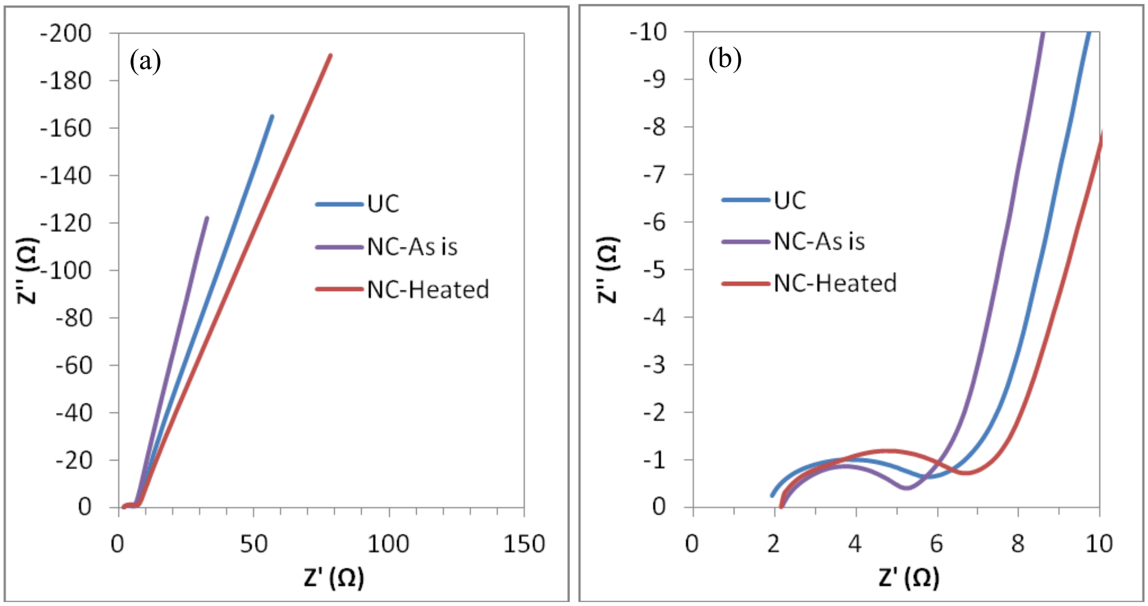

Figure 5.29. Nyquist plots (a) over the entire frequency range and (b) at high frequency only.

Table 5.14. Equivalent series resistance (ESR) and charge transfer resistance (R_{CT}) for unmodified carbon and nitrogen modified carbon both before and after heat treatment.

Sample	ESR (Ω)	R_{CT} (Ω)
UC	1.92	3.79
NC-As-is	2.18	3.06
NC-Heated	2.16	4.47

To test the effect of lower R_{CT}, the samples were cycled at higher applied currents during galvanic cycling. With a low R_{CT}, the samples will be able to react to the changing charge and discharge current faster, resulting in higher capacitance. Figure 5.30 shows how the gravimetric capacitance varies with applied current for all three samples. At the lowest applied current of 0.5 mA, the gravimetric capacitance for NC-As-is is almost 10% higher than that for UC. At a higher applied current of 10 mA, NC-As-is has a capacitance that is over 35% higher than UC. These results suggest that careful coating of carbon with nitrogen is very beneficial for enhancing the performance of supercapacitors, especially those subjected to high charge and discharge rates.

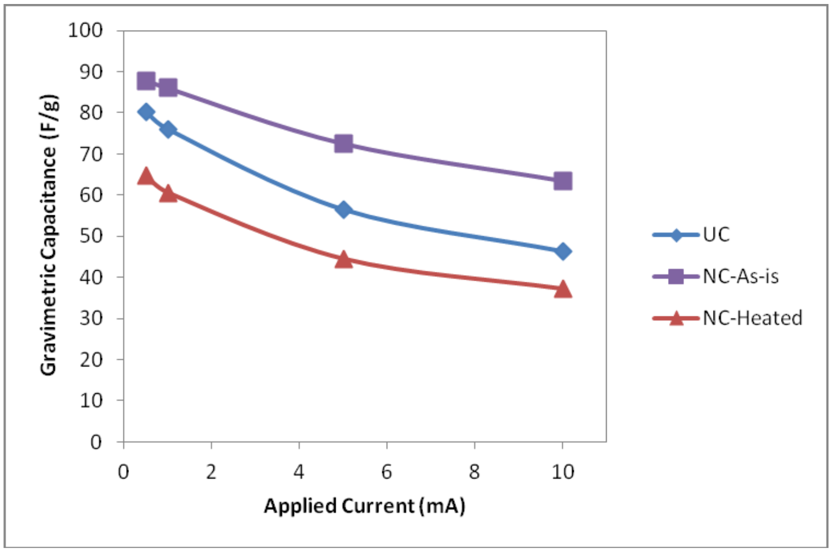

Figure 5.30. Gravimetric capacitance at various applied currents for unmodified carbon and nitrogen modified carbon before and after heating at 500°C. Carbon surface modified with nitrogen without further heat treatment consistantly shows the highest capacitance, especially at high applied currents.

5.4. Summary

Nitrogen can be added to porous carbon, either in the bulk as heteroatoms or on the pore surfaces as a coating, in order to induce pseudocapacitive reactions that add capacitance that is already present due to electric double layer formation. Contact angle measurements show that the wettability is changes with the addition of nitrogen, especially when it is coated on the surface of the pores. The activation behavior also changes significantly. Compared to unmodified carbon, nitrogen modified carbon has a higher capacitance, with surface nitrogen having more of an effect on capacitance than nitrogen in the bulk network. Coating with nitrogen increases the mass of carbon electrodes, so adding a large amount can decrease the gravimetric capacitance. However, when the capacitance is normalized to total surface area, the significant improvement from the nitrogen coating can be seen. Heating nitrogen modified carbon can change the type of nitrogen bonding, which may be less favorable to inducing pseudocapacitance.

6. *Increasing the working voltage for improved energy and power density*

6.1. Introduction

In organic electrolyte, the voltage window is often limited to 2V. Devices are rarely tested at increased working voltages because as the voltage approaches 3V, organic electrolytes can breakdown due to reactions with oxygen and other unwanted impurities in the porous carbon electrodes.[67, 131] However, synthesis of a highly pure carbon can prevent such reactions from occurring. Additionally, a nitrogen coating on the surface may create a barrier between the impurities and the electrolyte ions. In both scenarios, the voltage could be pushed higher. This will increase the energy density of the supercapacitor significantly according to Equation 3,

$$E = \frac{1}{2}CV^2 \qquad (3)$$

where E is the energy density, C is the capacitance, and V is the applied voltage. Since voltage is squared, increasing it will have a much greater effect on the energy density than increasing the capacitance. A higher voltage will also have an effect on the power density, given Equation (4),

$$P = \frac{V^2}{4R_S m} \qquad (4)$$

where R_s is the equivalent series resistance (ESR) and m is the mass of the electrodes. Like energy density, the power density depends on the square of voltage, so a higher working voltage will significantly increase this value.

The typical working voltage for activated carbon in organic electrolyte is 2V. To test the performance of the unmodified resorcinol-furaldehyde carbon and nitrogen-modified resorcinol-furaldehyde carbon, samples were tested at several working voltages, specifically 2V, 2.5V, and 3V. Each sample was tested at only one working voltage. CVs (100, 50, and 10 mV/s), GCs (100, 50, 10, 5, 1, and 0.5 mA), and EIS (10 mV, 0.1 MHz to 1 mHz) were performed at the specified voltage for each sample.

Higher working voltages are known to decrease device lifetime and durability when compared to normal working voltages. This is due to the higher voltage amplifying the effects of electrolyte degradation due to impurities and mechanical breakdown from the electrode swelling during charge and discharge.[67] In order to test the impact of higher working voltages on the various samples, cyclic stability tests were performed. After completing the CVs and GCs at different rates and EIS as mentioned above, samples were subjected to repeated charge and discharge to their specified voltage at a rate of 1 mA up to 200 cycles. Capacitances were calculated from the discharge slopes every 10 cycles.

6.2. Synthesis

Both unmodified carbon and nitrogen-modified carbon were tested at higher working voltages. The unmodified resorcinol-furaldehyde carbon had a 25% solid content and a resorcinol to hexamine mass ratio of 75. The samples were pyrolyzed at 900°C and activated in air at 420°C for 4 hours. These samples are referred to as unmodified carbon. The nitrogen-modified carbon was prepared the same way as the unmodified carbon and was soaked in a heated solution of 4 wt% hexamine in tert-butanol for several days then dried. These samples are referred to as 4 wt% modified carbon. Devices for nitrogen-modified carbon were prepared with activated unmodified carbon as the counter/reference electrode.

6.3. Electrochemical analysis

6.3.1. Unmodified carbon tested at higher working voltages

For unmodified carbon, the rectangular shape of the CV curves characteristic of double-layer formation are retained as the working voltage is increased from 2V to 3V, as can be seen in Figure 6.1. For the samples tested at 2.5V and 3V, a slight peak appears when approaching the maximum voltage, which may suggest some redox reactions are taking place at high voltage from either residual oxygen or nitrogen in the bulk carbon network. The measured current also increases as the working voltage increases, particularly at 3V, suggesting more charge storage.

The GC curves at each working voltage show symmetric charging and discharging behavior, which is another indication of double-layer formation. Each sample also has a minimal voltage drop as discharging begins, signifying that there is only a small amount of resistance present. The capacitance calculated from these curves is listed in Table 6.1. Both the gravimetric capacitance and the capacitance normalized to total surface area increase as the working voltage increases. The sample tested at 3V has the highest capacitance, increasing by approximately 15% over the sample tested at 2V. This increase in capacitance at higher voltages has been observed in other systems, and is believed to be due to electrochemical doping.[67, 132]

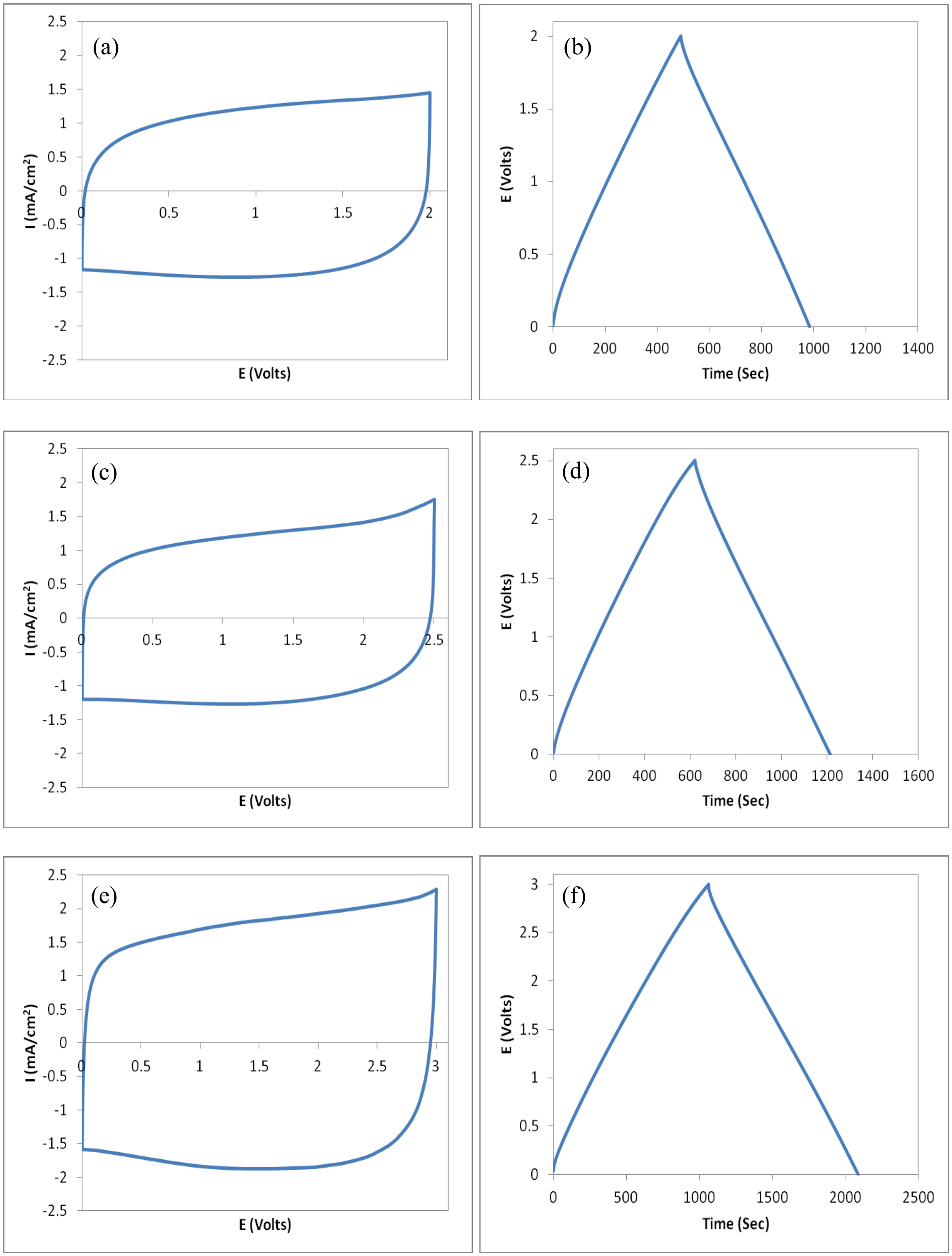

Figure 6.1. CVs taken at 10 mV/s (left) and GCs taken at 0.5 mA (right) for unmodified carbon tested at working voltages of (a, b) 2V, (c, d) 2.5V, and (e, f) 3V.

Table 6.1. Capacitance normalized to mass and surface area for unmodified carbon tested at high working voltages.

Working voltage	Gravimetric Capacitance (F/g)	Capacitance Based on Total Surface Area (F/m^2)
2V	80.2	0.109
2.5V	85.5	0.116
3V	92.2	0.125

According to Equations 3 and 4, both the energy density and power density are dependent on the voltage squared. Table 6.2 shows how the energy density and power density change with increasing working voltage for the unmodified carbon. The energy density increases significantly as the working voltage increases, more than doubling when comparing the samples tested at 2V and 3V. The large increase in the energy density is particularly significant because supercapacitors are notorious for having small energy densities (<10 Wh/kg) when compared to batteries (>100 Wh/kg).[12, 67] The power density also increases when the working voltage increases from 2V to 2.5V, but unlike the energy density, it decreases when the working voltage increases from 2.5V to 3V. EIS shows that the equivalent series resistance and charge transfer resistance increase at higher working voltages, as shown in Table 6.2 and Figure 6.2. However, the power density is 50% higher for the sample tested at 3V when compared to the sample tested at 2V. The superior performance of this material can be attributed to its high purity. Common sol-gel synthesis processes use catalysts that contain metal ions, such as NaOH, which can leave behind sodium and oxygen impurities in the bulk carbon network. However, the process used here replaces the metal ion catalyst with hexamine, contributing only nitrogen as an impurity.

Table 6.2. Energy density, power density, equivalent series resistance (ESR), and charge transfer resistance (R_{CT}) for unmodified carbon tested at higher working voltages.

Working Voltage	Energy Density (Wh/kg)	Energy Density (Wh/km^2)	Power Density (W/kg)	Power Density (W/km^2)	ESR (Ω)	R_{CT} (Ω)
2V	44.9	61.0	164	222	1.92	3.79
2.5V	74.4	101	283	385	2.04	4.19
3V	115	157	305	414	2.43	12.6

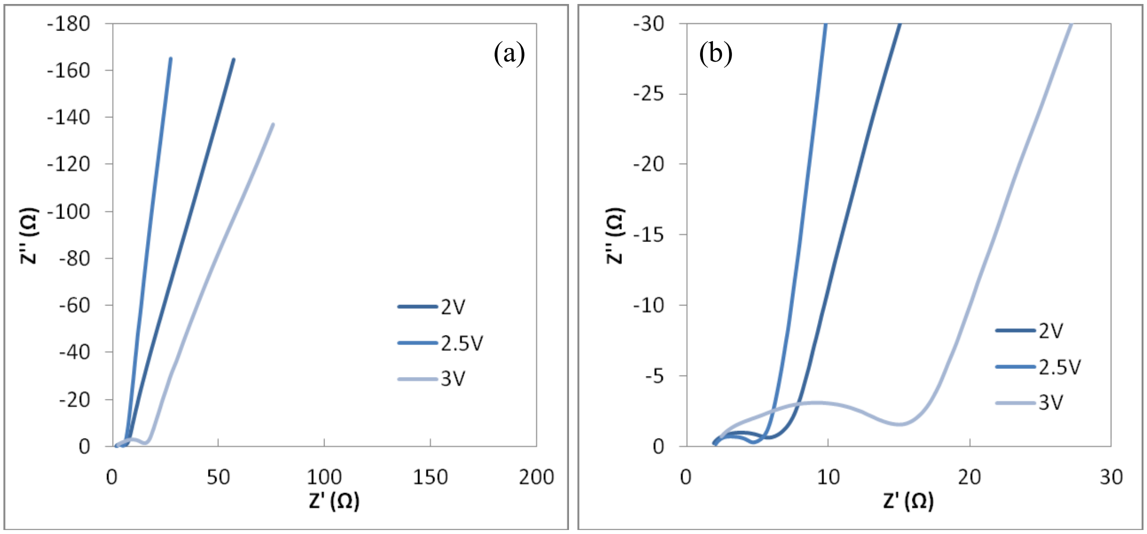

Figure 6.2. Nyquist plots for unmodified carbon (a) over the entire frequency range and (b) at high frequency only. Diffusivity resistance, equivalent series resistance, and charge transfer resistance increase as the working voltage increases.

6.3.2. Nitrogen-modified carbon tested at higher working voltages

The nitrogen-modified carbon showed a similar trend to the unmodified carbon, as evidenced by the CV and GC curves shown in Figure 6.3. The 4 wt% modified sample tested at 2V and 2.5V shows a fairly rectangular shape. As the working voltage increases to 3V, the sample shows more resistance, somewhat resembling what researchers refer to as a leaf-shaped curve. The GC curve for the sample tested at 3V also demonstrates increased resistance, as evidenced by the largest voltage drop of all three samples.

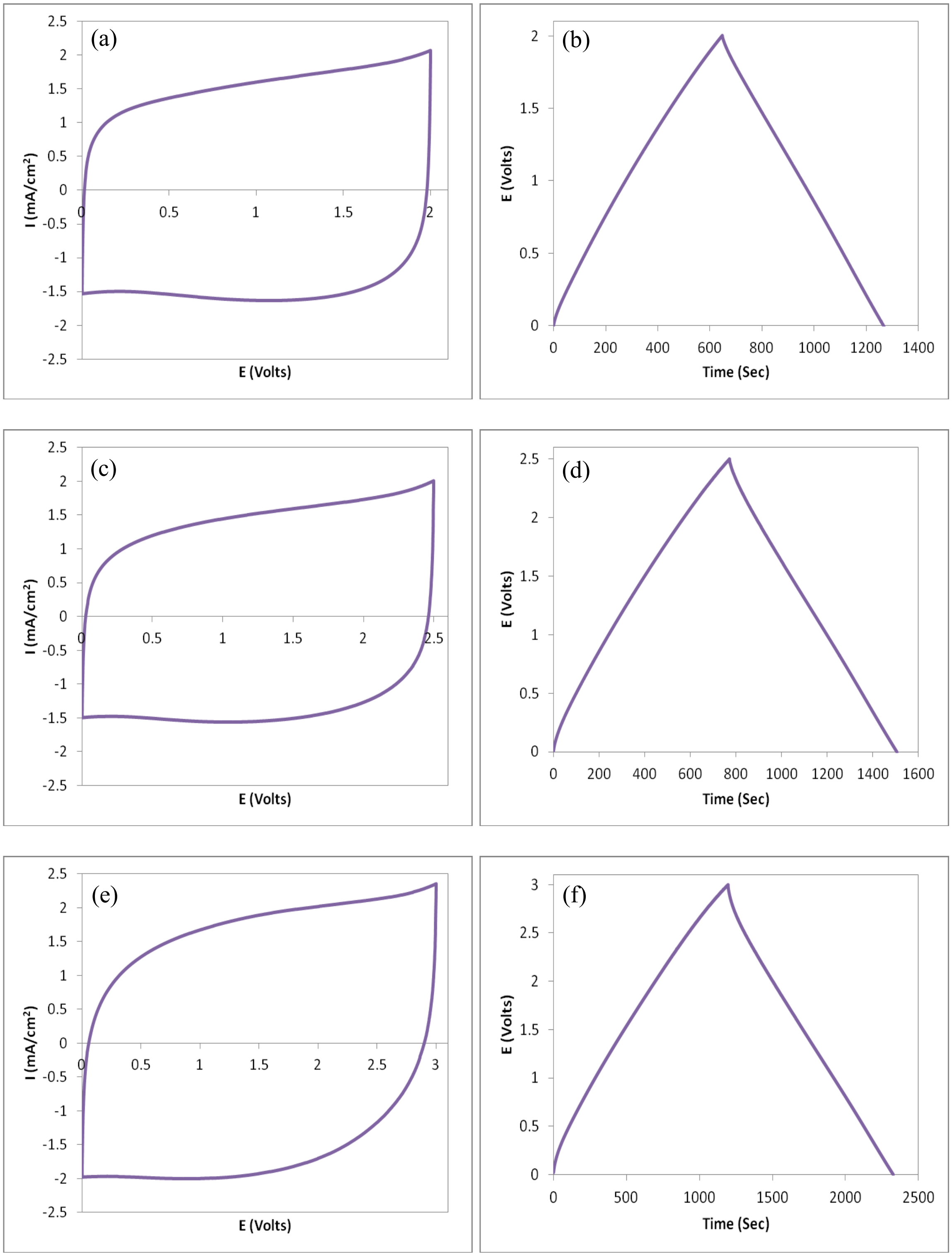

Figure 6.3. CVs taken at 10 mV/s (left) and GCs taken at 0.5 mA (right) for 4 wt% nitrogen modified carbon tested at working voltages of (a, b) 2V, (c, d) 2.5V, and (e, f) 3V.

Table 6.3. Capacitance normalized to mass and surface area for nitrogen modified carbon tested at high working voltages.

Working voltage	Gravimetric Capacitance (F/g)	Capacitance Based on Total Surface Area (F/m^2)
2V	87.8	0.509
2.5V	83.2	0.483
3V	82.9	0.481

The capacitance calculated from the GC curves and listed in Table 6.3 show the detrimental effect that the increased resistance has on the charge storage. Unlike the unmodified carbon samples, the capacitance decreases as the working voltage increases. This may be due to the nitrogen coating decomposing at the higher working voltages, causing the decomposition products to accumulate in the pores and preventing further charge storage. However, like the unmodified carbon samples, the energy density increases significantly as the working voltage increases. As shown in Table 6.4, the energy density more than doubles for nitrogen modified carbon when the working voltage is raised from 2V to 3V. The power density also increases as the working voltage increases, experiencing the highest value at 3V instead of peaking at 2.5V like for unmodified carbon. Figure 6.4 and Table 6.4 show that the highest ESR occurs at a working voltage of 2.5V, which leads to a lower power density.

Table 6.4. Energy density, power density, equivalent series resistance (ESR), and charge transfer resistance (R_{CT}) for nitrogen modified carbon tested at higher working voltages.

Working Voltage	Energy Density (Wh/kg)	Energy Density (Wh/km^2)	Power Density (W/kg)	Power Density (W/km^2)	ESR (Ω)	R_{CT} (Ω)
2V	48.9	284	142	825	2.18	3.06
2.5V	72.5	421	223	1291	2.74	7.46
3V	104	601	222	1288	2.19	16.2

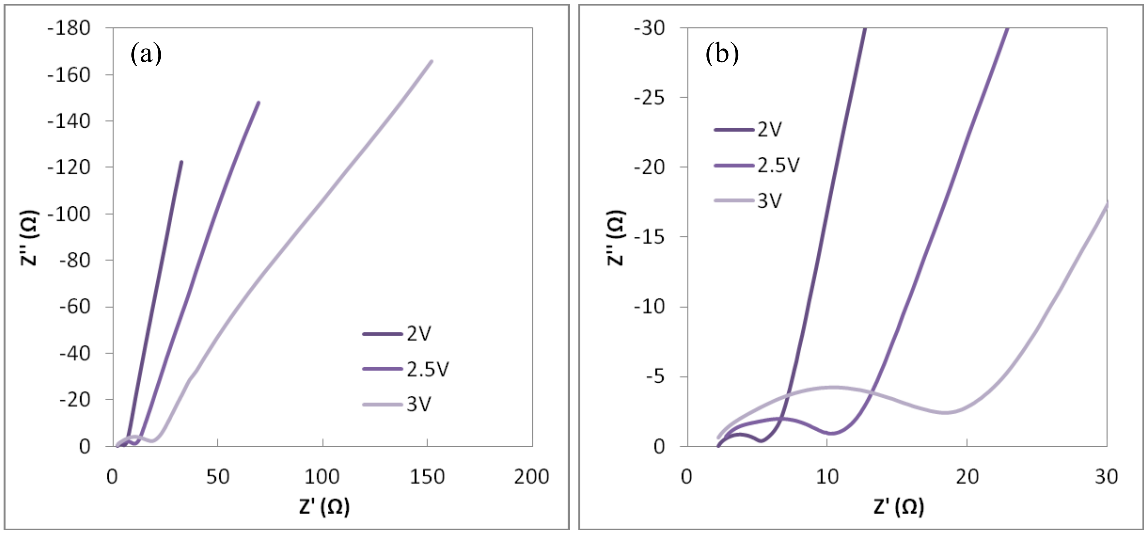

Figure 6.4. Nyquist plots for unmodified carbon (a) over the entire frequency range and (b) at high frequency only. Diffusivity resistance and charge transfer resistance increase as the working voltage increases.

When comparing unmodified carbon to nitrogen modified carbon tested at higher working voltage, the nitrogen modified carbon has a higher gravimetric capacitance than the unmodified carbon when tested at 2V. Unmodified carbon reaches 80.2 F/g, while nitrogen modified carbon is almost 10% higher, reaching 87.8 F/g. However, when the working voltage increases to 2.5V and 3V, the unmodified carbon has a higher gravimetric capacitance. Similarly, because energy density depends directly on capacitance, nitrogen modified carbon has a greater energy density at 2V, but unmodified carbon has a larger energy density at 2.5V and 3V, as seen in Figure 6.5a. Unmodified carbon also has higher power density at all working voltages, likely due to the material's smaller equivalent series resistance. Additionally, as noted in Section 5.3.1.3, coating the pore surfaces with nitrogen increases the mass of porous carbon. This overshadows the pseudocapacitive contribution due to the added nitrogen. As such, it is also useful to normalize the capacitance, energy density, and power density to the total surface area of the materials. Nitrogen modification clearly enhances the performance at each of the three working voltages. The capacitance based on total surface area can be up to 4 times higher for nitrogen modified carbon when compared to unmodified carbon. Energy density and power density normalized to total surface area are also significantly higher for nitrogen modified carbon, as seen in Figure 6.5b. The difference is even larger when comparing the energy density and power density of the unmodified carbon and nitrogen modified carbon samples tested at 2V and 3V. Simply by coating highly porous carbon with nitrogen and increasing the working voltage from 2V to 3V, the resulting device can achieve 5 times the power density and 10 times the energy density. The large increase in the energy density is particularly significant because supercapacitors are notorious for having small energy densities (<10 Wh/kg) when compared to batteries (>100 Wh/kg).[12, 67] With high energy density and power density, these supercapacitors are approaching the desired performance for superior charge storage devices (Figure 1.1).

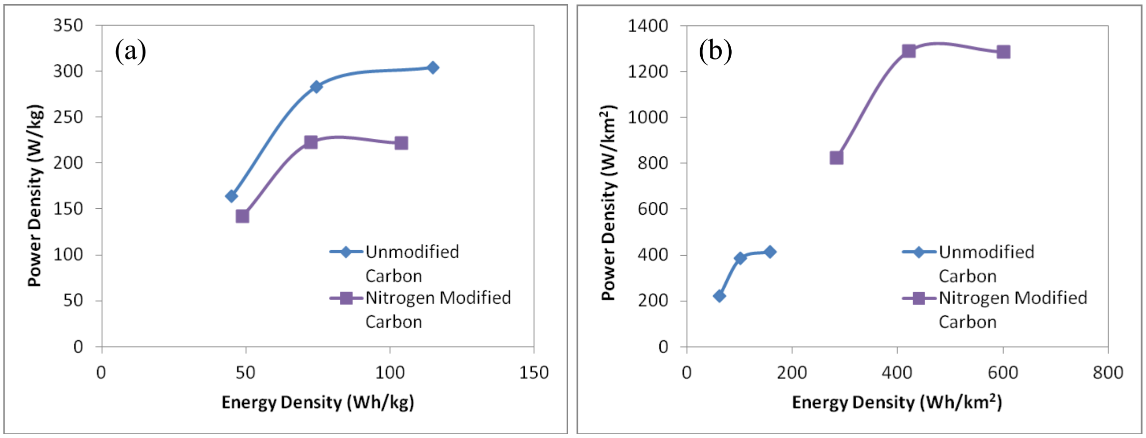

Figure 6.5. Power density vs. energy density for unmodified and nitrogen modified carbon tested at higher working voltages, normalized to (a) mass and (b) total surface area.

6.4. Cyclic stability

High working voltages can be detrimental to the cyclic stability of supercapacitors due to decomposition products partially filling the pores of the electrodes, leading to an increase in resistance and a decrease in capacitance.[10, 70] To test the effect, samples were cycled at a variety of charging rates for 500 cycles. The results are shown in Figure 6.6. Each sample experiences a capacitance drop within the first 100 cycles, which may be a result of a small amount of impurities such as oxygen in the porous carbon or water in the electrolyte. The large drop in capacitance after 100 cycles is the result of the testing conditions, as each sample was subjected to electrochemical impedance spectroscopy measurements at this point to see how the impedance changes with cycling. For the unmodified carbon, the capacitance is fairly stable after the first 100 cycles. The sample tested at 2V only decreases less than 0.5%, while the samples tested at 2.5V and 3V decrease less than 4%. For the nitrogen modified carbon, there is a much more significant decrease in capacitance for the samples tested at 2.5V and 3V, each decreasing by approximately 18%. The sudden decrease in capacitance at 100 cycles and 300 cycles for these two samples occur when the current rate increased. This suggests that the nitrogen coated material is more difficult to charge and discharge with extended cycling, possibly due to decomposition products blocking electrolyte access into the pores. However, the nitrogen modified sample tested at 2V is very stable after the first 100 cycles, decreasing less than 0.5% like the unmodified carbon sample. From this data, it is projected that the lifetimes of both the unmodified carbon and the nitrogen modified carbon samples tested at 2V can exceed 50,000 cycles.

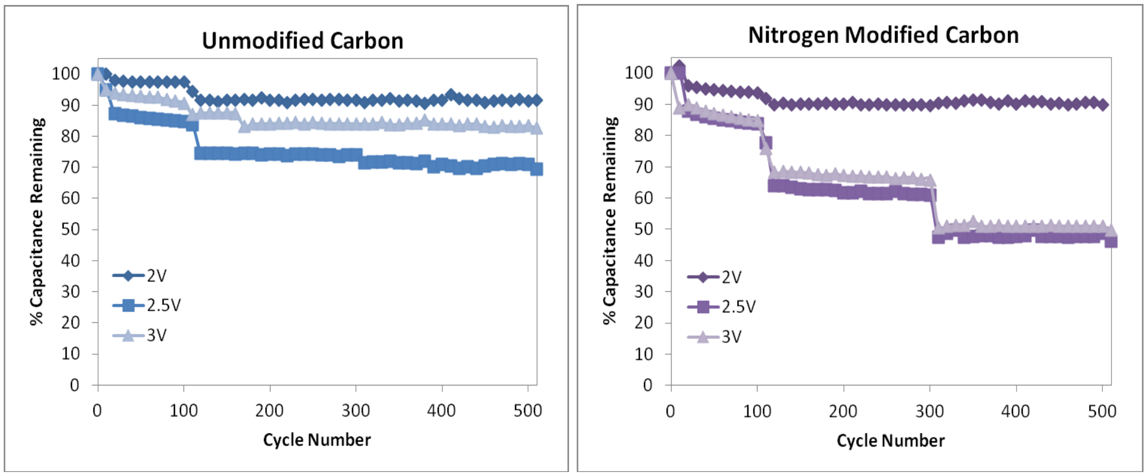

Figure 6.6. Cyclic stability of unmodified carbon and 4wt% nitrogen modified carbon tested at working voltages of 2V, 2.5V, and 3V.

To see how the resistance changes with cycling, all of the samples were measured using electrochemical impedance spectroscopy both before and after cycling 100 times. From the Nyquist plots in Figure 6.7, it can be seen that the diffusivity resistance remains largely unchanged for all samples after cycling. However, differences in the ESR and R_{CT} appear at high frequency, as shown in Table 6.5. With the exception of the unmodified carbon cycled at 2V, the ESR and R_{CT} increase for all samples after cycling, which is to be expected. At 2.5V and 3V, the R_{CT} increases by approximately 50% for unmodified carbon, but more than doubles for nitrogen modified carbon. This suggests that the nitrogen coating is breaking down at higher working voltages, increasing the resistance at the electrode/electrolyte interface and resulting in the low cyclic stability seen in Figure 6.5. However, this degradation is not seen for the nitrogen modified carbon cycled at 2V. This sample experiences only a small change in ESR and R_{CT} after cycling that is nearly identical to unmodified carbon cycled at 2V, indicating that the nitrogen coating is very stable. Together with the high capacitance, energy density, and power density, the excellent cyclic stability makes nitrogen modified porous carbon a superior material for enhanced supercapacitors.

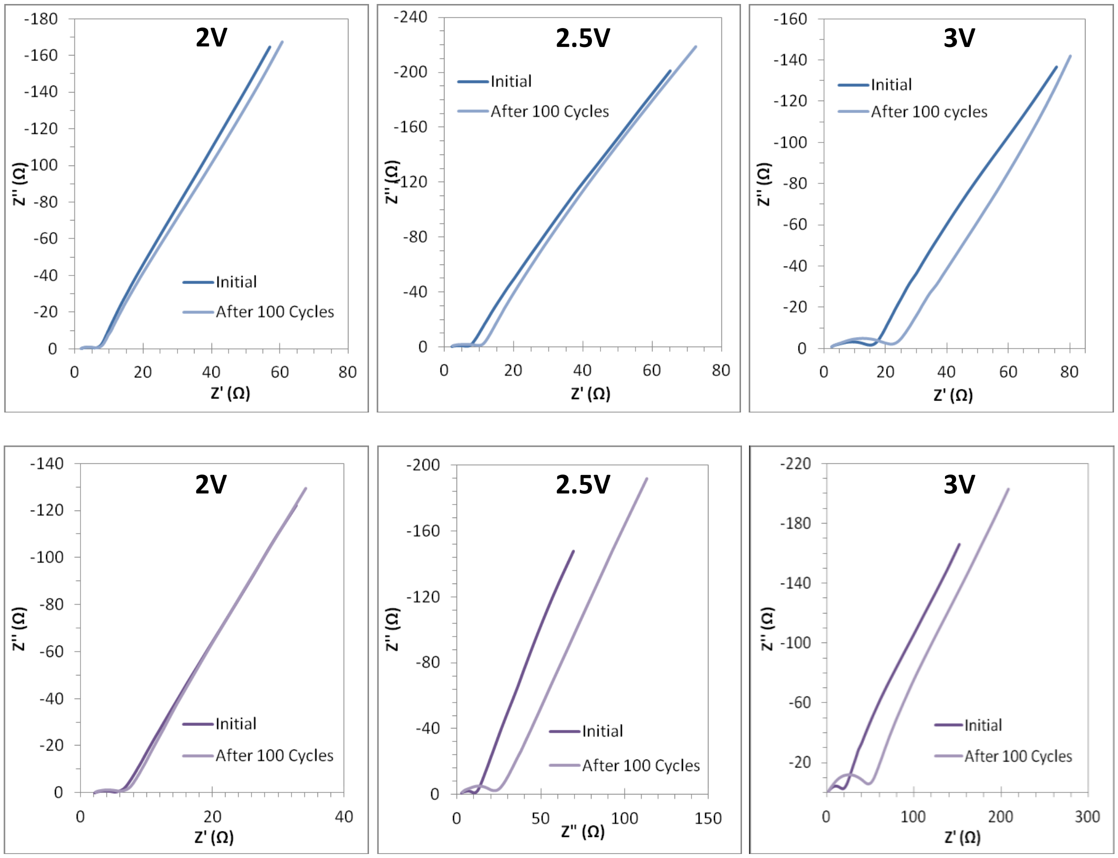

Figure 6.7. Nyquist plots for unmodified carbon (top row) and nitrogen modified carbon (bottom row) before and after cycling 100 times. Note the different axes.

Table 6.5. Equivalent series resistance (ESR) and charge transfer resistance (R_{CT}) for unmodified carbon and nitrogen modified carbon before and after cycling 100 times.

Sample	**Working Voltage**	**ESR (Ω)**		**R_{CT} (Ω)**	
		Initial	**After 100 Cycles**	**Initial**	**After 100 Cycles**
Unmodified Carbon	2V	1.92	1.82	3.79	4.45
	2.5V	2.04	2.27	4.19	9.70
	3V	2.43	2.52	15.0	19.3
Nitrogen Modified Carbon	2V	2.18	2.24	3.06	3.70
	2.5V	2.74	2.99	7.46	14.8
	3V	2.19	2.28	16.2	45.5

6.5. Summary

Energy density and power density both depend on the working voltage squared, so increasing the working voltage even a small amount can have a significant impact on these values. Unmodified carbon and nitrogen modified carbon were tested at 2V, 2.5V, and 3V. For unmodified carbon, double layer formation was retained and the capacitance increased as the working voltage increased. Despite a slight increase in resistance, the energy density and power density also increased when the working voltage was raised from 2V to 3V. Nitrogen modified carbon showed a decrease in capacitance as the working voltage increased, likely due to decomposition of the nitrogen coating as suggested by a significantly increased resistance. However, like unmodified carbon, the energy density and power density also increased when working voltage was raised from 2V to 3V. Comparing unmodified and nitrogen modified carbon, unmodified carbon shows better performance at high working voltage when normalized to mass. But when the performance is normalized to total surface area, nitrogen modified carbon is significantly better. Cyclic stability does decrease at higher working voltages, especially for nitrogen modified carbon due to increasing resistance with cycling. However, at 2V, nitrogen modified carbon retains its capacitance as well as unmodified carbon.

7. *Lignin as a novel precursor for highly porous carbon*

7.1. Introduction

Lignin is a complex polymer that is one of the three main components of wood and other biomass feedstocks, such as agriculture residue and cork. Most biomass is composed of three components: cellulose, hemicellulose, and lignin. It is one of the most common polymers in the world, second only to cellulose, and production reaches more than 50 million tons/year. However, there is little market for its use. Lignin is primarily a waste product from the paper milling industry. While there are a few applications, such as in wood adhesives and tanning agents, most lignin is simply burned as fuel.[1]

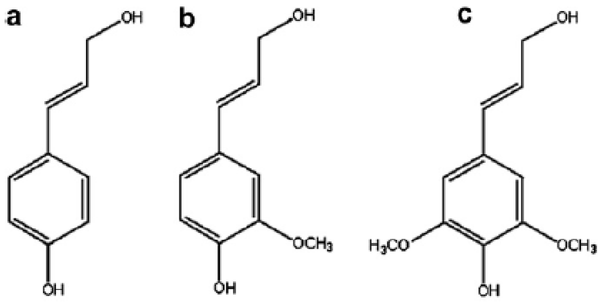

Figure 7.1. Lignin precursors: (a) *p*-coumaryl alcohol, (b) coniferyl alcohol, and (c) sinapyl alcohol.[1]

The chemical structure of lignin is highly complex and difficult to measure. It is dependent on the plant species and the method used to isolate the lignin from biomass. However, all lignin are polymerized from the three precursors shown in Figure 7.1. Lignin derived from wood can be divided into two broad classes based on their composition: softwood and hardwood. Softwood lignin is typically made of coniferyl alcohol units while hardwood lignin is made of coniferyl and sinapyl alcohol units. Lignin from grass contains *p*-coumaryl alcohol, coniferyl alcohol, and sinapyl alcohol units. An example lignin structure is shown in Figure 7.2. However, since lignin is highly polydisperse, some molecules can be 100 times larger than the one shown here.[1] Lignin consists of phenylpropane units linked together through ether-carbon and carbon-carbon bonds.[133]

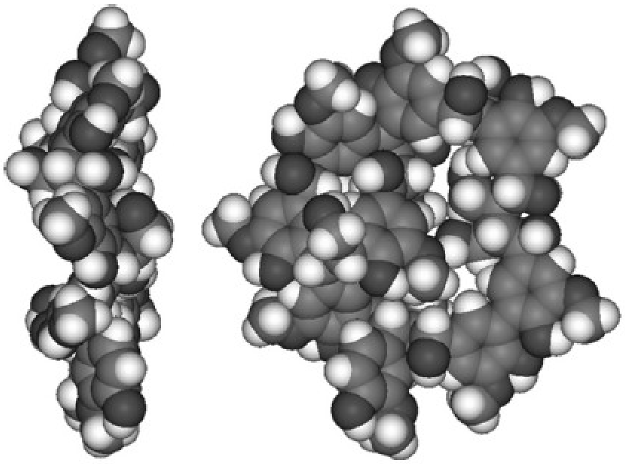

Figure 7.2. Sample lignin structure.[1]

Since lignin is a phenolic polymer, it is structurally similar to the resorcinol-furaldehyde system. As such, it is possible that lignin can also form a three-dimensional cross-linked network though sol-gel processing. Most of these studies incorporate lignin with other precursors to form blends. For example, a few studies have shown that lignin can be substituted for some or all of the phenol in phenol-formaldehyde resins (analogous to resorcinol-furaldehyde) without a significant decrease in performance.[134, 135] Another study shows that lignin can be copolymerized with acrylamide and poly(vinyl alcohol).[133] Lignin also can be crosslinked when mixed with NaOH and epichlorohydrin.[136] Many of these studies investigate these blends for their swelling behavior, measuring water uptake, but unfortunately not surface area. Additionally, there has been very limited study on the production of porous carbon from lignin for energy storage applications.

In order for lignin-derived carbon to be a good candidate for supercapacitors, emphasis must be placed on creating a material with high surface area and limited impurities. The latter is a particular challenge, not only because it is a natural product, but also due to the harsh processing needed to isolate cellulose from lignin. In the paper milling industry, in order to separate the desired cellulose from unwanted lignin, the chemical bonds between them must be broken. There are two methods to do so that are common in industry: sulfite pulping and sulfate pulping (also known as kraft processing). In sulfite pulping, salts of sulfurous acid, such as Na_2SO_3 and $CaSO_3$, are used to extract lignin from wood. Kraft processing is the more commonly used method, which requires NaOH and Na_2S as reagents.[1] Both of these processing methods can leave behind impurities in the lignin, which add to the impurities that are already naturally occurring in the material. The amount of ash impurities in lignin, mainly silica with lesser amounts of sodium, calcium, and other metals, can reach up to 15%.[1] These must be removed if the lignin is to be used as a porous carbon precursor, as metal impurities are highly detrimental to supercapacitor performance. The goal of this research is to use sol-gel processing to control both the porous structure and the surface chemistry of lignin-derived carbon for supercapacitor applications.

7.2. Alkali lignin

The first lignin used as a carbon precursor is referred to as alkali lignin and was isolated from biomass by the kraft process. The molecular structure is shown in Figure

7.3. Alkali lignin has a weight average molar mass (M_w) of approximately 10,000 and total impurities are 4% (present as sulfur) according to the manufacturer Sigma Aldrich.

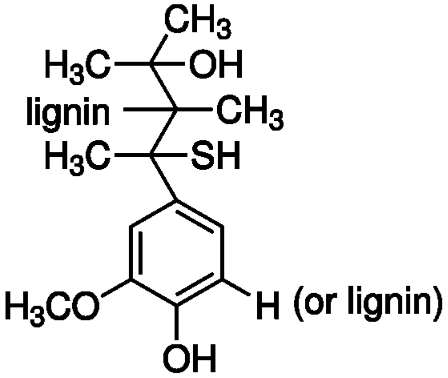

Figure 7.3. Molecular structure of alkali lignin.

To make a gel, several different sol recipes were tested. The lignin to hexamine mass ratio was varied between 1.8 and 2.4 and the solid content (calculated using the mass of the precursors divided by the mass of solvent) was varied between 5.7% and 67.6%. In general, lignin is added to DI water in a glass vial. The lignin is added to in several steps to get complete mixing, as a sticky tar can form if the lignin is added all at once. Next, hexamine is added and the mixture is stirred on a stirplate. Finally, the sol is sealed in the vial and it is cured in an oven at either 100°C or 80°C for 7 days or more depending on the sol recipe. After gelation and aging, the organic gel is dried for several days using a freeze dryer.

Pyrolysis takes place in a tube furnace under nitrogen gas flow. Samples were heated to 900°C at a ramp rate of 5°C/min. It is then held at the elevated temperature for 3 hours then cooled to room temperature. Electrodes for electrochemical measurements are prepared as described earlier and TEATFB in propylene carbonate/dimethylcarbonate is used as the electrolyte.

Nitrogen sorption isotherms were used to determine the surface area of the prepared carbon cryogels. Measurements were taken of the dried organic gels before pyrolysis. Table 7.1 compares the different recipes and their resulting specific surface areas. Samples 6, 7, 9, and 10 were not able to form gels upon curing at high temperature. For samples 6 and 7, this is thought to be due to a solid content that is too low. For samples 9 and 10, the oven temperature was not high enough. Interestingly, sample 9 gelled when it was moved to an oven at 100°C after being in an oven at 80°C for 2 weeks without gelling. Samples 5 and 8 have the highest surface area of all the remaining samples. These two samples had the least amount of shrinkage upon freeze drying, suggesting the formation of a stronger crosslinked network during gelation.

Table 7.2 shows the surface area, pore volume, and pore size for sample 8 before and after pyrolysis at 900°C. The pore structure remains fairly consistent after pyrolysis, with the overall surface area increasing slightly. However, on the whole, the surface area and pore volume are very low relative to the resorcinol-furaldehyde carbon prepared in the previous Sections 5 and 6. What little porosity that is present appears to be only mesopores; nitrogen sorption isotherms give no indication of the existence of micropores in this sample. Even though mesopores are important for electrolyte ion transport in supercapacitor electrodes, micropores contribute the most surface area and are therefore necessary to achieve high capacitance. However, the above results do show that it is possible to tune the pore structure of lignin-derived carbon by adjusting the precursor to catalyst ratio and the solid content of the sol before gelation. While the low surface area and pore volume are an indication that alkali lignin may not be an ideal precursor, other lignins may be more suitable for the formation of a highly porous carbon.

Table 7.1. Recipes of various sols made from alkali lignin and their corresponding specific surface areas.

Sample	Lignin to Hexamine Mass Ratio	Solid Content (Mass %)	Oven Temperature (°C)	Specific Surface Area (m^2/g)
1	2.4	56.6	100	7.28
2	2.4	56.6	100	5.14
3	2.25	67.7	100	31.9
4	2	60.8	100	24.3
5	1.75	67.6	100	26.6
6	1.8	11.4	100	-
7	1.8	5.7	100	-
8	1.8	28.4	100	38.3
9	2.4	67.6	80	-
10	1.8	28.4	80	-

Table 7.2. Surface area, pore volume, and pore size of sample 8 before and after pyrolysis at 900°C. Nitrogen sorption isotherms gave no indication of micropores.

Sample	Surface Area (m^2/g)			Pore Volume (cm^3/g)		Pore Diameter (nm)	
	Total	Mesopores	Micropores	Mesopores	Micropores	Mesopores	Micropores
Before pyrolysis	38.3	37.5	-	0.058	-	3.2	2.6
After pyrolysis	45.8	37.5	-	0.059	-	3.7	2.6

7.3. Na lignosulfonate and Na kraft lignins

Two new lignins are tested as precursors to make carbon cryogels, referred to as Na lignosulfonate and Na kraft. They are isolated from woody biomass using sulfite pulping and the kraft process, respectively. The structure and molecular weight of these lignins is unknown, as well as the amount of impurities. Both are commercially available. The manufacturer of Na kraft lignin is Mead Westvaco, where it is under the tradename

Indulin C. It is also referred to as sodium salt of kraft pine lignin and is primarily used as a dispersant for slow-setting asphalt emulsions.

To make sols, each lignin was mixed into DI water in steps as was done with the alkali lignin. The lignin to hexamine mass ratio was set to 1.8. After the lignin was stirred into DI water, hexamine was added. The mixture was sealed and placed in an oven at 100°C for 7 days. During sol preparation, the Na kraft lignin was quick to dissolve in water, but a significant amount of the lignosulfonate lignin did not dissolve, even after continuous mixing. Some solids remained in that latter sol after heating, both suspended in the liquid and settled at the bottom of the vial, and the lignosulfonate did not form a gel after 7 days at elevated temperature. In contrast, the Na kraft lignin gel needed only one day to gel, which is faster than the several days required by the alkali lignin. The Na kraft lignin gel was kept in the oven for the remaining six days for aging, which strengthens the newly formed crosslinked network. Because of its excellent solubility in water and fast gel formation, future experiments will focus on Na kraft lignin only.

Table 7.3 shows the surface area, pore volume, and pore size for the lignin gel before and after pyrolysis at 900°C. Like the alkali lignin gels, there is no evidence of microporosity. The Na kraft gels also have relatively low surface area and pore volume. One possibility for these low values is the presence of metal impurities in the lignin precursor. If the amount of impurities is high, this could affect polycondensation during gelation by limiting reactive sites or the impurities could be blocking the pores, preventing measurement with nitrogen sorption.

Table 7.3. Surface area, pore volume, and pore size of Na kraft lignin gel before and after pyrolysis at 900°C.

Sample	Surface Area (m^2/g)			Pore Volume (cm^3/g)		Pore Diameter (nm)	
	Total	**Mesopores**	**Micropores**	**Mesopores**	**Micropores**	**Mesopores**	**Micropores**
Before pyrolysis	26.4	38.2	-	0.078	-	4.2	2.6
After pyrolysis	35.2	54.3	-	0.095	-	3.7	2.3

To investigate whether impurities are blocking pores, Na kraft lignin gels were washed with either water or ethanol prior to freeze drying. The water wash helped to increase the surface area slightly while the pore volume remains about the same. Washing with ethanol, on the other hand, significantly increases both the surface area and pore volume. The average micropore size decreases by more than 0.5 nm, suggesting that some smaller micropores are being opened up by the ethanol wash. Unfortunately, the microporosity that might be present is still too low to be calculated for micropore surface area and pore volume. While this washing method does show promise, it is thought to be more important to remove metal impurities before gelation to allow for better crosslinking.

Table 7.4. Surface area, pore volume, and pore size of Na kraft lignin gels that have been washed with either water or ethanol prior to freeze drying.

Sample	Surface Area (m^2/g)			Pore Volume (cm^3/g)		Pore Diameter (nm)	
	Total	**Mesopores**	**Micropores**	**Mesopores**	**Micropores**	**Mesopores**	**Micropores**
Water wash	38.7	43.9	-	0.072	-	3.2	2.7
Ethanol wash	123.5	200.9	-	0.345	-	3.7	2.0

7.4. Purified lignin-derived carbon cryogels

7.4.1. Synthesis

Impurities in Na kraft lignin were removed using an acid precipitation method. First, lignin is mixed in an excess of deionized water. Then about 20 wt% of acetic acid is added to the mixture and it is stirred. The acid dissolves the metal impurities into the solvent and the purified lignin forms a precipitate. The mixture is frozen to flocculate the lignin and then allowed to thaw. The product is separated from the liquid using filter paper. The purified lignin is rinsed with DI water, then collected and dried.

Purification affected the solubility characteristics of the lignin. When the lignin was added to DI water, it did not completely dissolve like it had before purification. To solve this problem, ethanol was slowly added to the mixture until the lignin completely dissolved. This occurs at a 50/50 mixture of water and ethanol. To make a gel, the purified lignin is stirred into the solvent mixture in steps to get complete mixing. Next, hexamine is added to the mixture. The sol is sealed and cured in an oven at 100°C for 7 days. Gelation occurs in about two days, and the remaining five days allow for aging.

A solvent exchange step was necessary before freeze drying. The ethanol and water mixture in the gel will not freeze, which creates pore collapse due to capillary forces as the liquid is pulled away from the solid. Therefore, the solvent mixture was replaced with another solvent that will freeze, such as tert-butanol. The wet lignin gel is placed in 10 times its volume of tert-butanol three times, using fresh solvent each time and allowing 24 hours between each step. After the solvent exchange, the gel can be freeze dried.

For carbonization, the dried organic gel is pyrolyzed at high temperature to remove the unwanted organic functional groups. This is performed in a tube furnace under a nitrogen gas flow. The sample is heated to various temperatures between 340°C and 900°C at a ramp rate of 5°C/min. It is then held at the elevated temperature for 3 hours then cooled to room temperature. Activation is performed by heating the pyrolyzed sample in air to 250°C at a ramp rate of 5°C/min. The sample is held at 250°C for 97 minutes (dwell time determined by TGA), then heated to 450°C in nitrogen for 3 hours to remove any unwanted functional groups that may have developed during activation. Electrodes for electrochemical measurements are prepared as described earlier and TEATFB in propylene carbonate/dimethylcarbonate is used as the electrolyte.

7.4.2. Effect of purification on pore structure

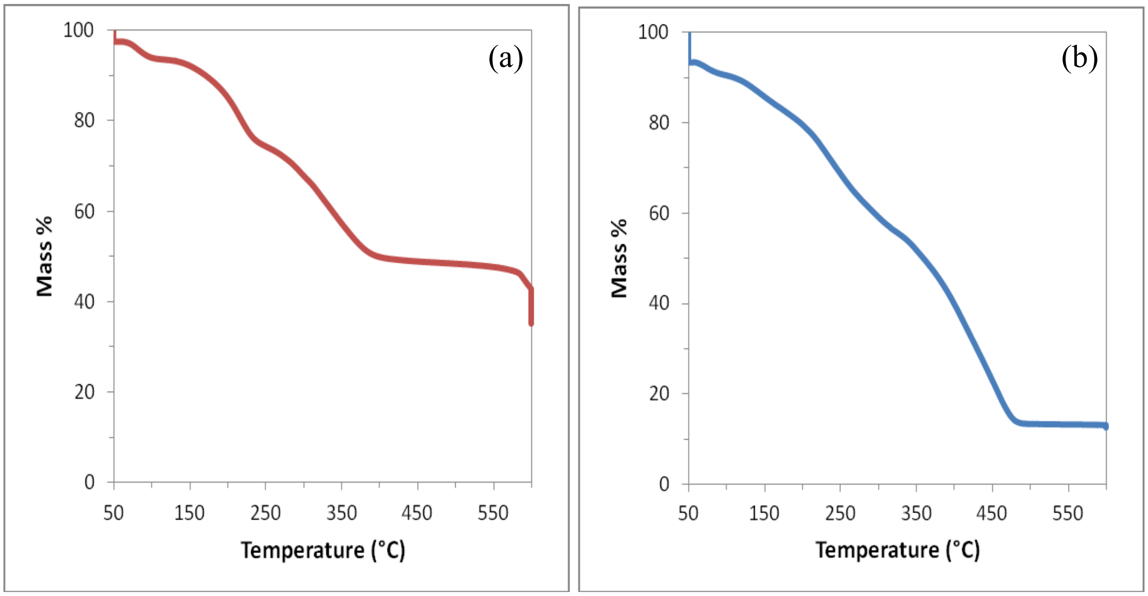

Figure 7.4. TGA showing the weight loss of lignin through oxidation and pyrolysis: (a) without purification and (b) with purification. Purification reduces the amount of ash to less than 50% of the original amount.

To see the effect of purification using the acid precipitation method, the ash content was measured using thermal gravimetric analysis. Lignin samples with and without purification were burned in air up to 600°C to remove all carbon, leaving behind inorganic impurities in the form of ash. The results are shown in Figure 7.4. Purification of the lignin through the acid precipitation method reduces the amount of ash to less than 50% of the original amount. Before purification, the ash content is 35.6 wt%, but after purification, it is reduced to 12.5 wt%. EDX elemental analysis reveals that some sodium remains as an impurity even after purification. There is also a significant amount of oxygen, which could pose a problem in later electrochemical measurements.

Nitrogen sorption reveals the benefit of impurity reduction on the pore structure of carbon cryogels. As seen in Table 7.5, the unpurified lignin-derived carbon cryogel has a surface area of only 26.4 m^2/g, while purification results in an increase to 189.1 m^2/g. The mesopore volume also significantly increases with purification, as illustrated by the mesopore size distributions in Figure 7.5a. Without purification, the carbon cryogel has very few small mesopores, but with purification, there are much more mesopores with a wider pore side distribution. The micropore size distribution in Figure 7.5b shows the same trend, with purification causing the micropore volume to increase. The enhanced pore structure resulting from lignin purification before synthesis is thought to be due to a higher occurrence of cross-linking events during gelation. Without excess impurities blocking these events, the precursors have the freedom to create a more porous 3-dimensional networked structure.

Table 7.5. Surface area, pore size, pore volume of lignin-derived carbon cryogels before purification and after purification.

Sample	Surface Area (m^2/g)			Pore Volume (cm^3/g)		Pore Diameter (nm)	
	Total	Mesopores	Micropores	Mesopores	Micropores	Mesopores	Micropores
Unpurified lignin	26.4	38.2	-	0.078	-	4.2	2.6
Purified lignin	189.1	179.8	-	0.698	-	21.1	1.9

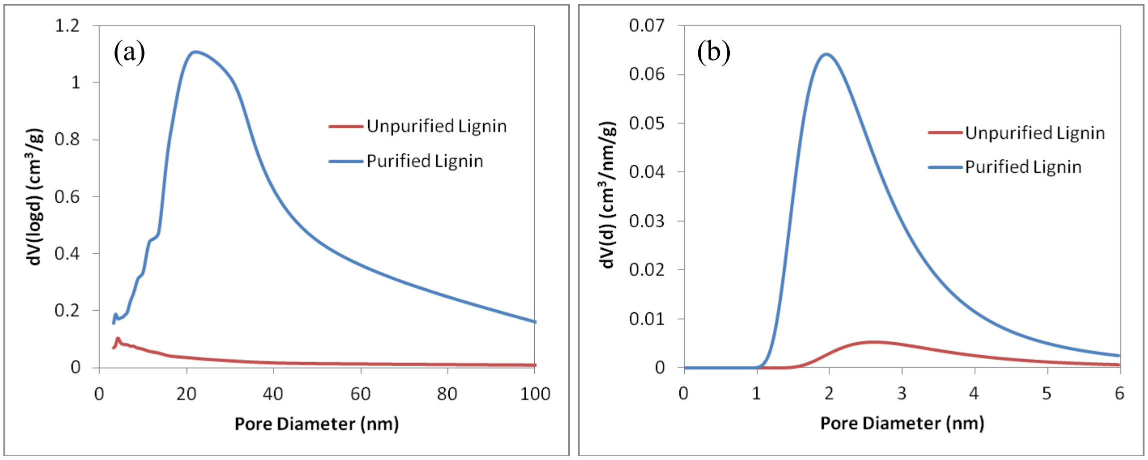

Figure 7.5. (a) Mesopore and (b) micropore size distributions of lignin-derived carbon cryogels before and after purification. The pore volume increases drastically with purification.

7.4.3. Varying pyrolysis temperature

To create high surface area porous carbons through sol-gel processing, pyrolysis temperature is an important factor to consider. Resorcinol-furaldehyde cryogels pyrolyzed at 900°C result in a highly porous carbon that retains the pore structure of the original cryogel (Section 4). However, pyrolysis at this temperature for lignin-derived cryogels results in a surface area that is much lower than expected. The lignin-derived cryogel before pyrolysis has a total surface area of 189.1 m^2/g, but it was reduced to only 20.6 m^2/g after pyrolysis. The large decrease in surface area could be an indication of shrinkage or sintering of the material at high temperature. SEM images of a sample pyrolyzed at 900°C are shown in Figure 7.6. The sample shows porosity, but with a smoother texture and less well-defined nanoparticles than seen in resorcinol-furaldehyde carbon cryogels. The nanoparticles are also relatively large, with the smallest being approximately 65 nm in diameter and the largest greater than 100 nm.

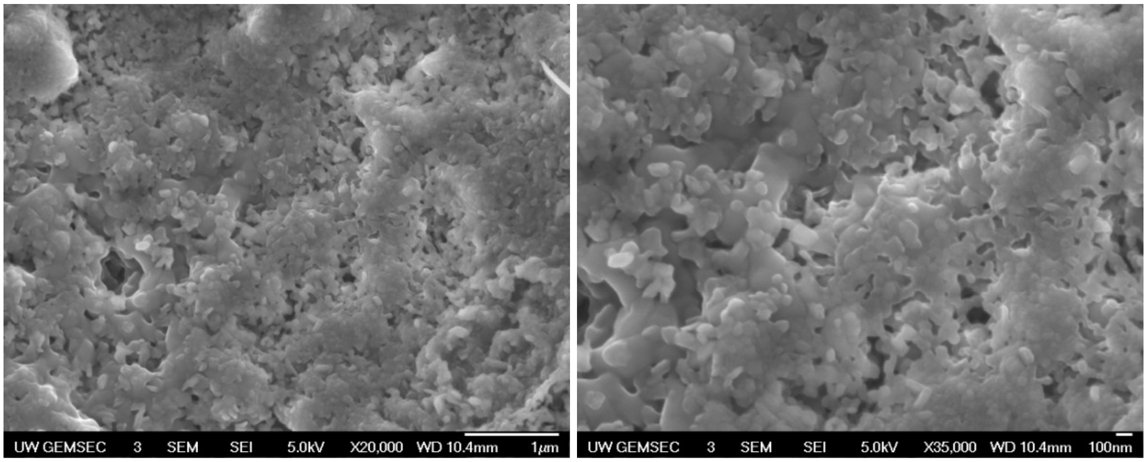

Figure 7.6. SEM images at different magnifications for a lignin cryogel pyrolyzed at 900°C. Particle sizes range from approximately 65 nm to over 100 nm in diameter. The relatively smooth texture and less well-defined nanoparticles when compared to resorcinol-furaldehyde carbon cryogels suggest sintering during pyrolysis.

To prevent sintering, a range of lower pyrolysis temperatures were tested, and the resulting nitrogen sorption isotherms are shown in Figure 7.7 and corresponding surface areas, pore volumes, and pore diameters are listed in Table 7.6. Decreasing the pyrolysis temperature from 900°C to 550°C increased the total surface area. Lowering further to 450°C resulted in a total surface area and pore volume that were nearly identical to the dried lignin gel before pyrolysis. Micropores were also developed upon pyrolysis at lower temperatures between 550°C and 405°C, with pyrolysis at 450°C having the largest contribution from micropores to the overall surface area. However, as the pyrolysis temperature is lowered further to 340°C, the surface area decreases again and micropores are no longer present. Because of the high surface area and pore volume, the sample pyrolyzed at 450°C was selected for further processing.

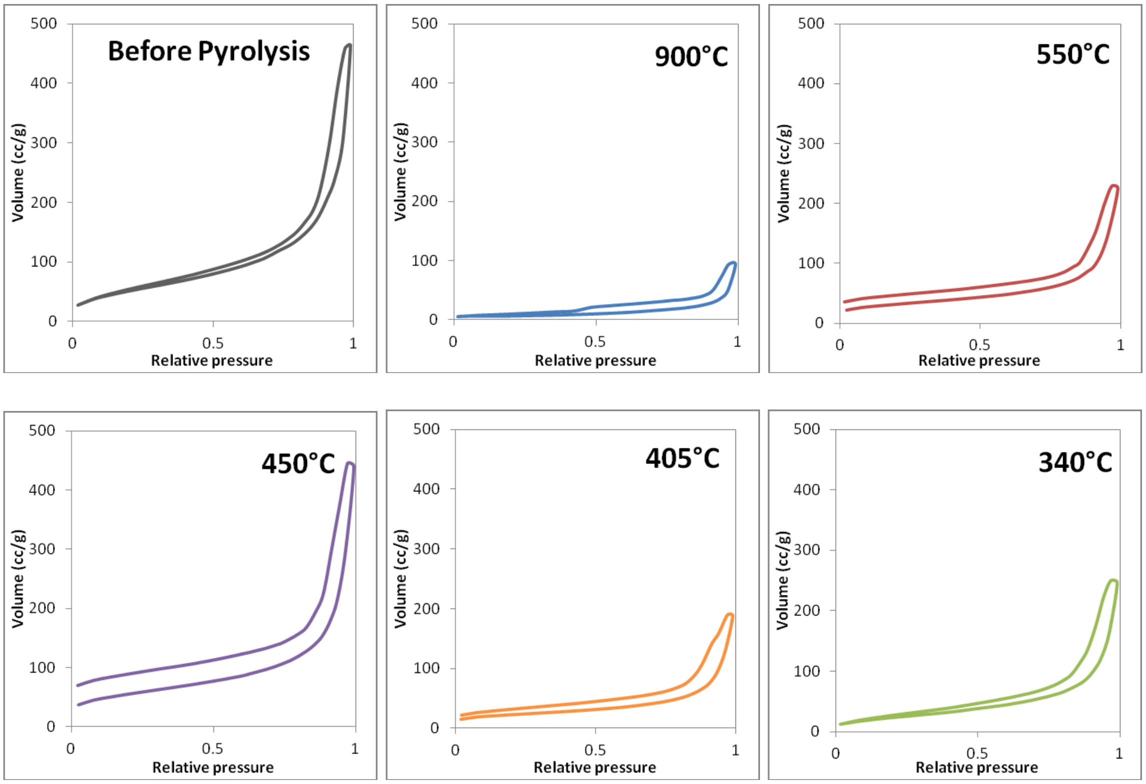

Figure 7.7. Nitrogen sorption isotherms for purified lignin pyrolyzed at various temperatures.

Table 7.6. Surface areas, pore volumes, and pore sizes for lignin-derived carbons pyrolyzed at various temperatures. Because of the variance, the mesopore surface area, pore volume, and pore size is shown for both the adsorption (ad) and desorption (de) isotherms.

Pyrolysis temperature	**Surface Area (m^2/g)**				**Pore Volume (cm^3/g)**			**Pore Diameter (nm)**		
	Total	**Meso (ad)**	**Meso (de)**	**Micro**	**Meso (ad)**	**Meso (de)**	**Micro**	**Meso (ad)**	**Meso (de)**	**Micro**
Before pyrolysis	189.1	148.9	179.8	-	0.690	0.698	-	3.2	21.1	1.9
900°C	20.6	24.0	53.1	-	0.145	0.150	-	5.5	3.6	1.7
550°C	106.5	61.7	76.1	20.72	0.320	0.309	0.012	3.2	16.5	1.7
450°C	188.8	115.0	138.5	28.06	0.635	0.603	0.016	3.2	21.0	1.7
405°C	75.3	49.8	72.1	10.91	0.275	0.271	0.006	5.4	16.4	1.7
340°C	88.3	76.8	108.6	-	0.372	0.3858	-	3.7	13.6	1.9

7.4.4. Activating lignin pyrolyzed at 450°C

7.4.4.1. Structure and composition

Physical activation of the purified lignin-derived carbon pyrolyzed at 450°C increases the surface area from 188.8 m^2/g to 258.8 m^2/g. While this value is relatively low when compared to resorcinol-furaldehyde carbon, it is still comparable to values obtained for other carbon materials, including carbon nanotubes.[9] As illustrated in Table 7.7 and Figure 7.8a, the mesopore surface area and mesopore volume decrease after activation, which is unlike what is seen for resorcinol-furaldehyde carbon cryogels. The increase in total surface area is therefore due to micropores begin revealed during activation, as can be seen by the larger micropore surface area and micropore volume in Table 7.7 and Figure 7.8b. While more micropores increase the surface area available for electric double-layer formation in supercapacitors, a large amount of mesopores are also necessary to facilitate fast diffusion of the electrolyte ions throughout the electrode material during charge and discharge.

Table 7.7. Surface area, pore volume, and pore diameter from nitrogen sorption for unactivated and activated lignin-derived carbon cryogel pyrolyzed at 450°C.

Sample	**Surface Area (m^2/g)**			**Pore Volume (cm^3/g)**		**Pore Diameter (nm)**	
	Total	**Mesopores**	**Micropores**	**Mesopores**	**Micropores**	**Mesopores**	**Micropores**
Unactivated	188.8	138.5	28.1	0.603	0.016	21.0	1.7
Activated	258.8	98.2	89.0	0.352	0.047	21.1	1.7

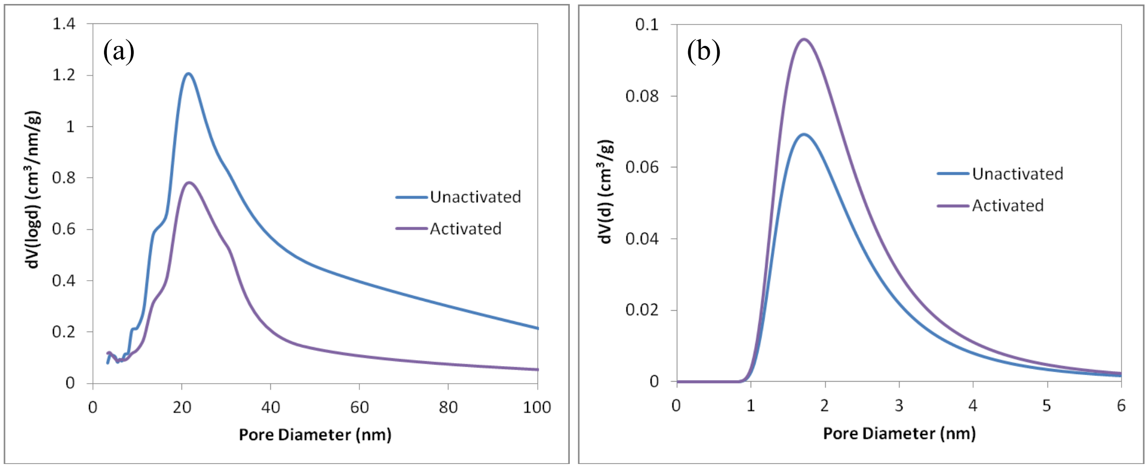

Figure 7.8. (a) Mesopore and (b) micropore size distributions for unactivated and activated lignin-derived carbon cryogels pyrolyzed at 450°C. Activation decreases the mesopore volume, but increases the micropore volume.

SEM images of the activated lignin-derived carbon are shown in Figure 7.9. The nanoparticles are more well-defined in this sample when compared to lignin-derived carbon pyrolyzed at 900°C seen in Figure 7.6. The diameters of the nanoparticles also appear to be smaller, ranging from approximately 50 to 100 nm. Overall, the nanotexture for this sample pyrolyzed at a lower temperature more closely resembles that of activated resorcinol-furaldehyde carbon cryogels (Section 4), making lignin a promising material for supercapacitors. However, elemental analysis by EDX reveals that some impurities remain in the lignin-derived carbon structure after pyrolysis and activation. As seen in Table 7.8, the purification process did not remove all of the sodium added during the isolation of lignin from biomass. Additionally, there is a large amount of oxygen left in the structure. In supercapacitors, both of these impurities can decrease conductivity and cause degradation of organic electrolyte, thereby affecting the electrochemical performance.

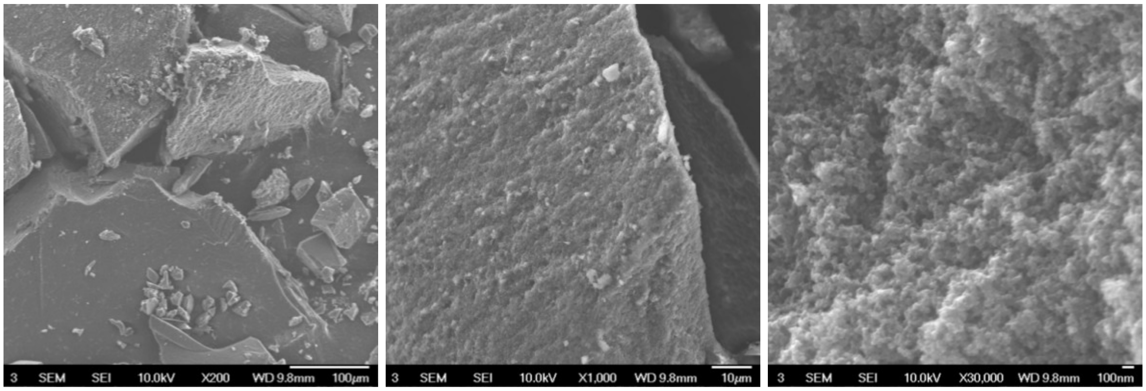

Figure 7.9. SEM images of activated lignin-derived porous carbon.

Table 7.8. Elemental analysis from EDX.

Element	Weight %	Atomic %
Carbon	84.8	89.0
Oxygen	11.1	8.8
Sodium	4.1	2.2

7.4.4.2. Electrochemical analysis

The CVs taken at 10 mV/s for lignin-derived carbon pyrolyzed at 450°C both with and without activation are shown in Figure 7.10. Each sample exhibits a very poor capacitive response. First, the measured current is extremely low, which is to be expected since the surface area is very low relative to carbon made with other well-researched precursors (e.g. resorcinol and furaldehyde). Additionally, the shape of the CV curve does not exhibit the rectangular shape characteristic to double-layer formation. Neither sample appears to store much charge until there is a sharp increase in current density as the voltage approaches 2V. They very low response may be an indication of low conductivity for the electrode material, making charging difficult. The peaks near 2V could be an indication of pseudocapacitive reactions due to the high level of impurities that remain in the lignin even after purification. With activation, the amount of oxygen functionalities often increases, which could account for the larger peak for the activated lignin-derived carbon.

Galvanic cycling also shows a low response for the lignin-derived carbon electrodes, as shown in Figure 7.11. The non-linear charging curves for each sample are unlike what is typically seen for double-layer formation. This behavior may be due to a combination of low surface area and conductivity. The large voltage drop at the beginning of each discharge curve also shows that there is increased resistance in the sample. Impurities in the lignin can hinder conductivity in the bulk by interrupting the interconnected carbon network. Additionally, the pyrolysis temperature may be too low to completely carbonize the cryogel, leading to low conductivity.

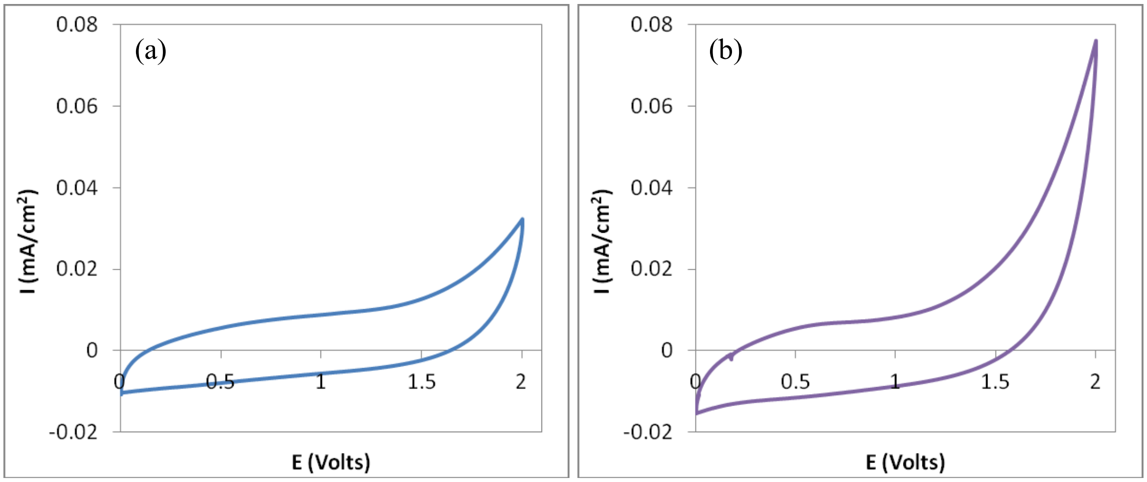

Figure 7.10. Cyclic voltammograms taken at 10 mV/s for lignin-derived carbon cryogels pyrolyzed at 450°C (a) without activation and (b) with activation.

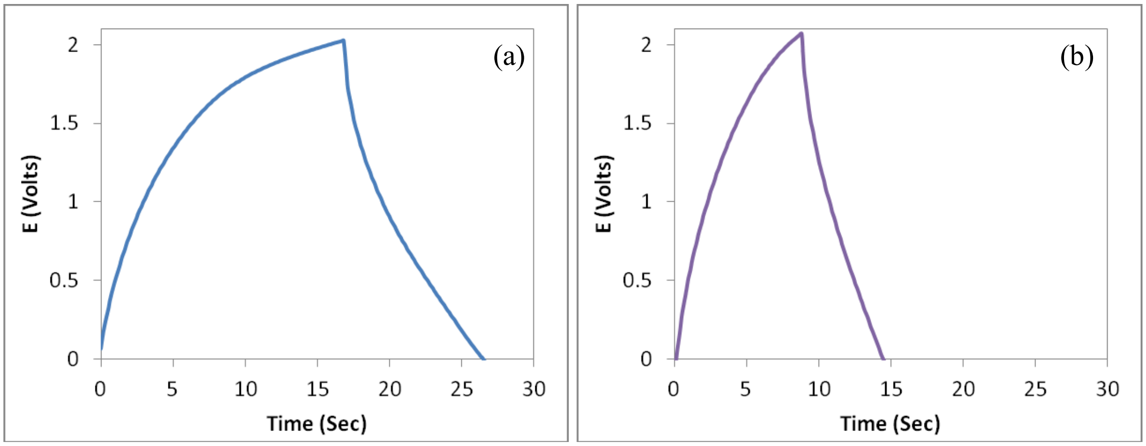

Figure 7.11. Galvanic cycling curves of lignin-derived carbon cryogel pyrolyzed at 450°C (a) without activation and (b) with activation. The smaller curve for activated lignin-derived carbon may be a result of the lower mesopore surface area and volume, making electrolyte diffusion into the pores more difficult.

The high resistance is further illustrated by the use of electrochemical impedance spectroscopy. Nyquist plots are shown in Figure 7.12. The large arch at lower frequencies indicates high resistivity to electrolyte diffusion. This is likely due to the low porosity of lignin samples. Without open porosity and high surface area, the ions in the electrolyte cannot diffuse sufficiently in the sample to form the desired electric double-layer structure. Additionally, while the ESR is relatively low, as listed in Table 7.9, it is higher than what is typically seen for resorcinol-furaldehyde carbon. This indicates that the intrinsic resistance of the electrode material is high. The charge transfer resistance is also relatively high for carbon, with the activated lignin-derived carbon having a larger value. Supporting the conclusion made from the smaller GC curve, this may be due to an increased amount of oxygen functionalities with activation, which reduces the efficiency of charging at the electrolyte/electrode interface.

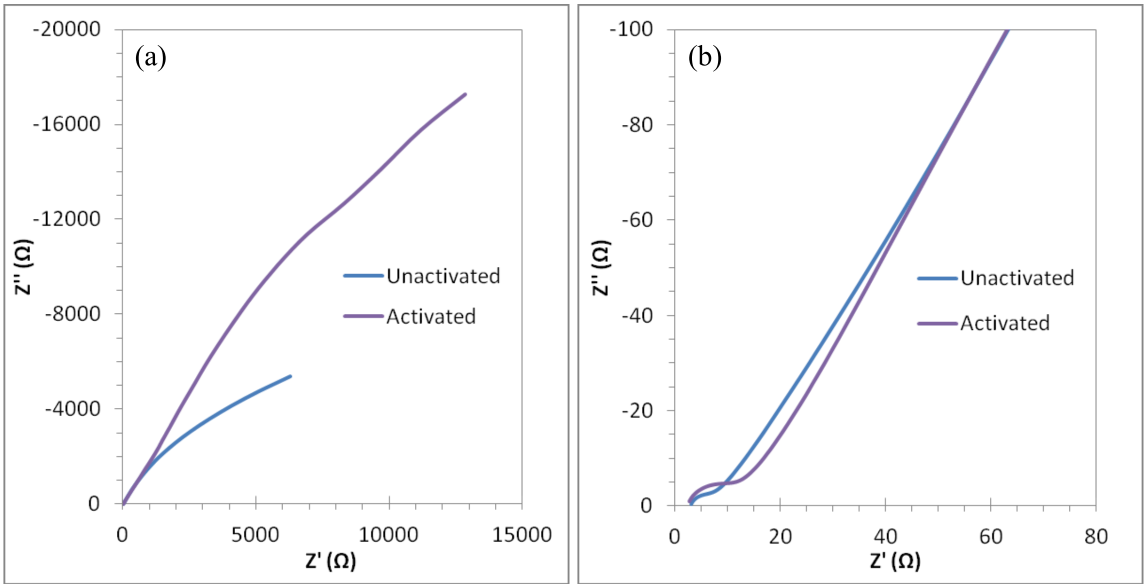

Figure 7.12. Impedance of lignin-derived carbon, showing (a) non-ideal behavior at low frequencies, and (b) a relatively high ESR and R_{CT} at high frequencies.

Table 7.9. Equivalent series resistance (ESR) and estimated charge transfer resistance (R_{CT}) for unactivated and activated lignin-derived carbon pyrolyzed at 450°C.

Sample	ESR (Ω)	R_{CT} (Ω)
Unactivated	3.05	4.51
Activated	2.77	9.18

To check the conductivity of the lignin-derived carbon electrodes both with and without activation, 4-point conductivity measurements were taken. While resorcinol-furaldehyde carbon had a relatively low resistance in ohms, both unactivated and activated lignin-derived carbon could not be measured with resistances in the megaohm range. As mentioned in Section 4.1, an organic precursor is only considered carbonaceous after it is pyrolyzed above 800°C. Below 600°C, high amounts of foreign atoms such as oxygen and hydrogen may still exist in the sample. Additionally, cyclization and aromatization may not have taken place yet. These factors combined could account for the extremely low conductivity seen for the lignin-derived carbon pyrolyzed at 450°C. Despite the possibility of low surface area, pyrolysis at a temperature above 800°C appears to be necessary to obtain a material with the high conductivity necessary for use as supercapacitor electrodes.

7.4.5. Pyrolysis at 900°C

7.4.5.1. Synthesis

Since a high level of impurities could be contributing to the low conductivity in lignin-derived carbon, it is useful to investigate whether further purification in addition to a higher pyrolysis temperature will enhance the properties of the material. Here, Na kraft lignin powder is subjected to purification once using the acid precipitation method, then half of the purified powder is purified a second time. The samples are labeled as 1x lignin and 2x lignin, respectively. The low solubility of lignin purified two times made further purification difficult.

To make a gel, the purified lignin is stirred into a 50/50 water/ethanol solvent mixture in steps to get complete mixing. Next, hexamine is added as the reactive catalyst. The sol is sealed in a vial and cured in an oven at 100°C for 7 days. Gelation occurs in about two days, and the remaining five days allow for aging. For solvent exchange before freeze drying, the wet 1x and 2x lignin gels are placed in 10 times its volume of tert-butanol three times, using fresh solvent each time and allowing 24 hours between each step. The gels are freeze dried for several days at -50°C. Pyrolysis is performed in a tube furnace under a nitrogen gas flow. The 1x and 2x lignin cryogels are heated to 900°C for 3 hours at a heating rate of 5°C/min, and labeled as 1x-900 and 2x-900, respectively.

7.4.5.2. Composition and structure

Thermal gravimetric analysis curves showing the effect of two purification steps are shown in Figure 7.13. With one purification step, the ash content is 12.5 wt%. After subjecting the lignin powder to purification a second time, the ash content is reduced to 10.3 wt%. Compared to unpurified lignin powder, this represents a reduction in the amount of ash from impurities to less than 1/3 of the initial value.

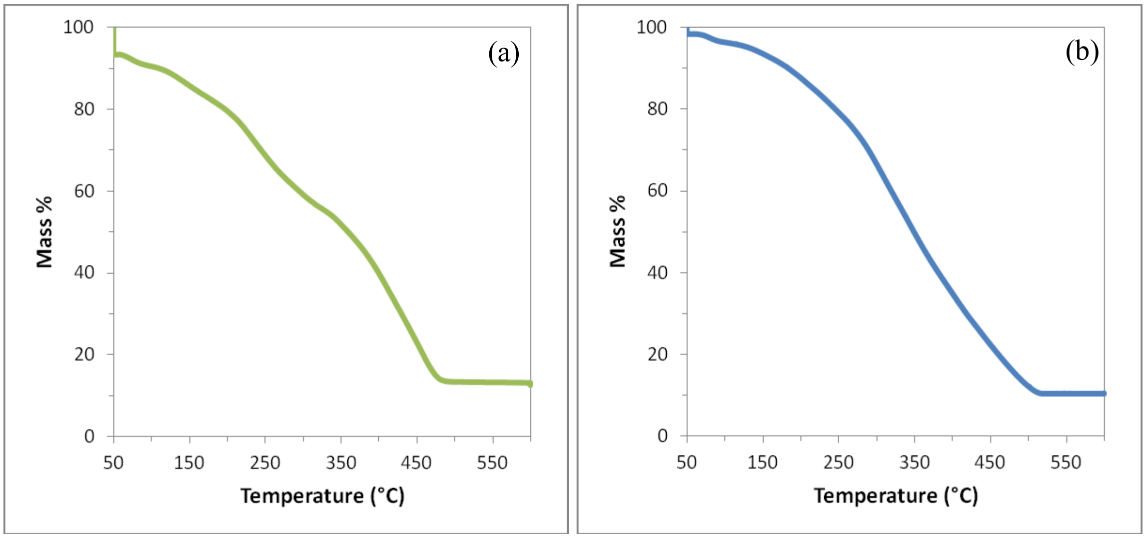

Figure 7.13. Thermal gravimetric analysis of Na kraft lignin after (a) purification once and (b) purification twice. Two purification steps reduces the ash content to less than 1/3 of the original ash content in unpurified lignin.

Energy dispersive x-ray spectroscopy (EDX) is used to determine the type and approximate amount of impurities in the lignin-derived carbon cryogel. Results for 1x-900 and 2x-900 are listed in Table 7.10. Both samples have very similar amounts of carbon, nitrogen, and oxygen. However, there is an important difference between the two samples when the sodium content is considered. For lignin subjected to purification once, the sodium content is 2.2 wt%. However, with a second purification step, the sodium content is nonexistent. This is a significant finding, as minimizing metal impurities is essential in carbon used for high performance supercapacitors. Metal impurities like sodium could react with the organic electrolyte employed in higher voltage devices, decreasing charge storage and cyclic stability. Therefore, the decreased impurity content for lignin-derived carbon that underwent two purification steps during synthesis should result in better electrochemical properties than less pure material. Not listed in Table 7.10 is the 0.7 wt% fluorine (0.4 at%) that was also measured in 2x-900. This is from the PTFE binder used during electrode fabrication and does not have any adverse effects on the electrolyte or device performance.

Table 7.10. Chemical composition by weight from EDX.

Sample	**Composition (Weight %)**				**Composition (Atomic %)**			
	Carbon	**Nitrogen**	**Oxygen**	**Sodium**	**Carbon**	**Nitrogen**	**Oxygen**	**Sodium**
1x-900	87.5	5.1	5.2	2.2	90.3	4.5	4.0	1.2
2x-900	86.4	5.3	5.7	2.0	89.4	4.7	4.4	1.1

As seen previously, the level of purification alters the pore structure of the lignin-derived carbon cryogels. Results from nitrogen sorption analysis taken after pyrolysis at 900°C are listed in Table 7.11. As expected, the surface area and pore volume are very low for these samples due to their high pyrolysis temperature. However, with multiple purification steps, the surface area increases in both the mesopore and micropore regions, leading to a higher total surface area. The pore volume is also significantly increased after two purification steps, as can be seen in the pore size distributions in Figure 7.14. The 2x-900 sample has almost 5 times the mesopore volume as 1x-900, and 8 times the micropore volume. The average pore sizes in both the mesopore and micropore regions are also larger when for 2x-900 when compared to 1x-900. The dramatically dissimilar pore structures of the two samples are due to the different amount of sodium impurities, which affects the polycondensation reaction during sol-gel synthesis. Fewer impurities means the precursors are less inhibited during crosslinking, creating a better networked structure with higher porosity. The differences in pore structure will have an impact on the electrochemical properties when the samples are tested as electrodes for supercapacitors.

Table 7.11. Surface area, pore volume, and pore diameter for lignin-derived carbon cryogels after pyrolysis at 900°C.

Sample	**Surface Area (m^2/g)**			**Pore Volume (cm^3/g)**		**Pore Diameter (nm)**	
	Total	**Mesopores**	**Micropores**	**Mesopores**	**Micropores**	**Mesopores**	**Micropores**
1x-900	14.5	26.9	2.2	0.046	0.001	7.8	1.4
2x-900	64.6	44.9	13.6	0.219	0.008	20.9	1.5

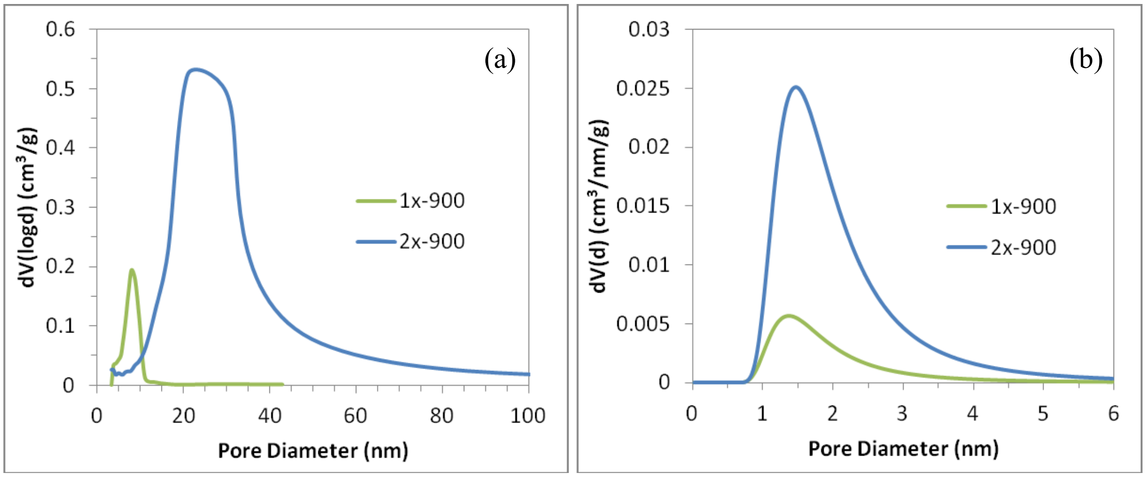

Figure 7.14. (a) Mesopore and (b) micropore size distributions for 1x and 2x purified lignin-derived carbon pyrolyzed at 900°C.

7.4.5.3 Electrochemical analysis

Cyclic voltammograms taken at 10 mV/s for 1x-900 and 2x-900 are shown in Figure 7.15. The 2x-900 sample exhibit better performance than the 1x-900 sample. The overall higher measured current density for the sample purified twice suggests that it can store more charge. The galvanic cycling curves taken at 0.5 mA in Figure 7.16 support this conclusion. The 2x-900 sample has a longer discharge curve, suggesting a higher capacitance. Table 7.12 lists the capacitance for both samples. For 1x-900, the gravimetric capacitance is 4.5 F/g, while the gravimetric capacitance for 2x-900 is nearly double that, having a value of 8.6 F/g. Similarly, the volumetric capacitance for 2x-900 is nealy twice that of 1x-900. The 1x-900 sample has a capacitance of 3.7 F/cm^3, while the 2x-900 sample is 7.0 F/cm^3.

Table 7.12. Capacitance normalized to mass, total surface area, and volume for 1x and 2x purified lignin-derived carbon pyrolyzed at 900°C.

Sample	**Gravimetric Capacitance (F/g)**	**Capacitance Based on Total Surface Area (F/m^2)**	**Volumetric Capacitance (F/cm^3)**
1x-900	4.5	0.198	3.7
2x-900	8.6	0.133	7.0

When compared to the cyclic voltammograms and galvanic cycles for lignin-derived carbon cryogels pyrolyzed at 450°C shown in Figures 7.9 and 7.10, these samples pyrolyzed at 900°C are very different. Unlike the samples pyrolyzed at a lower temperature, 1x-900 and 2x-900 both exhibit the rectangular CV curves that are more characteristic for double-layer formation. Furthermore, the GC curves also suggest double-layer formation due to the symmetric charging and discharging cycles. The improved behavior can be contributed to the increased conductivity for the samples pyrolyzed at the higher temperature.

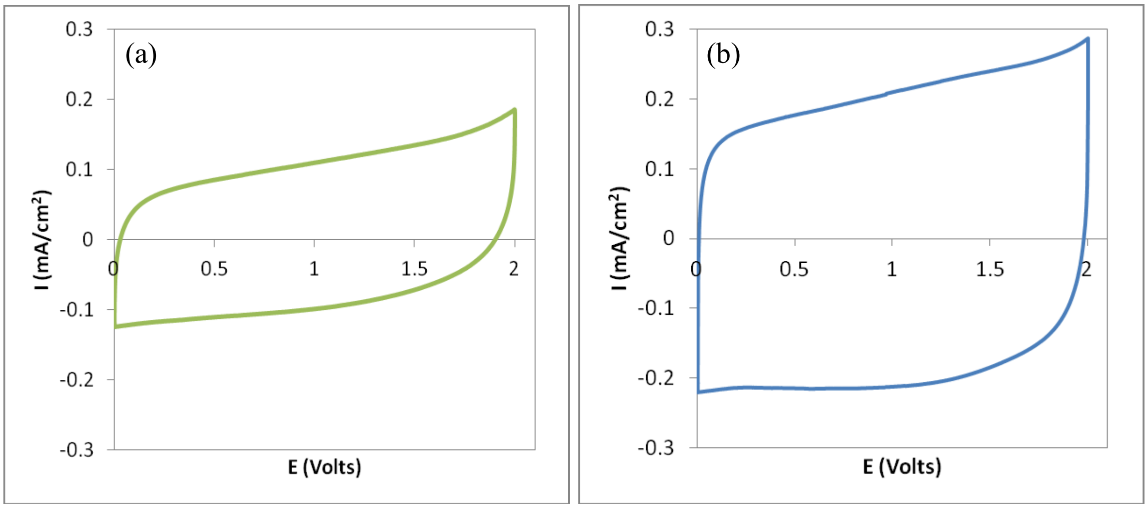

Figure 7.15. Cyclic voltammograms for (a) 1x and (b) 2x purified lignin-derived carbon cryogel pyrolyzed at 900°C.

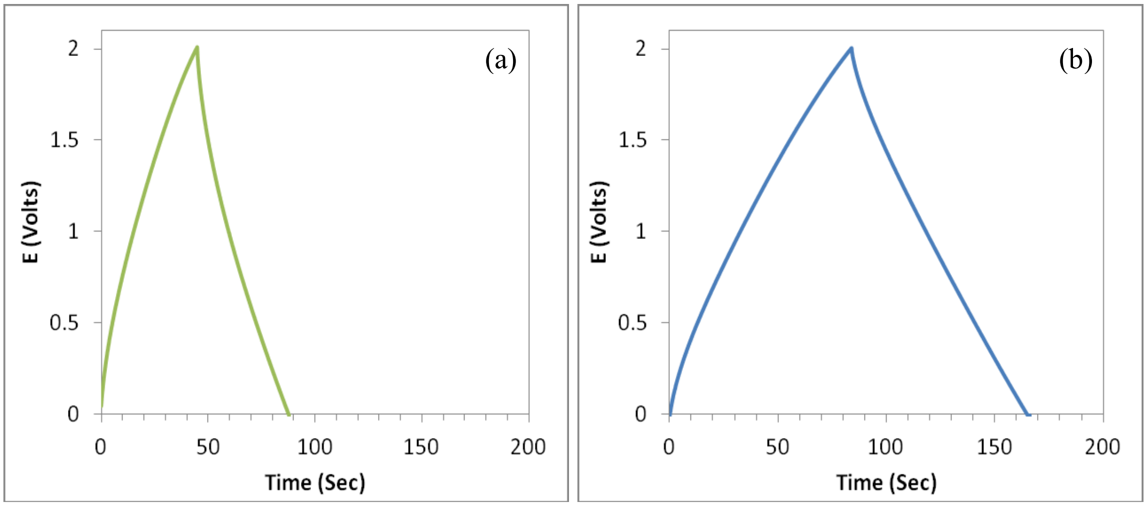

Figure 7.16. Galvanic cycles for (a) 1x and (b) 2x purified lignin-derived carbon pyrolyzed at 900°C.

When the conductivities are measured using the 4-point conductivity setup, both 1x-900 and 2x-900 have resistances that are the same order of magnitude as resorcinol-furaldehyde carbon pyrolyzed at 900°C. This is a significant improvement over the samples pyrolyzed at 450°C, which had resistances that were at least 10 times higher. The higher conductivity clearly effects the performance of the material for supercapacitors, with the lignin-derived carbon pyrolyzed at 900°C exhibiting superior charge storage ability. However, these samples still suffer from low surface area, limiting sites available for double layer formation. As such, the gravimetric capacitance is still extremely low for lignin-derived carbon as compared to resorcinol-furaldehyde derived carbon. But when the capacitance is normalized to the total surface area, lignin-derived carbon has a capacitance that rivals that of resorcinol-furaldehyde carbon. Therefore, if the surface area can be increased to close to what is obtained for resorcinol-furaldehyde carbon, lignin-derived carbon could also have similarly high gravimetric capacitance. This very promising result proves that lignin is a viable option as a precursor for high surface area carbon for high performance supercapacitors.

7.5. Summary

Lignin was investigated as a novel precursor for porous carbon. Due to the methods that are used to extract lignin from biomass, the raw material contains a large amount of impurities that needs to be removed. A low of a pyrolysis temperature is needed to retain the moderate surface area of the lignin-derived organic cryogel, which can then be activated to further increase the surface area. However, this results in a material with low conductivity that cannot be used for supercapacitors. When pyrolyzed at a high temperature, the surface area decreases due to sintering, but the material is much more conductive. When tested in devices, the low surface area severely limits the charge storage capability, and the gravimetric capacitance is low. However, normalizing to total surface area, the capacitance for lignin-derived carbon is very similar to that of resorcinol-furaldehyde carbon. This result suggests that lignin shows promise as a precursor for high surface area carbon for high performance supercapacitors.

8. ***Future work***

8.1. Device preparation

Excellent contact between the carbon electrode and the current collector is very important for good device performance. The contact resistance between these two components contributes to the ESR, which is used to calculate the power density. A lower ESR translates to a higher power density. The current method for obtaining intimate contact between the electrode and current collector is to apply pressure by hand. However, this method is inconsistent due to lack of precise control over the pressure applied. Additionally, the pressure is limited by the strength of the operator, which may not be high enough to ensure the best contact between the electrode and current collector.

In order to improve the reproducibility and reduce contact resistance, several other methods to attach a current collector to an electrode can be explored. (1) A hot press, which consists of a pair of parallel metal plates controlled by hydraulics, can provide a constant known pressure with or without the use of heat. The pressure is selected through a user-controlled program, and is much higher than what can be achieved by hand. (2) Silver paste can be used to paint on electrical contacts for thin film devices. Since the silver can be directly applied to the carbon electrode as the current collector, there is no need to apply pressure to achieve good contact. (3) An evaporator can be used to deposit metal to a surface directly from the vapor phase. A current is applied through the metal to atomize it and the material is then coated onto the exposed surface of a sample to create the current collector. Like using silver paste, this method eliminates the need to apply pressure after deposition to achieve good contact between the electrode and current collector. Devices made using these three methods will be measured by electrochemical impedance spectroscopy to determine their ESR, which can then be compared to a device prepared using the standard method to attach current collectors.

8.2. Surface chemistry modification with different elements

Most work that introduces foreign elements into porous carbon as either heteroatoms or surface functionalities has focused on oxygen and nitrogen. However, other elements can show similar affects. For example, surface modification of porous carbon with a combination of boron and nitrogen has already shown to increase capacitance when compared to unmodified carbon.[107] This trend was also seen for porous carbon modified with surface nitrogen and fluorine functional groups.[73] However, with these two examples, it is unclear whether the increased performance is due to the nitrogen, the boron or fluorine, or a combination of both. Additional studies are needed to investigate the role of each element individually.

Among the elements that can be used to modify porous carbon, sulfur and phosphorus seem to be the most promising candidates. On the periodic table, sulfur is in the same column as oxygen and phosphorus is in the same column as nitrogen. Therefore, it is believed that they will exhibit correspondingly similar pseudocapacitive behavior in supercapacitors, leading to increased capacitance. Some researchers have already noted the benefits of adding sulfur to porous carbon. For example, sulfur functional groups can act as receptor sites for metal catalysts in carbon aerogels,[137] or enhance gas storage in microporous carbons.[138] However, few studies have looked at the effect of sulfur modification on porous carbon used for supercapacitors, but some preliminary results suggest adding a sulfur coating to activated carbon can smooth the pore surfaces, reducing surface scattering effects. This increases the capacitance, and therefore the energy density.[139] It will also be interesting to see how modifying with these elements affects carbon's ability to be cycled at higher voltages. While the cyclic stability decreases for carbon modified on the surface with nitrogen when cycled at 2.5V and 3V, sulfur or phosphorous coatings may be more stable at high voltages.

To investigate the properties of these elements, highly porous carbon derived from resorcinol-furaldehyde gels can be modified with the same solution method that was used to coat nitrogen on the pore surfaces. Nitrogen-containing hexamine again will be the reactive catalyst as its role in the polycondensation reaction is already understood. While the use of hexamine will add nitrogen to the bulk carbon network, this should not significantly affect the pseudocapacitance characterization for carbon modified with either sulfur or phosphorus as it has already been established that foreign elements on the surface have greater impact on electrochemical properties than heteroatoms in the bulk.

Modification with sulfur or phosphorous can be performed on the wet organic gel before freeze drying, or on the carbon cryogel after activation. After modification, the samples can be characterized using multiple techniques such as nitrogen sorption, SEM, and XPS, and the electrochemical properties can be measured with cyclic voltammetry, galvanic cycling, and electrochemical impedance spectroscopy both at the normal operating voltage of 2V and at higher voltages.

8.3. Lignin

Electrochemical measurements show that purified lignin-derived carbon pyrolyzed at 900°C has very similar capacitance values as resorcinol-furaldehyde derived carbon when normalized to total surface area. However, the very low porosity results in limited gravimetric charge storage capacity. Future work should focus on increasing the surface area and pore volume. Perhaps the simplest way to accomplish this is through optimization of the activation process. The activation time in previous experiments was selected in order to achieve the desired 50% mass loss. However, the low surface area suggests that this may not be the ideal time. The activation time can be adjusted to achieve various levels of mass loss, and these samples should be measured by nitrogen sorption to determine which sample has the highest surface area. Additionally, several different temperatures can be tested while keeping the level of mass loss constant, which can be determined by TGA. Again, these samples should be measured by nitrogen sorption. Once a satisfactory porous structure is achieved, electrochemical properties can be tested.

Issues with the high level of impurities can be addressed in two ways. From EDX, oxygen occurs in a higher atomic percent in lignin-derived carbon cryogels than resorcinol-furaldehyde derived carbon cryogels (approximately 9 atom% and <3 atom%, respectively). Rather than attempting to remove the oxygen, it can be exploited for its pseudocapacitive properties in aqueous electrolyte. In this way, the oxygen can contribute to the capacitance rather than cause detrimental reactions as it will in organic electrolytes. Alternatively, a nitrogen coating can be added to the surface of the pores with the same simple solution method that was used to modify resorcinol-furaldehyde carbon with nitrogen. Besides inducing pseudocapacitive reactions that increase the overall capacitance, it is believed that the nitrogen coating can prevent the impurities from coming in contact with the electrolyte. If this is indeed the case, the implication is that highly pure carbon is not necessary to achieve excellent performance in supercapacitors. Instead, inexpensive precursors that are derived from natural resources can be used to replace costly synthetic precursors while still retaining the ability to finely tune the porous structure.

Acknowledgements

Thank you to my advisor Professor Guozhong Cao for ideas, advice, and encouragement. Also, thanks to Professor Christine Luscombe, Professor Brian Flinn, and Professor Richard Gustafson for agreeing to be on my committee and offering a lot of helpful suggestions. Thank you also to past and present Cao group members, including Betzaida Batalla Garcia for lots of advice and guidance, Evan Uchaker for EDX, Yanyi Liu for SEM, Professor Yunxia Huang for SEM and EDX, and Jolin Lan for 4-point conductivity measurements. Additionally, thanks to Ashley Tracey for contact angles and FTIR, Ryan Toivola for FTIR, Jim Hull and Gerry Hammer from NESAC/BIO in Bioengineering for XPS (supported by NIBIB grant EB-002027), and finally Chris Dandeneau and Professor Fumio Ohuchi for XPS.

This work was funded by the National Science Foundation (DMR-0605159 and CMMI-1030048), University of Washington's IGERT: Bioresource-based Energy for Sustainable Societies (DGE-0654252), and the Intel Corporation.

References

1. Suhas, P. J. M. Carrott and M. M. L. R. Carrott, *Bioresource Technol*, 2007, **98**, 2301-2312.
2. P. J. Hall, M. Mirzaeian, S. I. Fletcher, F. B. Sillars, A. J. R. Rennie, G. O. Shitta-Bey, G. Wilson, A. Cruden and R. Carter, *Energ Environ Sci*, 2010, **3**, 1238-1251.
3. P. Simon and Y. Gogotsi, *Nat Mater*, 2008, **7**, 845-854.
4. C. Peng, S. W. Zhang, D. Jewell and G. Z. Chen, *Prog Nat Sci*, 2008, **18**, 777-788.
5. M. Inagaki, H. Konno and O. Tanaike, *Journal of Power Sources*, 2010, **195**, 7880-7903.
6. A. F. Burke, *P Ieee*, 2007, **95**, 806-820.
7. J. H. Kim, K. Zhu, Y. F. Yan, C. L. Perkins and A. J. Frank, *Nano Lett*, 2010, **10**, 4099-4104.
8. Y. Korenblit, M. Rose, E. Kockrick, L. Borchardt, A. Kvit, S. Kaskel and G. Yushin, *Acs Nano*, 2010, **4**, 1337-1344.
9. C. Liu, F. Li, L. P. Ma and H. M. Cheng, *Adv. Mater.*, 2010, **22**, E28-E62.
10. F. Beguin and E. Frackowiak, *Carbons for Electrochemical Energy Storage and Conversion Systems*, CRC Press, Boca Raton, 2010.
11. Y. H. Kim, in *Electronic Component News*, 2002.
12. V. V. N. Obreja, *Physica E*, 2008, **40**, 2596-2605.
13. S. L. Candelaria, Y. Y. Shao, W. Zhou, X. L. Li, J. Xiao, J. G. Zhang, Y. Wang, J. Liu, J. H. Li and G. Z. Cao, *Nano Energy*, 2012, **1**, 195-220.
14. B. C. Thompson and J. M. J. Frechet, *Angew Chem Int Edit*, 2008, **47**, 58-77.
15. Y. Q. Sun, Q. O. Wu and G. Q. Shi, *Energ Environ Sci*, 2011, **4**, 1113-1132.
16. E. Yoo, J. Kim, E. Hosono, H. Zhou, T. Kudo and I. Honma, *Nano Lett*, 2008, **8**, 2277-2282.
17. B. J. Landi, M. J. Ganter, C. D. Cress, R. A. DiLeo and R. P. Raffaelle, *Energ Environ Sci*, 2009, **2**, 638-654.
18. B. Panella, M. Hirscher and S. Roth, *Carbon*, 2005, **43**, 2209-2214.
19. D. Lozano-Castello, J. Alcaniz-Monge, M. A. de la Casa-Lillo, D. Cazorla-Amoros and A. Linares-Solano, *Fuel*, 2002, **81**, 1777-1803.
20. A. Feaver and G. Z. Cao, *Carbon*, 2006, **44**, 590-593.
21. A. Feaver, S. Sepehri, P. Shamberger, A. Stowe, T. Autrey and G. Z. Cao, *J Phys Chem B*, 2007, **111**, 7469-7472.
22. T. Otowa, Y. Nojima and T. Miyazaki, *Carbon*, 1997, **35**, 1315-1319.
23. C. Y. Lu and H. S. Chiu, *Chem Eng Sci*, 2006, **61**, 1138-1145.
24. V. Gomez-Serrano, A. Macias-Garcia, A. Espinosa-Mansilla and C. Valenzuela-Calahorro, *Water Res*, 1998, **32**, 1-4.
25. M. C. Annesini, C. Di Carlo, V. Piemonte and L. Turchetti, *Biochem Eng J*, 2008, **40**, 205-210.
26. D. J. Malik, G. L. Warwick, I. Mathieson, N. A. Hoenich and M. Streat, *Carbon*, 2005, **43**, 2317-2329.
27. R. J. A. Bigsby, R. J. Rider and G. N. Blount, *P I Mech Eng H*, 1998, **212**, 373-381.
28. C. Ye, Q. M. Gong, F. P. Lu and J. Liang, *Sep Purif Technol*, 2007, **58**, 2-6.
29. S. H. Joo, S. J. Choi, I. Oh, J. Kwak, Z. Liu, O. Terasaki and R. Ryoo, *Nature*, 2001, **412**, 169-172.
30. G. G. Park, T. H. Yang, Y. G. Yoon, W. Y. Lee and C. S. Kim, *Int J Hydrogen Energ*, 2003, **28**, 645-650.
31. E. Auer, A. Freund, J. Pietsch and T. Tacke, *Appl Catal a-Gen*, 1998, **173**, 259-271.
32. A. Guha, W. J. Lu, T. A. Zawodzinski and D. A. Schiraldi, *Carbon*, 2007, **45**, 1506-1517.

33. W. C. Chen, T. C. Wen and H. S. Teng, *Electrochimica Acta*, 2003, **48**, 641-649.
34. K. Wang, J. Y. Huang and Z. X. Wei, *J Phys Chem C*, 2010, **114**, 8062-8067.
35. Y. Y. Gao, S. L. Chen, D. X. Cao, G. L. Wang and J. L. Yin, *J Power Sources*, 2010, **195**, 1757-1760.
36. M. Rose, E. Kockrick, I. Senkovska and S. Kaskel, *Carbon*, 2010, **48**, 403-407.
37. V. Presser, L. F. Zhang, J. J. Niu, J. McDonough, C. Perez, H. Fong and Y. Gogotsi, *Adv Energy Mater*, 2011, **1**, 423-430.
38. J. Lee, J. Kim and T. Hyeon, *Adv. Mater.*, 2006, **18**, 2073-2094.
39. M. Kodama, J. Yamashita, Y. Soneda, H. Hatori, S. Nishimura and K. Kamegawa, *Materials Science and Engineering B-Solid State Materials for Advanced Technology*, 2004, **108**, 156-161.
40. W. Xing, S. Z. Qiao, R. G. Ding, F. Li, G. Q. Lu, Z. F. Yan and H. M. Cheng, *Carbon*, 2006, **44**, 216-224.
41. L. C. Sang, A. Vinu and M. O. Coppens, *Journal of Materials Chemistry*, 2011, **21**, 7410-7417.
42. D. Banham, F. X. Feng, J. Burt, E. Alsrayheen and V. Birss, *Carbon*, 2010, **48**, 1056-1063.
43. K. Matsuoka, Y. Yamagishi, T. Yamazaki, N. Setoyama, A. Tomita and T. Kyotani, *Carbon*, 2005, **43**, 876-879.
44. F. Wu and B. Xu, *New Carbon Mater*, 2006, **21**, 176-184.
45. G. Lota, K. Fic and E. Frackowiak, *Energ Environ Sci*, 2011, **4**, 1592-1605.
46. K. H. An, W. S. Kim, Y. S. Park, Y. C. Choi, S. M. Lee, D. C. Chung, D. J. Bae, S. C. Lim and Y. H. Lee, *Adv Mater*, 2001, **13**, 497-500.
47. C. G. Liu, H. T. Fang, F. Li, M. Liu and H. M. Cheng, *J Power Sources*, 2006, **160**, 758-761.
48. A. B. Fuertes, F. Pico and J. M. Rojo, *J Power Sources*, 2004, **133**, 329-336.
49. M. D. Stoller, S. J. Park, Y. W. Zhu, J. H. An and R. S. Ruoff, *Nano Lett*, 2008, **8**, 3498-3502.
50. S. R. C. Vivekchand, C. S. Rout, K. S. Subrahmanyam, A. Govindaraj and C. N. R. Rao, *J Chem Sci*, 2008, **120**, 9-13.
51. A. P. Yu, I. Roes, A. Davies and Z. W. Chen, *Appl Phys Lett*, 2010, **96**, 253105.
52. Y. Wang, Z. Q. Shi, Y. Huang, Y. F. Ma, C. Y. Wang, M. M. Chen and Y. S. Chen, *J Phys Chem C*, 2009, **113**, 13103-13107.
53. C. G. Liu, Z. N. Yu, D. Neff, A. Zhamu and B. Z. Jang, *Nano Lett*, 2010, **10**, 4863-4868.
54. Q. Cheng, J. Tang, J. Ma, H. Zhang, N. Shinya and L. C. Qin, *Phys Chem Chem Phys*, 2011, **13**, 17615-17624.
55. S. Y. Yang, K. H. Chang, H. W. Tien, Y. F. Lee, S. M. Li, Y. S. Wang, J. Y. Wang, C. C. M. Ma and C. C. Hu, *J Mater Chem*, 2011, **21**, 2374-2380.
56. R. W. Pekala, *J Mater Sci*, 1989, **24**, 3221-3227.
57. D. C. Wu, R. W. Fu, S. T. Zhang, M. S. Dresselhaus and G. Dresselhaus, *J Non-Cryst Solids*, 2004, **336**, 26-31.
58. R. W. Pekala, J. C. Farmer, C. T. Alviso, T. D. Tran, S. T. Mayer, J. M. Miller and B. Dunn, *J Non-Cryst Solids*, 1998, **225**, 74-80.
59. R. W. Pekala, C. T. Alviso, X. Lu, J. Gross and J. Fricke, *J Non-Cryst Solids*, 1995, **188**, 34-40.
60. M. H. Nguyen and L. H. Dao, *J Non-Cryst Solids*, 1998, **225**, 51-57.
61. J. Biener, M. Stadermann, M. Suss, M. A. Worsley, M. M. Biener, K. A. Rose and T. F. Baumann, *Energ Environ Sci*, 2011, **4**, 656-667.
62. V. Bock, A. Emmerling, R. Saliger and J. Fricke, *J Porous Mat*, 1997, **4**, 287-294.

63. R. W. Pekala, C. T. Alviso, F. M. Kong and S. S. Hulsey, *J Non-Cryst Solids*, 1992, **145**, 90-98.
64. H. Tamon, H. Ishizaka, T. Yamamoto and T. Suzuki, *Carbon*, 1999, **37**, 2049-2055.
65. B. B. Garcia, A. M. Feaver, Q. F. Zhang, R. D. Champion, G. Z. Cao, T. T. Fister, K. P. Nagle and G. T. Seidler, *J Appl Phys*, 2008, **104,** 014305.
66. O. Barbieri, M. Hahn, A. Herzog and R. Kotz, *Carbon*, 2005, **43**, 1303-1310.
67. A. Izadi-Najafabadi, S. Yasuda, K. Kobashi, T. Yamada, D. N. Futaba, H. Hatori, M. Yumura, S. Iijima and K. Hata, *Adv. Mater.*, 2010, **22**, E235-E241.
68. H. Iwasaki, N. Sugo and G. Uehara, Patent number EP1176617A2, 2002.
69. S. Ghosh, X. H. An, R. Shah, D. Rawat, B. Dave, S. Kar and S. Talapatra, *Journal of Physical Chemistry C*, 2012, **116**, 20688-20693.
70. P. Azais, L. Duclaux, P. Florian, D. Massiot, M. A. Lillo-Rodenas, A. Linares-Solano, J. P. Peres, C. Jehoulet and F. Beguin, *Journal of Power Sources*, 2007, **171**, 1046-1053.
71. D. Hulicova, J. Yamashita, Y. Soneda, H. Hatori and M. Kodama, *Chemistry of Materials*, 2005, **17**, 1241-1247.
72. D. Hulicova-Jurcakova, M. Kodama, S. Shiraishi, H. Hatori, Z. H. Zhu and G. Q. Lu, *Advanced Functional Materials*, 2009, **19**, 1800-1809.
73. M. J. Jung, E. Jeong, S. Cho, S. Y. Yeo and Y. S. Lee, *J Colloid Interf Sci*, 2012, **381**, 152-157.
74. K. Jurewicz, K. Babel, A. Ziolkowski and H. Wachowska, *Electrochimica Acta*, 2003, **48**, 1491-1498.
75. E. Frackowiak, *Phys Chem Chem Phys*, 2007, **9**, 1774-1785.
76. E. Frackowiak and F. Beguin, *Carbon*, 2001, **39**, 937-950.
77. C. M. Yang, Y. J. Kim, M. Endo, H. Kanoh, M. Yudasaka, S. Iijima and K. Kaneko, *J Am Chem Soc*, 2007, **129**, 20-21.
78. J. C. Farahmendi, J. M. Dispennette, E. Blank and A. C. Kolb, Patent numbers WO9815962, EP0946954, JP 2001502117T, 1998.
79. Y. P. Zhai, Y. Q. Dou, D. Y. Zhao, P. F. Fulvio, R. T. Mayes and S. Dai, *Adv. Mater.*, 2011, **23**, 4828-4850.
80. M. E. Orazem and B. Tribollet, *Electrochemical Impedance Spectroscopy*, John Wiley & Sons, Inc., Hoboken, New Jersey, 2008.
81. J. R. Miller, *Ieee Electr Insul M*, 2010, **26**, 40-47.
82. L. L. Zhang, R. Zhou and X. S. Zhao, *Journal of Materials Chemistry*, 2010, **20**, 5983-5992.
83. R. De Levie, *Electrochimica Acta*, 1963, **8**, 751-780.
84. J. W. Lang, X. B. Yan, X. Y. Yuan, J. Yang and Q. J. Xue, *Journal of Power Sources*, 2011, **196**, 10472-10478.
85. Y. T. Kim, Y. Ito, K. Tadai, T. Mitani, U. S. Kim, H. S. Kim and B. W. Cho, *Appl Phys Lett*, 2005, **87,** 234106.
86. L. P. Zheng, Y. Wang, X. Y. Wang, X. Y. Wang, H. F. An and L. H. Yi, *J Mater Sci*, 2010, **45**, 6030-6037.
87. W. Xiong, M. X. Liu, L. H. Gan, Y. K. Lv, Z. J. Xu, Z. X. Hao and L. W. Chen, *Colloid Surface A*, 2012, **411**, 34-39.
88. J. M. Shen, A. D. Liu, Y. Tu, G. S. Foo, C. B. Yeo, M. B. Chan-Park, R. R. Jiang and Y. Chen, *Energ Environ Sci*, 2011, **4**, 4220-4229.
89. M. D. Stoller and R. S. Ruoff, *Energ Environ Sci*, 2010, **3**, 1294-1301.
90. A. Lewandowski and M. Galinski, *Journal of Power Sources*, 2007, **173**, 822-828.
91. Z. Lei, Z. Chen and X. S. Zhao, *Journal of Physical Chemistry C*, 2010, **114**, 19867-19874.

92. M. J. Deng, F. L. Huang, I. W. Sun, W. T. Tsai and J. K. Chang, *Nanotechnology*, 2009, **20,** 175602.
93. R. Tummala, R. K. Guduru and P. S. Mohanty, *J Power Sources*, 2012, **209**, 44-51.
94. B. B. Garcia, D. W. Liu, S. Sepehri, S. Candelaria, D. M. Beckham, L. W. Savage and G. Z. Cao, *J Non-Cryst Solids*, 2010, **356**, 1620-1625.
95. X. Q. Zhang and D. H. Solomon, *Chemistry of Materials*, 1998, **10**, 1833-1840.
96. Thermo VG Scientific, *E3000 Series Critical Point Drying Apparatus Operating Manual,* West Sussex, England, 1999.
97. Labconco Corporation, *A Guide to Freeze Drying for the Laboratory*, Kansas City, Missouri, 2010.
98. J. Hayashi, K. Muroyama, V. G. Gomes and A. P. Watkinson, *Carbon*, 2002, **40**, 630-632.
99. T. Yamamoto, T. Nishimura, T. Suzuki and H. Tamon, *J Non-Cryst Solids*, 2001, **288**, 46-55.
100. S. L. Candelaria, R. Chen, Y. H. Jeong and G. Z. Cao, *Energ Environ Sci*, 2012, **5**, 5619-5637.
101. E. Frackowiak, *Journal of the Brazilian Chemical Society*, 2006, **17**, 1074-1082.
102. E. Frackowiak and F. Beguin, *Carbon*, 2002, **40**, 1775-1787.
103. C. O. Ania, V. Khomenko, E. Raymundo-Pinero, J. B. Parra and F. Beguin, *Advanced Functional Materials*, 2007, **17**, 1828-1836.
104. W. R. Li, D. H. Chen, Z. Li, Y. F. Shi, Y. Wan, J. J. Huang, J. J. Yang, D. Y. Zhao and Z. Y. Jiang, *Electrochem. Commun.*, 2007, **9**, 569-573.
105. G. Lota, B. Grzyb, H. Machnikowska, J. Machnikowski and E. Frackowiak, *Chemical Physics Letters*, 2005, **404**, 53-58.
106. F. Beguin, K. Szostak, G. Lota and E. Frackowiak, *Adv. Mater.*, 2005, **17**, 2380-2384.
107. S. Sepehri, B. B. Garcia, Q. Zhang and G. Cao, *Carbon*, 2009, **47**, 1436-1443.
108. J. R. Pels, F. Kapteijn, J. A. Moulijn, Q. Zhu and K. M. Thomas, *Carbon*, 1995, **33**, 1641-1653.
109. F. Kapteijn, J. A. Moulijn, S. Matzner and H. P. Boehm, *Carbon*, 1999, **37**, 1143-1150.
110. B. Ruelle, A. Felten, J. Ghijsen, W. Drube, R. L. Johnson, D. Liang, R. Erni, G. Van Tendeloo, S. Peeterbroeck, P. Dubois, T. Godfroid, M. Hecq and C. Bittencourt, *Micron*, 2009, **40**, 85-88.
111. A. Felten, C. Bittencourt, J. J. Pireaux, G. Van Lier and J. C. Charlier, *J Appl Phys*, 2005, **98,** 074308.
112. J. L. Stevens, A. Y. Huang, H. Q. Peng, L. W. Chiang, V. N. Khabashesku and J. L. Margrave, *Nano Lett*, 2003, **3**, 331-336.
113. H. Park, J. J. Zhao and J. P. Lu, *Nano Lett*, 2006, **6**, 916-919.
114. J. J. Zhao, Z. F. Chen, Z. Zhou, H. Park, P. V. Schleyer and J. P. Lu, *Chemphyschem*, 2005, **6**, 598-601.
115. M. Melle-Franco, M. Marcaccio, D. Paolucci, F. Paolucci, V. Georgakilas, D. M. Guldi, M. Prato and F. Zerbetto, *J Am Chem Soc*, 2004, **126**, 1646-1647.
116. M. Holzinger, J. Abraha, P. Whelan, R. Graupner, L. Ley, F. Hennrich, M. Kappes and A. Hirsch, *J Am Chem Soc*, 2003, **125**, 8566-8580.
117. K. Jurewicz, K. Babel, A. Ziolkowski, H. Wachowska and M. Kozlowski, *Fuel Processing Technology*, 2002, **77**, 191-198.
118. M. Q. Wu, G. A. Snook, V. Gupta, M. Shaffer, D. J. Fray and G. Z. Chen, *Journal of Materials Chemistry*, 2005, **15**, 2297-2303.
119. M. D. Ingram, A. J. Pappin, F. Delalande, D. Poupard and G. Terzulli, *Electrochimica Acta*, 1998, **43**, 1601-1605.

120. M. Hughes, G. Z. Chen, M. S. P. Shaffer, D. J. Fray and A. H. Windle, *Chemistry of Materials*, 2002, **14**, 1610-1613.
121. W. S. Huang, B. D. Humphrey and A. G. Macdiarmid, *J Chem Soc Farad T 1*, 1986, **82**, 2385-2400.
122. R. Kotz and M. Carlen, *Electrochimica Acta*, 2000, **45**, 2483-2498.
123. H. Y. Tian, C. E. Buckley, S. Mule, M. Paskevicius and B. B. Dhal, *Nanotechnology*, 2008, **19**, 475605.
124. B. B. Garcia, S. L. Candelaria, D. Liu, S. Sepheri, J. A. Cruz and G. Cao, *Renewable Energy*, 2011, **36**, 1788-1794.
125. Z. X. Ma, T. Kyotani, Z. Liu, O. Terasaki and A. Tomita, *Chemistry of Materials*, 2001, **13**, 4413-4415.
126. C. T. Lynch, R. Summitt and A. Sliker, *CRC handbook of materials science*, CRC Press, Boca Raton, Fla., 1974.
127. P. X. Hou, H. Orikasa, T. Yamazaki, K. Matsuoka, A. Tomita, N. Setoyama, Y. Fukushima and T. Kyotani, *Chemistry of Materials*, 2005, **17**, 5187-5193.
128. University of Colorado at Boulder, Table of Characteristic IR Absorptions, 2013, http://orgchem.colorado.edu/Spectroscopy/specttutor/irchart.html.
129. B. B. Garcia, S. L. Candelaria and G. Z. Cao, *J Mater Sci*, 2012, **47**, 5996-6004.
130. A. P. Dementjev, A. de Graaf, M. C. M. van de Sanden, K. I. Maslakov, A. V. Naumkin and A. A. Serov, *Diamond and Related Materials*, 2000, **9**, 1904-1907.
131. C. Peng, S. Zhang, X. Zhou and G. Z. Chen, *Energ Environ Sci*, 2010, **3**, 1499-1502.
132. O. Kimizuka, O. Tanaike, J. Yamashita, T. Hiraoka, D. N. Futaba, K. Hata, K. Machida, S. Suematsu, K. Tamamitsu, S. Saeki, Y. Yamada and H. Hatori, *Carbon*, 2008, **46**, 1999-2001.
133. W. K. El-Zawawy, *Polym Advan Technol*, 2005, **16**, 48-54.
134. M. A. Khan, S. M. Ashraf and V. P. Malhotra, *J Appl Polym Sci*, 2004, **92**, 3514-3523.
135. N. E. El Mansouri, A. Pizzi and J. Salvado, *J Appl Polym Sci*, 2007, **103**, 1690-1699.
136. T. Lindstrom and L. Westman, *Colloid Polym Sci*, 1980, **258**, 390-397.
137. W. S. Baker, J. W. Long, R. M. Stroud and D. R. Rolison, *J Non-Cryst Solids*, 2004, **350**, 80-87.
138. Y. D. Xia, Y. Q. Zhu and Y. Tang, *Carbon*, 2012, **50**, 5543-5553.
139. Y. X. Huang, S. L. Candelaria, Y. W. Li, Z. M. Li, J. J. Tian, L. L. Zhang and G. Z. Cao, *Carbon*, submitted for publication.